

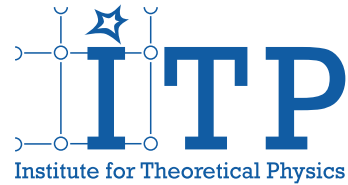
JOHANN WOLFGANG GOETHE-UNIVERSITÄT FRANKFURT AM MAIN
INSTITUT FÜR THEORETISCHE PHYSIK

Master's Thesis

Locating the Heavy Z_2 Point in $N_f=2$ LQCD at Zero Chemical Potential

Reinhold Kaiser

20. November 2020



Supervisor and first referee: Prof. Dr. Owe Philipsen
Second referee: Dr. Alessandro Sciarra

Contents

Abstract	V
Zusammenfassung	VI
Introduction	1
1. Introduction to Lattice QCD	4
1.1. Continuum QCD	4
1.2. Lattice QCD	7
1.3. Finite Temperature LQCD	10
1.4. Continuum and Thermodynamic Limit	11
1.5. Scale Setting	12
1.6. Deconfinement and the Center Symmetry	13
2. The QCD Phase Diagram and the Columbia Plot	16
2.1. General Aspects about Phase Transitions	16
2.1.1. Types of Phase Transitions	17
2.1.2. Finite Size Scaling	19
2.2. The QCD Phase Diagram	22
2.3. The Columbia Plot	24
3. Numerical Aspects of Phase Transitions in LQCD	27
3.1. Numerical Analysis of Phase Transitions	27
3.1.1. Monte Carlo Importance Sampling	27
3.1.2. Analyzing an Observable	29
3.1.3. Reweighting	30
3.1.4. Skewness and Kurtosis	32
3.1.5. Finite Size Scaling of the Kurtosis	35
3.1.6. Fitting to the Kurtosis	38
3.2. Numerical Tools	43
3.2.1. CL ² QCD	43
3.2.2. BaHaMAS	44
3.2.3. PLASMA	45
3.2.4. Mass Measurement and Scale Setting Handling	46
3.3. Python Fitting GUI	46
3.3.1. Motivation	47
3.3.2. Overview over the Structure	48
3.3.3. Available Fit Functions	54
3.3.4. Tests	56

4. Locating the Heavy Z_2-point	59
4.1. Overview over the Simulations	59
4.2. Discussion of the Obtained Kurtosis Points	61
4.3. Finding Good Fits	66
4.3.1. Discussion of the Constraints to the Fits	66
4.3.2. Analysis of the Different Fit Ansätze	67
4.4. Obtaining a Critical Mass	75
Summary and Conclusion	78
Appendix A. Derivation of the Kurtosis Correction Term	82
Appendix B. Derivation of the Fit Formulas	85
B.1. The Rescaling Term in the Polynomial Fit	86
B.2. The General Logistic Fit Functions	87
B.3. The Gompertz Fit Function	89
Appendix C. Additional Tables Concerning the PFG Tests	91
Bibliography	94

Abstract

The QCD thermal transition at zero chemical potential is a crossover for $N_f=2$ quarks with physical quark masses. For infinitely heavy quarks this transition is a first order phase transition, which can be related to the spontaneous breaking of the global Z_3 center symmetry. Finite quark masses break the center symmetry explicitly and when decreasing the quark mass the first order phase transition weakens until it vanishes at the critical Z_2 point. The localization of the critical mass with $N_f=2$ lattice QCD, employing staggered fermions on lattices with temporal extent $N_\tau=8$, is the goal of this master's thesis. The result is compared qualitatively to similar calculations with Wilson fermions and good agreement is found. Furthermore it is discussed how Monte Carlo data can be analyzed with respect to phase transitions, focusing on the skewness and the kurtosis of the order parameter, which is the Polyakov loop. The derivation of a finite size scaling formula for the kurtosis at a Z_2 critical point is shown, forming the basis for the development of kurtosis fit functions. Applying the fit functions to kurtosis data from simulations, the critical mass can be extracted as a fit parameter. Different fit functions are examined and the Gompertz function is proposed as a new possible kurtosis fit function. To perform these fits a new tool was developed, which is called Python Fitting GUI (PFG). It allows a comfortable examination of various kurtosis fits in a functional graphical user interface (GUI).

Zusammenfassung

Der thermische Übergang der QCD für verschwindendes chemisches Potential und $N_f=2$ Quarks mit physikalischen Massen ist ein Crossover. Für unendlich schwere Quarks wird dieser Übergang ein Phasenübergang erster Ordnung, der mit der spontanen Symmetriebrechung der globalen Z_3 Zentrumssymmetrie verknüpft ist. Endliche Quarkmassen brechen die Zentrumssymmetrie explizit und abnehmende Quarkmassen schwächen den Phasenübergang erster Ordnung, bis er am kritischen Z_2 Punkt verschwindet. Das Ziel dieser Masterarbeit ist die Lokalisierung der kritischen Masse im Rahmen der $N_f=2$ Gitter-QCD auf Gittern mit $N_\tau=8$ zeitlicher Ausdehnung unter Verwendung der staggered-Fermionen-Wirkung. Das Resultat wird qualitativ mit ähnlichen Rechnungen für Wilson-Fermionen verglichen und eine gute Übereinstimmung kann gezeigt werden. Außerdem wird diskutiert, wie Monte-Carlo-Daten in Hinsicht auf Phasenübergänge analysiert werden können, wobei sich auf die Schiefe und die Kurtosis des Ordnungsparameters, dem Polyakov-Loop konzentriert wird. Es wird die Herleitung einer „Finite-Size-Scaling“-Formel der Kurtosis am kritischen Z_2 -Punkt gezeigt, was die Grundlage für die Entwicklung von Kurtosis-Fit-Funktionen bildet. Werden die Fitfunktionen auf die Kurtosisdaten der Simulationen angewendet, kann die kritische Masse als Fitparameter extrahiert werden. Verschiedene Fitfunktionen werden untersucht und die Gompertz-Funktion als neue mögliche Kurtosis-Fit-Funktion vorgeschlagen. Um diese Fits durchzuführen, wurde eine neue Software mit dem Namen Python Fitting GUI (PFG) entwickelt. Sie ermöglicht die bequeme Untersuchung von mehreren Kurtosisfits in einem funktionalen grafischem User Interface (GUI).

Introduction

In today's research in physics, particle physics or high energy physics is one of the largest fields. It investigates the smallest possible particles, called elementary particles, and its interactions. The model describing these elementary particles is the Standard Model of particle physics, combining three basic forces of the universe: the strong, the weak and the electromagnetic interactions. The fourth fundamental force, the gravitational force, has not been managed to be included in one unified theory, which contains all fundamental forces. Nevertheless, for the three other fundamental forces, the Standard Model has been and still is successful in predicting and explaining results from experiments.

One sector of the Standard Model is the Quantum Chromodynamics (QCD) sector. It is the theory describing the strong force between elementary particles called quarks and gluons. Quarks are spin=1/2 fermions with a mass and an electric and a color charge. On the other hand, gluons are massless bosons with spin=1, acting as exchange particles between the quarks. QCD is a quantum field theory, where quarks and gluons are described by fields in four dimensional space-time. An important symmetry of QCD is the $SU(3)$ gauge symmetry, which is responsible for the generation of color charge. Thus, quarks can either have red, blue or green color charge. Another important property of QCD is asymptotic freedom, denoting the phenomenon that interactions between particles become asymptotically weaker as the energy scale of the interaction increases and the length scale decreases. As a consequence, quarks are confined for low energies or temperatures to the so called hadrons, e.g. protons, neutrons or pions. These particles are color neutral combinations of quarks, implying for example, that either three quarks, all with different color, or two quarks (quark and anti-quark) with a particular color and its anti-color bind together. On the other hand, there is significant evidence that quarks become deconfined for energies sufficiently large to render the interaction between quarks and gluons asymptotically weak. The phase for the deconfined quarks and gluons at large temperatures is called quark-gluon-plasma (QGP), where the term plasma indicates, that free color charges are allowed. Due to these different temperature dependent phases, a transition from one phase into the other is expected. It has already been shown, that this thermal QCD transition is not a true phase transition, but rather an analytical crossover for small densities [2]. In the early universe, this crossover is assumed to have taken place a few tens of microseconds after the big bang, when the fast expansion of the system lead to a decrease of the temperature. At this point, quarks and gluons from the QGP formed hadrons, the type of particles, also forming the atomic nucleus. In current nature the QGP may be found in the extremely dense cores of neutrons stars. Beyond that, the QGP can be detected in heavy ion collision experiments at large particle colliders.

The hadronic phase and the QGP can be represented in the QCD phase diagram. It is a temperature vs. density (or baryonic chemical potential) diagram, depicting the different phases of the thermodynamic system of QCD as areas. The lines or points separating the phases mark the (phase) transitions, which take place, when varying the parameters temperature and density of the QCD system correspondingly. The explo-

ration of the QCD phase diagram is an important goal of current QCD research, as still many regions of it are only conjectured. A detailed quantitative understanding of the QCD phase diagram would allow to explain the behavior of strong interacting matter for arbitrary combinations of the parameters temperature and density. This in turn would help to advance the analysis of astrophysical observations, for example neutron stars. Experimental approaches focusing on the thermal QCD transition require large heavy ion colliders and detectors. These can be found at CERN in Switzerland, namely the Large Hadron Collider (LHC) or in Brookhaven (USA) the Relativistic Heavy Ion Collider (RHIC). The heavy ions are accelerated close to the speed of light and a QGP forms upon high energetic collisions. The expanding system cools down and the particles hadronize. In current research, many theoretical approaches to the QCD phase diagram involve effective models. On the other hand, the first principles lattice QCD (LQCD) works without additional assumptions beyond the QCD theory. In the limit of very large density or high temperatures, perturbation theory is valid and effective models are not needed, whereas for lower finite temperatures and densities, effective models are the only approach to study the QCD phase diagram. Lattice QCD can only access QCD systems with zero real baryonic chemical potential, as a real finite chemical potential μ gives rise to a sign problem, which prohibits the use of the Monte Carlo importance sampling method. One of the main difficulties with lattice QCD is the enormous computational cost at least for finite temperature simulations. The lattice discretizes space-time, which necessitates performing the continuum limit, leading to simulations with more lattice points. Additionally the lattice extent is finite, which demands performing the thermodynamic limit. The resulting growth of the lattice further increases the number of lattice points. Nevertheless, lattice QCD is quite successful, when exploring the $\mu=0$ line in the QCD phase diagram. For example, it served to determine the QCD crossover transition temperature of 150MeV to 170MeV [7].

At physical quark masses, the QCD thermal transition is a crossover, but considering non-physical masses allows insights into the phase structure of QCD. The so called Columbia plot represents just this, the type of the QCD thermal transition as a function of the two degenerate up and down quark masses on one axis and the strange quark mass on the other axis. At this point, the main goal of this master's thesis is explained by referring to the terms from the title "Locating the Heavy Z_2 Point in $N_f=2$ LQCD at Zero Chemical Potential". It has been already said, that lattice QCD (LQCD) is not applicable to real chemical potentials different from zero. The term $N_f=2$ refers to the number of degenerate quark flavors, thus considering only the lightest up and down quarks. In the Columbia plot, the upper border line is denoted as $N_f=2$ line, where the strange quark is infinitely heavy. The heavy Z_2 line represents the change of the type of the thermal QCD transition from a crossover to a first order phase transition towards heavier quark masses. At this line the QCD thermal transition is a second order phase transition, separating the crossover and the first order phase transition areas. This Z_2 line hits the $N_f=2$ line at the Z_2 point, whose localization with respect to the up and down quark mass is the main goal of this master's thesis.

Currently, the heavy mass region of the Columbia plot is known qualitatively well, meaning, that the different types of phase transitions have been found. However, as an example, the exact value of the critical mass of the Z_2 point requires to be determined. The approach to locate this critical mass involves LQCD simulations at various

unphysical quark masses in a range, where the Z_2 point is estimated to be located. For establishing the critical mass value, the continuum limit has to be performed, which makes it difficult, among other things, to determine the heavy Z_2 point. Considering the huge computational cost of exploring the heavy quark mass region of the Columbia plot, why is it rewarding to exactly localize the Z_2 point? The Columbia plot is a two dimensional plot, but an additional axis e.g. for the chemical potential can be added. Former points become lines in the three dimensional volume of the plot. The Z_2 line might then bend towards the physical point or line for varying the chemical potential. Whether a thermodynamic system is near a critical point, is important to know, because critical points show a particular behavior, as will be seen in chapter 2. Therefore, the localization of the heavy Z_2 point is of huge interest, even though the simulated mass values are far from physical values. Moreover, it is good to know about the location of critical points in the parameter space of the theory, as they may influence extrapolations of measurements to the physical mass values. In order to guarantee a sufficient accuracy, the regions around critical points should be avoided, when using extrapolations. The practical benefits of investigating the unphysical regions of the Columbia plot justify the high computational efforts.

One important aspect of this thesis is to perform fits in order to localize the critical mass. In short, the critical mass value is extracted from a fit as a fit parameter. Performing the fits and at the same time visualizing and comparing the results, requires a specifically adapted fitting tool. The more technical goal of this master's thesis was to implement such a tool as a graphical user interface (GUI). The sophisticated implementation and the incorporation of various fit functions is the reason, why a separate section is devoted to the description of the Python Fitting GUI (PFG) and its implementation.

As a last part of the introduction, a short overview of the structure of this thesis is given. In the beginning, the theoretical basics of lattice QCD are introduced in chapter 1. The continuum QCD and its connection to lattice QCD are presented, focusing on the discretized actions, namely the Wilson gauge action and the staggered fermion action. After discussing some other important properties of lattice QCD in this chapter, the second chapter focuses on the QCD phase diagram in general and the Columbia plot. As a preparation, general aspects of phase transitions, that are of particular interest for finite thermodynamic systems, are discussed. The large chapter 3 is devoted to the numerical aspects of analyzing phase transitions of thermodynamic systems on lattices. Here, among other numerical tools to analyze the data, also the PFG is introduced as a fitting tool. At last, the results of the localization of the Z_2 point are discussed in chapter 4. This thesis concludes with a short summary and conclusion, reflecting on the most important results.

1. Introduction to Lattice QCD

As a first step, the basic concepts of lattice QCD are introduced, presenting the relevant theoretical principles of how this theory can be employed. First, a short section is devoted to an outline of continuum QCD, as lattice QCD is derived from it by discretizing the QCD action. The discretized Wilson gauge action and the staggered fermion action are presented in the following section, as only these discretizations were applied for this thesis. Additional sections discuss the simulation of a thermodynamic system of strong interacting matter, using thermal LQCD, and how the continuum and the thermodynamic limits are performed. Section 1.6 explains in more detail the relation between deconfinement and the center symmetry of pure gauge theory. Furthermore, the observable Polyakov loop is presented as the order parameter for the deconfinement transition. The approach to the theoretical principles and their notation used here is similar to those in the book *Quantum Chromodynamics on the Lattice* of C. Gattringer and B. Lang [17], which was used as the main reference for the topics presented in this chapter.

1.1. Continuum QCD

The continuum QCD is the quantum field theory within the Standard Model, which describes the physics of particles, interacting through the strong force. On the elementary particles level, these are the quarks and the gluons. Formulating the quantum field theory QCD, the path integral formalism for fermionic and bosonic fields is used as a basic concept. A discussion of the path integral formalism is omitted here, but detailed information about it can be found in chapter 1 of [17].

Take notice, that throughout this and the following sections, the Euclidean space-time is used instead of the Minkowski space-time. The Euclidean space-time can be obtained by performing a Wick-rotation, implying a switch from real time τ to imaginary time $t = i\tau$. Thus, the action occurring in the path integrals is the Euclidean action S_E , which relates to the usual action as $S_E = -i S|_{\tau=-it}$. Before starting the discussion, the Euclidean action for QCD is formulated. The fields for the gluons and quarks, occurring in the QCD action, have to be introduced first.

Quarks are massive fermions and can be described by Dirac 4-spinors. The notation for quarks is

$$\psi^{(f)}(x)_\alpha, \quad \bar{\psi}^{(f)}(x)_\alpha. \quad (1.1)$$

In contrast to the Minkowskian path integral approach, the quark fields are not related by $\bar{\psi} = \psi^\dagger \gamma_0$, where γ_0 is the γ -matrix related to time. Instead, they are independent integration variables for the Euclidean path integral. The Dirac indices are denoted by $\alpha \in \{1, 2, 3, 4\}$. The fundamental color index is $c \in \{1, 2, 3\}$ for $SU(N_c=3)$ gauge theory, where N_c is the number of colors. The last index $f \in \{1, 2, \dots, 6\}$ represents the flavors up, down, strange, charm, bottom and top, which differ in physical mass and electrical charge. The electrical charge, however, is irrelevant for the formulation of QCD. x is a

four dimensional Euclidean vector representing the space-time position of the spinors. The gauge fields, describing the gluons are denoted by

$$A_\mu(x)_{cd}, \quad (1.2)$$

where $\mu \in \{1, 2, 3, 4\}$ is a Euclidean Lorentz index and x is again the space-time position of the gauge field. The gluon carries two color indices c, d , turning it into a 3×3 -matrix at each space-time point x and in each direction μ .

Now, the Euclidean action of QCD can be set up by distinguishing between the fermionic and the gauge parts $S_F[\psi, \bar{\psi}, A]$ and $S_G[A]$, respectively:

$$S_{QCD}[\psi, \bar{\psi}, A] = S_F[\psi, \bar{\psi}, A] + S_G[A] \quad (1.3)$$

The fermionic part of the QCD action reads

$$S_F[\psi, \bar{\psi}, A] = \sum_{f=1}^{N_f} \int d^4x \bar{\psi}^{(f)}(x)_\alpha \left[(\gamma_\mu)_{\alpha\beta} (\delta_{cd} \partial_\mu + iA_\mu(x)_{cd}) + m^{(f)} \delta_{\alpha\beta} \delta_{cd} \right] \psi^{(f)}(x)_\beta, \quad (1.4)$$

using the Einstein summation convention. The space-time integral is taken over the whole Euclidean space-time volume. The number of flavors is specified by N_f , allowing to include only the lightest quarks for some calculations. The masses of the quark flavors are denoted by $m^{(f)}$. The γ_μ are the 4×4 Euclidean γ -matrices in Dirac space, obeying the Euclidean anti-commutation relations $\{\gamma_\mu, \gamma_\nu\} = 2\delta_{\mu\nu}\mathbb{1}$. The partial derivative in μ direction $\frac{\partial}{\partial x^\mu}$ is abbreviated as ∂_μ . One property of the massless fermion action is the invariance under chiral transformations

$$\psi \rightarrow \psi' = e^{i\alpha\gamma_5}\psi, \quad \bar{\psi} \rightarrow \bar{\psi}' = \bar{\psi}e^{i\alpha\gamma_5}, \quad (1.5)$$

where α is a real constant parameter and γ_5 is the chirality matrix. Here, this symmetry is covered briefly, because the spontaneous breaking of the chiral symmetry and the corresponding order parameter, the chiral condensate $\langle \bar{\psi}\psi \rangle$, only appear in the description of the Columbia plot in section 2.3. More details on this symmetry can be found in [17].

The gauge action is obtained by introducing the field strength tensor $F_{\mu\nu}(x)$, which in turn requires the introduction of the covariant derivative $D_\mu(x)$. The covariant derivative is already part of the fermionic action and reads

$$D_\mu(x) = \partial_\mu + iA_\mu(x) \quad (1.6)$$

in matrix notation. Using this expression, the field strength tensor can be expressed using the commutator

$$F_{\mu\nu}(x) = -i[D_\mu(x), D_\nu(x)] = \partial_\mu A_\nu(x) - \partial_\nu A_\mu(x) + i[A_\mu(x), A_\nu(x)]. \quad (1.7)$$

Having defined the field strength tensor, the gauge action reads

$$S_G[A] = \frac{1}{2g^2} \int d^4x \text{Tr}[F_{\mu\nu}(x)F_{\mu\nu}(x)], \quad (1.8)$$

where the trace is taken in color space and g is the bare gauge coupling. g appears in an overall factor in the gauge action, since rescaled gauge fields $gA_\mu(x) \rightarrow A_\mu(x)$ are used. Again, the integral is taken over the whole Euclidean space-time volume.

Since QCD is a Yang-Mills gauge theory, the corresponding gauge symmetry transformation has to be considered. The QCD-action is invariant under local gauge transformations of the special unitary group $SU(3)$, which transforms the fermionic fields according to

$$\psi(x) \rightarrow \psi'(x) = \Omega(x)\psi(x), \quad (1.9)$$

$$\bar{\psi}(x) \rightarrow \bar{\psi}'(x) = \bar{\psi}(x)\Omega(x)^\dagger. \quad (1.10)$$

The gauge fields transformation property is

$$A_\mu(x) \rightarrow A'_\mu(x) = \Omega(x)A_\mu(x)\Omega(x)^\dagger + i(\partial_\mu \Omega(x))\Omega(x)^\dagger. \quad (1.11)$$

It can be shown, that these transformations leave the actions S_F and S_G invariant.

The $A_\mu(x)$ are traceless hermitian matrices and elements of the Lie algebra $\mathfrak{su}(N_c=3)$, leading to $N_c^2 - 1 = 8$ gluons. This becomes clear, when writing the $A_\mu(x)$ as linear combinations of the color components $A_\mu^{(i)}(x)$ and the generators T_i :

$$A_\mu(x) = \sum_{i=1}^8 A_\mu^{(i)}(x)T_i \quad (1.12)$$

The generators T_i are a basis for traceless hermitian 3×3 matrices, obeying the commutation relations $[T_i, T_j] = if_{ijk}T_k$, with the anti-symmetric structure constants f_{ijk} .

Having introduced the Euclidean action for QCD, now its appearance in the path integrals is discussed, which have to be solved somehow to calculate QCD observables. The vacuum expectation value of a gauge observable $O[A]$ is given by

$$\langle O \rangle = \frac{1}{Z} \int \mathcal{D}[\psi, \bar{\psi}] \mathcal{D}[A] e^{-S_F[\psi, \bar{\psi}, A] - S_G[A]} O[A], \quad (1.13)$$

where the partition function Z is given by

$$Z = \int \mathcal{D}[\psi, \bar{\psi}] \mathcal{D}[A] e^{-S_F[\psi, \bar{\psi}] - S_G[A]}. \quad (1.14)$$

The path integral measure for the fermionic fields is denoted as $\mathcal{D}[\psi, \bar{\psi}]$, whereas the path integral measure for the gauge field is denoted as $\mathcal{D}[A]$. A definition of the path integral measure will be introduced for the lattice formulation of QCD in the next section 1.2 (see equation (1.33)). Another important quantity is the Euclidean correlator

$$\begin{aligned} & \langle O_2(t)O_1(0) \rangle \\ &= \frac{1}{Z} \int \mathcal{D}[\psi, \bar{\psi}] \mathcal{D}[A] e^{-S_F[\psi, \bar{\psi}] - S_G[A]} O_2[\psi(\cdot, t), \bar{\psi}(\cdot, t), A(\cdot, t)] O_1[\psi(\cdot, 0), \bar{\psi}(\cdot, 0), A(\cdot, 0)]. \end{aligned} \quad (1.15)$$

The functional $O[\psi(\cdot, t)]$ is evaluated for the field ψ at all spatial positions, depicted by a dot \cdot and at a certain time t . In general the QCD path integrals (1.13) - (1.15) can not be solved analytically. That is why the space-time is discretized, enabling the numerical approximation of the path integrals. Possible discretizations for the actions, introduced in this section, are discussed in the next section 1.2.

1.2. Lattice QCD

To obtain a lattice formulation of QCD, the first step is the definition of the 4D hypercubic lattice Λ , discretizing the space-time:

$$\Lambda = \{n = (n_1, n_2, n_3, n_4) | n_1, n_2, n_3 = 0, 1, \dots, N_s - 1; n_4 = 0, 1, \dots, N_\tau - 1\} \quad (1.16)$$

The vectors n are related to the physical space-time point by $x = an$, where a is the lattice spacing. The first three components of n are the spatial components and n_4 is the temporal component. The space-time integrals in both of the continuum actions (1.4) and (1.8) turn into sums over the index $n \in \Lambda$ in the discretized formulation. The spinors $\psi, \bar{\psi}$ are placed on the lattice points, thus, with the space time index n as the only argument, the fermion fields can be written as

$$\psi(n), \bar{\psi}(n), \quad n \in \Lambda. \quad (1.17)$$

As in the continuum fermion action (1.4), a space-time derivative occurs, a discretized version of ∂_μ has to be found as well. An expression of the discretization of ∂_μ is the symmetric one

$$\partial_\mu \rightarrow \frac{1}{2a}(\psi(n + \hat{\mu}) - \psi(n - \hat{\mu})), \quad (1.18)$$

with $\hat{\mu}$ being the unit vector in μ -direction. It can be shown, however, that this discretization of ∂_μ does not preserve the gauge invariance of the fermion action, which necessitates the introduction of gauge links $U_\mu(n)$. Their $SU(3)$ gauge transformation is defined as

$$U_\mu(n) \rightarrow U'_\mu(n) = \Omega(n)U_\mu(n)\Omega(n + \hat{\mu})^\dagger, \quad (1.19)$$

with $\Omega \in SU(3)$. The link variables $U_\mu(n)$ connect the lattice sites n and $n + \hat{\mu}$ with a certain orientation. The reversed link variable is defined as $U_{-\mu}(n) = U_\mu(n - \hat{\mu})^\dagger$. The relation of the gauge links to the continuum gauge fields $A_\mu(x)$ is given by

$$U_\mu(n) = \exp(iaA_\mu(n)), \quad (1.20)$$

thus being elements of the group $SU(3)$. In lattice QCD, the gluonic degrees of freedom are represented by the gauge links $U_\mu(n)$, being group-valued fields instead of the algebra-valued fields $A_\mu(x)$ in the continuum QCD.

As now the gluons can be represented on the lattice, a discretized gauge action is introduced. Hence, a construct built from gauge links is required, which is called the plaquette $U_{\mu\nu}(n)$. It is a product of four gauge links, forming a square of links, starting at lattice site n and expanding in the directions μ and ν

$$U_{\mu\nu}(n) = U_\mu(n)U_\nu(n + \hat{\mu})U_\mu(n + \nu)^\dagger U_\nu(n)^\dagger. \quad (1.21)$$

Subsequently, the Wilson gauge action [38] can be formulated as

$$S_G[U] = \frac{2}{g^2} \sum_{n \in \Lambda} \sum_{\mu < \nu} \text{Re Tr}[\mathbb{1} - U_{\mu\nu}(n)], \quad (1.22)$$

where the sum over Lorentz indices is constrained to $1 \leq \mu < \nu \leq 4$ and the trace is taken in color space. It can be shown, that this lattice gauge action turns into the

continuum gauge action (1.8), when performing the continuum limit $a \rightarrow 0$. For this proof, see *Quantum Chromodynamics on the Lattice* by C. Gattringer and C. B. Lang [17].

The discretized fermion action (1.4), in general, has the form

$$S_F[\psi, \bar{\psi}, U] = a^4 \sum_{n, m \in \Lambda} \sum_{\substack{\alpha, \beta \\ a, b}} \bar{\psi}(n)_\alpha D(n|m)_{\alpha\beta} \psi(m)_\beta, \quad (1.23)$$

where $D(n|m)_{\alpha\beta}$ is the Dirac operator with the Dirac indices α and β and the color indices a and b . From now on, the sum over the flavor index is omitted, thus only considering one flavor in the fermion action. Finding such a Dirac operator is not simple, as the naive replacement of the continuum covariant derivative with the symmetric expression (1.18) of the derivative and the gauge links

$$\partial_\mu + iA_\mu(n) \rightarrow \frac{U_\mu(n)\delta_{n+\hat{\mu}} - U_{-\mu}(n)\delta_{n-\hat{\mu}}}{2a} \quad (1.24)$$

and calculating the lattice fermion propagator leads to doublers. Doublers are unwanted poles in the quark propagator, which is the inverse of the Dirac operator. Only one pole, corresponding to the single fermion described by the continuum fermion action, exists in the continuum quark propagator. The naive discretization (1.24) of the Dirac operator gives rise to another 15 unwanted poles, which have to be removed from the theory. Kenneth G. Wilson found a solution to this problem by introducing the Wilson fermion action, but here, only the staggered lattice fermion action is considered, as it is the only one employed for this master's thesis.

The idea of the staggered action was first proposed by John Kogut and Leonard Susskind in 1975 [22]. The staggered transformation of the spinor fields

$$\psi(n) = \gamma_1^{n_1} \gamma_2^{n_2} \gamma_3^{n_3} \gamma_4^{n_4} \psi(n)' \quad (1.25)$$

$$\bar{\psi}(n) = \bar{\psi}(n)' \gamma_4^{n_4} \gamma_3^{n_3} \gamma_2^{n_2} \gamma_1^{n_1} \quad (1.26)$$

with $n = (n_1, n_2, n_3, n_4)$ is applied to the naive discretization of the fermion action. The formula for this naive fermion action is

$$S_F[\psi, \bar{\psi}, U] = a^4 \sum_{n \in \Lambda} \bar{\psi}(n) \left(\sum_{\mu=1}^4 \gamma_\mu \frac{U_\mu(n)\psi(n + \hat{\mu}) - U_\mu^\dagger(n - \hat{\mu})\psi(n - \hat{\mu})}{2a} + m\psi(n) \right), \quad (1.27)$$

which is formulated here to better explicate the application of the staggered transformation. This transformation mixes the spinor and space-time indices to reduce the 16-fold degeneracy of the naive fermion discretization.

Using the property of the γ -matrices $\gamma_\mu^2 = \mathbb{1}$, it is clear that the mass term is invariant. The derivative term in (1.27) with the additional γ -matrix can best be expressed by introducing the so called staggered sign function

$$\eta_\mu(n) = \begin{cases} 1 & \text{if } \mu = 1 \\ (-1)^{\sum_{k=1}^{\mu-1} n_k} & \text{for } \mu = 2, 3, 4, 5. \end{cases} \quad (1.28)$$

The product of the γ -matrices for the first symmetric derivative term turns into

$$\gamma_4^{n_4} \gamma_3^{n_3} \gamma_2^{n_2} \gamma_1^{n_1} \gamma_\mu \gamma_1^{n_1 + \hat{\mu}_1} \gamma_2^{n_2 + \hat{\mu}_2} \gamma_3^{n_3 + \hat{\mu}_3} \gamma_4^{n_4 + \hat{\mu}_4} = \mathbb{1} \eta_\mu(n), \quad (1.29)$$

which can be shown, using the anti-commutation relations of the γ -matrices $\{\gamma_\mu, \gamma_\nu\} = 2\delta_{\mu\nu}$. The second term of the derivative evaluates to the same result. Subsequently, the staggered sign function (1.28) replaces the γ -matrices. The Dirac operator is now diagonal in Dirac space and assumes the same form for all components. By discarding 3 of the 4 identical components, the initially 16 quark degrees of freedom (doubblers) are reduced to 4 remaining ones. The new action can be written with the new quark-fields $\chi(n), \bar{\chi}(n)$ without the Dirac structure

$$S_F[\chi, \bar{\chi}, U] = a^4 \sum_{n \in \Lambda} \bar{\chi}(n) \left(\sum_{\mu=1}^4 \eta_\mu(n) \frac{U_\mu(n) \chi(n + \hat{\mu}) - U_\mu^\dagger(n - \hat{\mu}) \chi(n - \hat{\mu})}{2a} + m \chi(n) \right). \quad (1.30)$$

By analyzing this staggered action (referring to chapter 10 of *Quantum Chromodynamics on the Lattice* [17]), it is found that the action describes 4 different species of quarks, named the tastes of staggered fermions. They live on a coarser lattice with lattice spacing $b = 2a$.

Another aspect concerns the fermion determinant, which is obtained by integrating out the Grassmann valued quark fields. The fermion determinant denotes the determinant of the Dirac operator, whose derivation can be seen in *Quantum Chromodynamics on the Lattice* [17], chapter 5. It can be shown that the fermion determinant for staggered fermions is real and strictly positive. This property enables the application of Monte Carlo importance sampling for the staggered formulation (see section 3.1.1). Except for a taste-breaking term, which becomes apparent when analyzing this discretization, the staggered action describes four degenerate quarks. However, to achieve the simulation of a theory with different quark flavors or a different number of degenerate quarks, the rooting trick can be applied. Here, the fourth root of the fermion determinant is raised to the power of the number of degenerate quarks to be simulated. This rooting trick has not yet been proven to be correct and indeed, there are some conceptual issues. Furthermore, in a naive continuum limit the taste-breaking term would vanish, but it is not clear, whether effects of the taste-breaking term survive in the true continuum limit for actual calculations. These problems are beyond this thesis and will not be discussed here. However, the comparison of results from staggered simulations and experimental results has shown good agreement (e.g. [4]).

After having introduced the discretizations of the gauge action and the fermion action, the lattice counterpart of the path integrals in the continuum is considered, which calculate the expectation value of a gauge observable (1.13). For convenience, a rooted staggered fermion determinant $\det[D^{(stagg.)}]^{1/2}$, describing 2 degenerate quark flavors, is chosen. The expectation value of a gauge observable $O[U]$ is

$$\langle O \rangle = \frac{1}{Z} \int \mathcal{D}[U] e^{-S_G[U]} \det[D^{(stagg.)}]^{1/2} O[U], \quad (1.31)$$

with the partition function

$$Z = \int \mathcal{D}[U] e^{-S_G[U]} \det[D^{(stagg.)}]^{1/2}. \quad (1.32)$$

The path integral measure is defined as

$$\mathcal{D}[U] = \prod_{n \in \Lambda} \prod_{\mu=1}^4 dU_\mu(n), \quad (1.33)$$

where the measure for a single link variable is $dU_\mu(n)$, denoting an integration over the group manifold $SU(3)$. How to calculate an approximation for the type of the path integrals (1.31) and (1.32), is subject of section 3.1.1.

1.3. Finite Temperature LQCD

The finite temperature LQCD can be introduced easily, as it shares the same path integral techniques as the vacuum LQCD. The partition function for a statistical system with temperature T is given by

$$Z(T) = \text{Tr} \left[e^{-\hat{H}/(k_B T)} \right], \quad (1.34)$$

with the Hamiltonian \hat{H} and the Boltzmann constant k_B , which can be set to $k_B = 1$ in natural units. This partition function can be transformed to a path integral in the same manner as for the Euclidean vacuum LQCD, but with the difference of a finite Euclidean time interval $[0, 1/T]$. The time extent does not become infinite anymore, instead it is connected to the temperature. In addition, the fields have to be periodic in time for bosons and anti-periodic for fermions. Often, periodic boundary conditions are also used in the spatial directions. The finite temperature partition function is

$$Z(T) = \int \mathcal{D}[U] \mathcal{D}[\psi, \bar{\psi}] e^{-S_E[\psi, \bar{\psi}, U]}, \quad (1.35)$$

where S_E is the Euclidean action, being expressed as an integral of the Euclidean Lagrangian \mathcal{L}_E

$$S_E[\psi, \bar{\psi}, U] = \int_0^{1/T} dt \int d^3x \mathcal{L}_E[\psi, \bar{\psi}, U]. \quad (1.36)$$

Applying the space-time discretization, it is recognized, that the number of lattice points in temporal direction is given by

$$aN_\tau = \frac{1}{T}. \quad (1.37)$$

The number of lattice sites in spatial direction $N_s = N_x = N_y = N_z$ is the same for every direction, since there is no reason to treat any direction individually. The number of temporal lattice sites N_τ differs explicitly, as it determines the temperature. However, N_s and N_τ cannot be chosen completely independent from each other. Their relation follows from considering the correlation length ξ of the statistical system. Roughly speaking, the correlation length is a measure for the distance, over which two spins are correlated with each other. Clearly, it is beneficial, if the correlation length fulfills

$$a \ll \xi \ll aN_s, \quad (1.38)$$

implying, that the correlations can be resolved by the lattice spacing a and are not bounded from above by the physical box length of the system. The relevant length scale in deconfined QCD matter is the Debye screening length, which is the inverse Debye screening mass. For Debye screening in the QCD plasma see [26]. The Debye screening mass m_D has been found to be proportional to the temperature T . Inserting the inverse Debye screening mass (the inverse temperature) into inequality (1.38) and division by a , leads to

$$1 \ll N_\tau \ll N_s. \quad (1.39)$$

This inequality, with the strong \ll , can not be fulfilled in realistic simulations, as the lattices would become much too large and so would the computational cost. Therefore, an evaluation of the finite size effects and the lattice artifacts should be done carefully (see section 1.4). The aspect ratio

$$\frac{N_s}{N_\tau} \quad (1.40)$$

is used to compare the simulations of different N_τ , but at the same temperature, with respect to their physical box length. To tune the temperature of the system, it is not convenient to alter the integer valued N_τ . On the lattice, the temperature also depends on the lattice spacing a (see equation (1.37)), thus, the temperature can be adjusted by tuning a . This is done implicitly by tuning the inverse gauge coupling

$$\beta = \frac{6}{g^2}. \quad (1.41)$$

This is motivated by the fact, that the bare parameters like g and m of the theory have a nontrivial dependence on the cutoff, the lattice spacing a . Therefore, the parameter β is used to tune the temperature, while keeping N_τ constant.

1.4. Continuum and Thermodynamic Limit

To relate the results of a lattice gauge theory to the continuum gauge theory, two important limits have to be taken. By reducing the lattice spacing $a \rightarrow 0$, the continuum limit is achieved. In the thermodynamic limit, the box size of the system is extended $N_s \rightarrow \infty$. Systematic errors of the lattice gauge theory due to a finite lattice spacing are referred to as lattice artifacts. The errors, which occur due to the finite size of the physical box, are called finite-size effects. Both systematic errors can be estimated by taking the continuum and the thermodynamic limit. Another aspect, illustrating the importance of taking both limits, is the lattice momentum. On the lattice with periodic boundary conditions, the momenta are discrete due to the finite size of the lattice volume and, when considering plane waves, they assume the values

$$p_\mu = n_\mu \frac{2\pi}{aN_\mu}, \quad n_\mu \in \mathbb{Z}, \quad (1.42)$$

with μ indicating the lattice directions. The discrete space-time lattice with lattice spacing a leads to the momentum cutoff $\frac{2\pi}{a}$ at the border of the first Brillouin zone.

The two limits are usually performed in a certain order, first the thermodynamic limit and thereafter the continuum limit. While performing the thermodynamic limit, the number of spatial lattice points is sent to ∞ and the other parameters are kept fixed

$$N_s \rightarrow \infty, \quad N_\tau \text{ fixed}, \quad a \text{ fixed} \quad \rightarrow \quad T \text{ fixed}, \quad (1.43)$$

such that the temperature is the same for all volumes N_s with the variable physical box length $L = aN_s$. Performing the thermodynamic limit becomes especially important for statistical systems near critical points, as will be seen in section 2.1. When taking the continuum limit, the temperature again and also the physical box length shall be kept fixed. This is achieved by performing the limits

$$N_s \rightarrow \infty, \quad N_\tau \rightarrow \infty, \quad a \rightarrow 0, \quad (1.44)$$

with the constraint, that the products

$$aN_s = L, \quad aN_\tau = \frac{1}{T} \quad (1.45)$$

are kept constant.

The question arises, how the lattice spacing a can be tuned to perform the continuum limit, as it is not a free parameter of the theory, but is rather determined by the simulation parameters. As QCD is an asymptotically free theory, the coupling becomes small at short distances. Hence, in the continuum limit, the bare gauge coupling also vanishes $g \rightarrow 0$, implying, that the inverse gauge coupling $\beta \rightarrow \infty$. Effectively, the continuum limit is performed by increasing N_τ and keeping the aspect ratio $N_s/N_\tau = LT$. To keep the temperature constant, β is increased. The β values for different N_τ , corresponding to the same temperature, are found indirectly. After guessing β values, the temperature has to be determined by setting the scale (see section 1.5). In some cases, the identification of certain phase transitions determines the value of β and thus the temperature, at which the simulations are performed.

1.5. Scale Setting

Lattice QCD calculations yield quantities in lattice units, which need to be transformed into physical units to make physical statements. It is sufficient to determine the scale parameter, which in lattice calculations is the lattice spacing a and can be determined by relating an experimental mass value $M^{exp.}$ to the value obtained by the lattice calculation $(aM)^{latt.}$

$$a = \frac{(aM)^{latt.}}{M^{exp.}}. \quad (1.46)$$

Hadron masses in lattice units $(aM)^{latt.}$ are calculated, using the Euclidean correlator from equation (1.15). However, this method fails, if the lattice QCD calculation is performed at an unphysical combination of parameters of the theory, e.g. the quark masses. Alternatively, the scale can be set, using the Sommer parameter r_0 , which is related to the static quark potential $V(r)$ discussed in section 1.6 (see equation (1.53)). Experimentally, it has been found, that

$$\left. \frac{dV(r)}{dr} \right|_{r_0} r_0^2 = 1.65 \quad (1.47)$$

corresponds to $r_0 \approx 0.5$ fm. Being able to evaluate the dimensionless product $\frac{dV(r)}{dr} r^2$ on the lattice, allows to set the scale.

However, for this thesis, the scale is set, using the w_0 scale [6], which is based on the Wilson flow [23]. Compared to the Sommer scale r_0 , it has one main advantage: w_0 can be determined with a higher precision, due to the absence of fitting to asymptotic time behavior of correlators (i.e. Wilson loops (see section 1.6)) and the missing signal-to-noise issues. Additionally, the w_0 scale has only small cutoff effects and the method is generally very fast.

The w_0 scale is derived according to [6] and in physical units it is

$$w_0 = 0.1755(18)\text{fm}, \quad (1.48)$$

with the statistical error in brackets. Subsequently, the scale is set by calculating $(w_0/a)^{(latt.)}$ on the lattice and a is determined by

$$a = \frac{w_0}{(w_0/a)^{(latt.)}}. \quad (1.49)$$

The error on the lattice spacing a can be determined by the usual propagation of uncertainty.

1.6. Deconfinement and the Center Symmetry

At low temperatures, QCD is a confining theory. The asymptotic freedom of QCD guarantees, that at some temperature the thermal QCD phase transition separates the confined phase from the gas of quasi-free quarks and gluons. More qualitative aspects of this phase transition will be subject of section 2.2, as in this section, observables and the center symmetry related to the deconfinement transition will be discussed. The two important observables are the Wilson loop and the related Polyakov loop.

The Wilson loop is a product of gauge links $U_\mu(n)$ forming a loop. Four different parts in this product can be distinguished. There are two spatial transporters of the type

$$S(\mathbf{n}, \mathbf{m}, n_\tau) = \prod_{(\mathbf{k}, \nu) \in \mathcal{C}_{\mathbf{n}, \mathbf{m}}} U_\nu(\mathbf{k}, n_\tau), \quad (1.50)$$

which connect two spatial points \mathbf{n}, \mathbf{m} in the same time slice n_τ via the path $\mathcal{C}_{\mathbf{n}, \mathbf{m}}$. Furthermore, there are two temporal transporters of the type

$$T(\mathbf{n}, n_\tau) = \prod_{j=0}^{n_\tau-1} U_4(\mathbf{n}, j), \quad (1.51)$$

which are straight lines of n_τ gauge links in temporal direction at the spatial site \mathbf{n} . With these components, the Wilson loop is the trace of a closed loop \mathcal{L} of gauge links

$$W_{\mathcal{L}}[U] = \text{Tr}[S(\mathbf{n}, \mathbf{m}, n_\tau)T(\mathbf{m}, n_\tau)^\dagger S(\mathbf{n}, \mathbf{m}, 0)^\dagger T(\mathbf{n}, n_\tau)]. \quad (1.52)$$

The physical interpretation of the Wilson loop is given by its relation to the static quark potential. The static quark potential of an quark-antiquark-pair at distance $r = a|\mathbf{n} - \mathbf{m}|$ and temporal extent $t = an_\tau$ is denoted by $V(r)$. The expectation value of the Wilson loop can be shown to be

$$\langle W_{\mathcal{L}} \rangle \propto e^{-tV(r)} (1 + \mathcal{O}(e^{-t\Delta E})), \quad (1.53)$$

where ΔE is the difference between $V(r)$ and the first excited energy level of the quark-antiquark-pair.

The Polyakov loop is closely related to the Wilson loop. On a lattice with boundary conditions in temporal direction, the temporal extent of the Wilson loop is set to the maximum $n_\tau = N_\tau$. The spatial transporters $S(\mathbf{n}, \mathbf{m}, N_\tau)$ and $S(\mathbf{n}, \mathbf{m}, 0)^\dagger$ become basically the same, but the orientation is opposite. Performing gauge transformations of the type (1.19), the spatial transporters can be transformed to $\mathbb{1}$. Subsequently, the Wilson loop consists of two disconnected paths, which are closed on their own, as they

wind around the temporal direction. For the definition of the Polyakov loop, the trace is taken for only one of such closed loops in temporal direction. The Polyakov loop is expressed as

$$P(\mathbf{n}) = \text{Tr} \left[\prod_{j=0}^{N_\tau-1} U_4(\mathbf{n}, j) \right]. \quad (1.54)$$

The physical interpretation of the Polyakov loop is evident from evaluating the correlator $\langle P(\mathbf{m})P(\mathbf{n})^\dagger \rangle$ for pure gauge theory with static quarks. At a given temperature T , it is related to the free energy of $F_{\bar{q}q}(r)$ of a quark-antiquark-pair at a distance $r = a|\mathbf{n} - \mathbf{m}|$ via

$$\langle P(\mathbf{m})P(\mathbf{n})^\dagger \rangle = \exp(-F_{\bar{q}q}(r)/T). \quad (1.55)$$

At a large distance $r \rightarrow \infty$, the expectation value factorizes, such that the spatial position becomes irrelevant due to translational invariance and

$$|\langle P \rangle|^2 = \lim_{r \rightarrow \infty} \exp(-F_{\bar{q}q}(r)/T). \quad (1.56)$$

The difference of the free energy of two thermodynamic systems gives the work required to transform one system into the other. For QCD in the confined phase, the work to place an infinitely separated quark-antiquark-pair into the system is ∞ , whereas in the deconfined phase it becomes finite. With equation (1.56), this leads to the conclusion for the expectation value of the Polyakov loop

$$\langle P \rangle \begin{cases} = 0 & \Leftrightarrow \text{confinement,} \\ \neq 0 & \Leftrightarrow \text{deconfinement.} \end{cases} \quad (1.57)$$

Here, the Polyakov loop can be identified as an exact order parameter for the deconfinement phase transition of pure gauge theory.

The symmetry related to this phase transition in pure gauge theory is the center symmetry. It is a global symmetry of the Wilson gauge action (1.22), or in short, pure gauge theory is invariant under center transformations. These transformations involve all temporal links in one time slice n_τ , multiplying them with the same element z of the center group Z_3 of the gauge group $SU(3)$:

$$U_4(\mathbf{n}, n_\tau) \rightarrow zU_4(\mathbf{n}, n_\tau). \quad (1.58)$$

The center elements z can assume the values

$$z \in \{\mathbb{1}, \mathbb{1}e^{2\pi i/3}, \mathbb{1}e^{-2\pi i/3}\}. \quad (1.59)$$

The gauge action is constructed by plaquettes and the temporal plaquettes always contain two temporal gauge links in opposite direction. As $[z, U] = 0$ and $z^\dagger z = \mathbb{1}$, the center transformation leaves the plaquette and thus the gauge action invariant.

The situation with Polyakov loops is a bit different, as they don't close in a topologically trivial way. They wind around the compact time direction and pick up the factor z from the center transformation in one time slice

$$P(\mathbf{n}) \rightarrow zP(\mathbf{n}). \quad (1.60)$$

The expectation value of the Polyakov loop with the center element $z = \mathbb{1}e^{2\pi i/3}$ can be written as

$$\langle P \rangle = \frac{1}{3} \langle P + zP + z^2P \rangle, \quad (1.61)$$

because each prefactor z^n , $n \in \{0, 1, 2\}$, leads to the same probability weight. The sum can be calculated, resulting in

$$\langle P \rangle = \frac{1}{3} (1 + e^{2\pi i/3} + e^{-2\pi i/3}) \langle P \rangle = 0. \quad (1.62)$$

This calculation does not hold, if the center symmetry is broken. This is the case for the deconfined phase of the QCD phase diagram, as shown in equation (1.57).

With regards to the center symmetry, the system resembles a spin model with three possible states, being elements of Z_3 . The system is in one of the three sectors with equal probability, when being in the confined phase. For computer simulations, it might be difficult to tunnel between the sectors and therefore, the expectation value of the absolute value of the Polyakov loop $\langle |P| \rangle$ is the order parameter to be analyzed in this case. In the thermodynamic limit it coincides with $|\langle P \rangle|$.

The previous discussion was only considering pure gauge theory without dynamical fermions. Their inclusion into the theory breaks explicitly the Z_3 center symmetry, which is evident from the hopping expansion of the fermion determinant. The hopping expansion follows from the Wilson formulation of the Dirac operator in the limit of large quark masses. As described in detail in chapter 5 of [17], an important observation is, that the fermion determinant consists of a sum over all possible closed gauge link loops. This includes Polyakov loops, which were already found to be not invariant under non trivial center transformations, also affecting the Polyakov loop as an order parameter for the deconfinement transition. With dynamical fermions, the Polyakov loop is not an exact order parameter anymore, but rather an approximate one. This will play a crucial role in the discussion of the finite size scaling of the kurtosis of the Polyakov loop in section 3.1.5. Although the Polyakov loop is not a true order parameter anymore, it can still serve to investigate the deconfinement phase transition by analyzing its distribution.

2. The QCD Phase Diagram and the Columbia Plot

After having touched the deconfinement transition for pure gauge theory, in this chapter, the discussion of the deconfinement transition follows from the relation to the QCD phase diagram. The aim here is to give a brief overview over the conjectured QCD phase diagram and the Columbia plot. As in the QCD phase diagram different phases and phase transitions are represented and as the Columbia plot shows the type of the QCD thermal transition, first, the basic theory about phase transitions is introduced. Some general terms, particularly important for the discussion of phase transitions, as well as a brief overview of the types of phase transitions, are introduced in the first section 2.1. This theoretical basis will be helpful for sections 2.2 and 2.3 about the QCD phase diagram and the Columbia plot, respectively.

2.1. General Aspects about Phase Transitions

Some terms like first or second order phase transition and crossover have been used already, for example in the introduction. In this section the subject of phase transitions is approached more formally, describing the classification of different types of phase transitions. The most important properties distinguishing the types of phase transitions are presented. A large part of this section discusses the finite size scaling for a thermodynamic system near a critical point. This is justified by the importance of the finite size scaling formula of the reduced free energy density, which is derived in this section. Using this formula, the fit formulas for the kurtosis of the order parameter in sections 3.1.5 and 3.1.6 will be derived.

Many of the topics covered in this section are also treated in the book of Nigel Goldenfeld *Lectures on Phase Transitions and the Renormalization Group* [18], which gives a detailed and formal explanation of the occurrence of phase transitions and also covers the relation to the renormalization group. The book by John Cardy *Scaling and Renormalization in Statistical Physics* [9] much more concentrates on the idea of the renormalization group and the examination of phase diagrams, using critical phenomena from the renormalization group. Both books are given as references for this section.

The following sections rely on some important terms, which are briefly explained. Partition function refers to the canonical partition function

$$Z = \text{Tr} \left(e^{-\frac{\hat{H}}{T}} \right), \quad (2.1)$$

depending on the temperature T and the Hamiltonian \hat{H} of the system. Important thermodynamic quantities are derived from the partition function. The free energy refers

to the Helmholtz free energy $F = U - TS$, U denoting the inner energy and S the entropy of the system, and can be expressed in terms of the partition function

$$F = -T \ln Z. \quad (2.2)$$

One very well investigated thermodynamic system of interacting spins S_i at discrete lattice sites i is the Ising model with its Hamiltonian

$$\tilde{H} = -J \sum_{\langle i,j \rangle} S_i S_j - H \sum_i S_i. \quad (2.3)$$

The sum over $\langle i, j \rangle$ denotes nearest neighbors i and j , whose interaction strength is given by J , and the magnetic field H couples to all spins equally. The Hamiltonian of the Ising model is invariant under the Z_2 -symmetry if the magnetic field is zero. It corresponds to a flip of the sign for all spin variables S_i . For this model, the magnetization can be given by

$$M = \frac{1}{N} \sum_i^N S_i, \quad (2.4)$$

where N is the total number of spins. Another important term is the correlation length, which is a measure for the distance, over which two spins in such a spin system are correlated. A more precise definition of the correlation length ξ follows from the asymptotic behavior $r \rightarrow \infty$ of the correlation function

$$C(r) \propto \frac{e^{-r/\xi}}{r^{(d-1)/2}}, \quad (2.5)$$

where r is the spatial distance of two spins and d is the spatial dimension of the system. The context of these terms has not yet been clarified, but they become relevant in the following.

2.1.1. Types of Phase Transitions

It is useful to reflect on the definition of phases and phase boundaries. A state of a system in the thermodynamic equilibrium, being characterized by its macroscopic properties, is denoted as a phase. One and the same substance can be found in several distinct phases, depending on the intensive thermodynamic properties. While the microscopical interactions between particles are identical in these phases, the macroscopic properties like density or magnetization differ significantly.

The phases can be represented in the phase diagram, whose axes correspond to the thermodynamic parameters of the theory, e.g. temperature and chemical potential. The dimension D of the phase diagram is determined by the number of those parameters. Phase boundaries separate the phases by being hyperplanes in the phase diagram of dimension $D - 1$ of non-analyticities in the free energy density f . Thus, phase boundaries in a 2-dimensional $p - T$ phase diagram are simply lines. A more subtle theoretical description of these terms can be found in chapter 2 of [18]. Phase transitions describe the evolution of a system into another phase by crossing the phase boundary. It has to be noted, that phase transitions can only occur in the thermodynamic limit. A simple explanation considers the partition function, from which the thermodynamic potentials

like the free energy can be derived. At first sight, non-analyticities in the partition function, which is basically a sum over exponentials, are not expected. However, in the infinite volume limit, this sum becomes infinite and can thus exhibit singularities. This also implies, that phase transitions in finite volumes are smoothed and that an increasing system volume will sharpen the phase transition with respect to the parameters of the thermodynamic system.

The phase transitions can now be classified into categories, depending on how the macroscopic observables change, while crossing such a phase boundary. A classification introduced by Ehrenfest, while being deprecated, still has a large impact on the nomenclature of the types of phase transitions. Ehrenfest's classification claims, that a phase transition is of n th order, if any n th derivative of the free energy with respect to its arguments exhibits a discontinuity at the phase boundary and if all derivatives from first to $(n - 1)$ th order are continuous. This classification turned out to be problematic, because it was shown, that for second order phase transitions the second derivative of the free energy may not only be discontinuous, but may actually diverge at the critical point. For example, the specific heat is proportional to the second derivative of the free energy with respect to the temperature and it diverges at a second order phase transition. Therefore, the modern definition for second order phase transitions or continuous phase transitions is, that the first derivatives of the free energy are continuous, but in any of the second derivatives a non-analyticity has to exist, which can either be a discontinuity or even a singularity. First order phase transitions are also called discontinuous phase transitions, because they are discontinuous in any of the first derivatives of the free energy.

Having introduced a formal classification of phase transitions, some general properties of either type are discussed. The discontinuous or first order phase transition is characterized by the coexistence of two or more phases at the critical point. These phases are distinct from each other and have different macroscopic properties. Consequently, the phases fill distinct regions of the volume and the correlation length is generally finite. Discontinuous phase transitions often involve a latent heat, implying that the temperature stays constant, while the system releases or absorbs energy. This property is also reflected in the discontinuous behavior of the thermodynamic quantities. In this case, they are discontinuous with respect to a change in the temperature.

Contrary to the discontinuous phase transition, at a continuous phase transition the system is in a unique critical phase. When approaching the critical point, the correlation length diverges continuously until it effectively becomes infinite. Another important difference to the discontinuous phase transitions is, that thermodynamic quantities smoothly approach the same value from either side of the critical point. An example for a second order phase transition is the ferromagnetic transition at the Curie temperature T_C . When approaching this temperature from below, the spontaneous magnetization decreases continuously, until it becomes zero at T_C . Above T_C , the magnetization is always zero. The Ising model introduced above is a model, describing ferromagnetism and this second order phase transition.

Another important type of transition is the crossover transition. It is not a true phase transition, because it cannot be classified into one of the types of phase transitions presented above. The thermodynamic variables just change very rapidly in a small range around the critical temperature, but there are no non-analyticities in any of the derivatives of the free energy. The renormalization group is not discussed here in detail,

but the references [18] and [9] provide an explanation for crossover effects. Instead of discussing this explanation here, only some typical occurrences of crossovers are named. One example is the occurrence of crossovers for small residual fields, being present in the Hamiltonian of the system. If the symmetry related to a phase transition is broken by this external field explicitly and sufficiently strong, the system undergoes a crossover instead of a true phase transition. True phase transitions only occur in the thermodynamic limit, but nevertheless, a rapid change of the relevant thermodynamic variables can be observed in finite systems. This can also be called a crossover phenomenon or more explicitly finite-size crossover.

2.1.2. Finite Size Scaling

As explained in the previous section, real phase transitions only occur in the infinite volume limit. Nevertheless, if the volume is sufficiently large, signs of the real phase transition can be observed. Therefore, it is important to simulate systems with volumes as large as possible or to investigate the volume dependency. This is clearly restricted by the available computation time and capacity. The finite size scaling analysis quantifies the behavior of thermodynamic quantities near a critical point. It can be derived from the renormalization group framework, which also explains the term “critical point”.

In the following, the concept of the renormalization group framework will only be outlined, for more details see chapter 9 of [18]. The renormalization group (RG) transformations \mathcal{R} act on the coupling parameters $\{K\}$ of a system in thermodynamic limit, performing a coarse-graining. In this case, the real space is coarse-grained by a length factor of ℓ . Thus,

$$\{K'\} = \mathcal{R}_\ell\{K\} \quad (2.6)$$

describes how the coupling constants change, as the length scale is varied by ℓ . As the correlation length plays an important role for phase transitions, its transformation under \mathcal{R}_ℓ is given as

$$\xi[K'] = \xi[K]/\ell. \quad (2.7)$$

When considering a spin system on a lattice, it is clear, that this coarse-graining of the real space is also a coarse graining of the degrees of freedom. Hence, the transformation of the free energy density is of interest, as it is related to the partition function $Z_N[K]$, depending on the set of coupling parameters $\{K\}$. In the following the singular part of the reduced free energy density

$$\tilde{f}[K] = \frac{\tilde{F}[K]}{N} = \frac{1}{N} \ln(Z_N[K]), \quad (2.8)$$

is considered, with N being the number of degrees of freedom. The reduced free energy \tilde{F} relates to the usual free energy as $F = -\tilde{F}T$, with T being the temperature. It is necessary to consider the singular part of the reduced free energy density to obtain a homogeneous scaling law as in equation (2.9). It can be shown, that the partition function is invariant under an RG transformation leading to

$$\tilde{f}[K] = \ell^{-d} \tilde{f}[K'], \quad (2.9)$$

with d being the spatial dimension of the system.

Another crucial aspect are fixed points, emerging from RG transformations. A fixed point K^* is a point in coupling parameter space $\{K\}$ and is defined by

$$\{K^*\} = \mathcal{R}_\ell\{K^*\}. \quad (2.10)$$

This can be applied to the transformation equation of the correlation length (2.7)

$$\xi[K^*] = \xi[K^*]/\ell, \quad (2.11)$$

which has the only two solutions $\xi = 0$ and $\xi = \infty$. The first solution $\xi = 0$ refers to a trivial fixed point and the $\xi = \infty$ indicates a critical fixed point. The critical fixed points are important for the treatment of phase transitions, as they describe critical singular behavior and finding those fixed points, allows to determine the phase diagram.

Within the renormalization group framework, the scaling laws of the free energy density or derived quantities can be established in the vicinity of a critical point. These scaling laws incorporate several critical exponents, which hold an important peculiarity. The values are universal for all systems within a universality class. The renormalization group approach also explains the origin of universality, but here, just the definition of universality is given. The members of a universality class have three things in common. First, the spatial dimensions have to coincide. Secondly, the symmetry group of the Hamiltonian has to be the same for all members and crucially, the interaction forces have to be of similar range, either being long or short ranged. Particularly, the details of the type of interaction of the thermodynamic system do not play a role. Systems, belonging to the same universality class, can be described by universal scaling laws and critical exponents near a critical point.

Now, after having introduced the most important concepts and terms, the actual finite size scaling analysis for the reduced free energy density f can be performed. To obtain a finite size scaling formula with specific coupling parameters, a certain model is chosen. Here, the ferromagnetic Ising model is used, where the temperature T and the magnetic field H have to be adjusted to bring the system to its critical point. The reduced variables

$$t = \frac{T - T_c}{T_c}, \quad (2.12)$$

$$h = \frac{H}{T} \quad (2.13)$$

are introduced as they become zero, when the critical point is reached at the critical temperature T_c . The inverse spatial volume of the system L^{-1} can be treated as an additional parameter, as the finite size is expected to have an effect on the system. Like the other parameters of the system t and h , $L^{-1} \rightarrow 0$ has to be fulfilled to reach the critical point. Thus, in the vicinity of the critical point, the scaling law (2.9) is expressed as

$$\tilde{f}(t, h, L^{-1}) = \ell^{-d} \tilde{f}(t\ell^{y_t}, h\ell^{y_h}, \ell L^{-1}), \quad (2.14)$$

with y_t and y_h being the critical exponents to be determined. For n renormalization group transformations of the correlation length, it is found, that

$$\xi(t, h) = \ell^n \xi(\ell^{ny_t} t, \ell^{ny_h} h). \quad (2.15)$$

Considering the case $h = 0$ and setting $\ell^n = \left(\frac{b}{t}\right)^{1/y_t}$, as ℓ can be chosen arbitrarily, the correlation length is

$$\xi(t, 0) = \left(\frac{t}{b}\right)^{-1/y_t} \xi(b, 0). \quad (2.16)$$

b is some arbitrary positive number much larger than one. The behavior of ξ in the limit $t \rightarrow 0$ is found to be

$$\xi \propto |t|^{-\nu}, \quad (2.17)$$

where the critical exponent $\nu = 1/y_t$ was identified and the absolute value of t was used to include both cases $T < T_c$ and $T > T_c$. At this point, the values of the relevant critical exponents for the Ising 3D universality class are written down. The scaling relation

$$2(d - y_h) = d - 2 + \eta \quad (2.18)$$

also relates y_h to another critical exponent η , which is connected to the decay of the correlation function at the critical point. $d = 3$ is the spatial dimension of the system. This scaling relation, as well as others, can be found in *Lecture on Phase Transitions and the Renormalization Group* [18]. The values for four of these critical exponents can be seen in table 2.1; ν and η are taken from [25] and y_t and y_h are calculated by using the relations of the critical exponents mentioned above.

ν	y_t	η	y_h
0.6301(4)	1.5870(10)	0.0364(5)	2.4818(3)

Table 2.1.: Values of selected critical exponents obtained from numerical simulations for the Ising 3D universality class [25].

Again considering $h = 0$ and setting the arbitrary value of ℓ to

$$\ell = |t|^{-1/y_t}, \quad (2.19)$$

equation (2.14) turns into

$$\tilde{f}(t, L^{-1}) = |t|^{d/y_t} \tilde{f}(1, |t|^{-1/y_t} L^{-1}) = |t|^{d\nu} \tilde{f}(1, |t|^{-\nu} L^{-1}). \quad (2.20)$$

By identifying $\xi = |t|^{-\nu}$, except for an irrelevant constant factor, it becomes apparent, that the finite size scaling of the reduced free energy density only depends on the ratio $x = \frac{\xi}{L}$. The thermodynamic limit $x \rightarrow 0$ corresponds to the correct critical behavior, because the correlation length is not affected by the boundaries. Inserting these substitutions in equation (2.20), leads to

$$\tilde{f}(t, L^{-1}) = (xL)^{-d} \tilde{f}(1, x), \quad (2.21)$$

where a new scaling function

$$\phi(x^{-1/\nu}) = x^{-d} \tilde{f}(1, x) \quad (2.22)$$

is defined. The result is a finite size scaling form of the reduced free energy density

$$\tilde{f}(t, L^{-1}) = L^{-d} \phi(tL^{1/\nu}), \quad (2.23)$$

with the scaling variable $tL^{1/\nu}$, where the temperature t was recovered by employing equation (2.17) backwards. As this result was achieved by setting $h = 0$, a similar result can be obtained by setting $t = 0$ and performing an analogous calculation. Combining these results of the finite size scaling analysis for the reduced free energy density, the scaling formula (2.9) can be rewritten by setting $\ell = L$:

$$\tilde{f}(t, h, L^{-1}) = L^{-d} \tilde{f}(tL^{y_t}, hL^{y_h}, 1). \quad (2.24)$$

At last, the reduced free energy \tilde{F} is required instead of the reduced free energy density \tilde{f} , as well as its scaling behavior. Therefore, it is derived here in short. These quantities are related by

$$\tilde{f}(t, h, L^{-1}) = L^{-d} \tilde{F}(t, h, L^{-1}), \quad (2.25)$$

for which the relation (2.14) has to be inserted.

$$\begin{aligned} L^{-d} \tilde{F}(t, h, L^{-1}) &= \tilde{f}(t, h, L^{-1}) = \ell^{-d} \tilde{f}(t\ell^{y_t}, h\ell^{y_h}, \ell L^{-1}) \\ &= \ell^{-d} (\ell L^{-1})^d \tilde{F}(t\ell^{y_t}, h\ell^{y_h}, \ell L^{-1}) = L^{-d} \tilde{F}(t\ell^{y_t}, h\ell^{y_h}, \ell L^{-1}) \end{aligned} \quad (2.26)$$

leads to the result

$$\tilde{F}(t, h, L^{-1}) = \tilde{F}(tL^{y_t}, hL^{y_h}, 1). \quad (2.27)$$

This section is concluded by noting, that these derivations help to determine the scaling behavior of various thermodynamic observables. Especially the last formula (2.27) will be the starting point to obtaining a finite size scaling formula of the kurtosis, as will be seen in section 3.1.5.

2.2. The QCD Phase Diagram

Having introduced general terms of phase transitions, a closer look is taken at the QCD phase diagram and in particular the QCD thermal transition. Usually, the QCD phase diagram represents the phases and phase boundaries of QCD in the μ - T -plane, where μ is the baryonic chemical potential and T is the temperature. Quite early it was clear, that the hadronic phase, which is located in the low temperature and low baryonic chemical potential region, would not persist for high temperatures. Consequently, a line in the phase diagram should mark a transition from the hadronic phase to the quark-gluon-plasma (QGP). A possible explanation considers the asymptotic freedom of QCD. The running gauge coupling decreases for large energies or for large temperatures, where the quarks and gluons lose the confinement, which was present in the hadronic phase. The term plasma indicates the presence of free color charges.

The relevant energy scales of the QCD phase diagram prevent analysis by perturbation theory, because the gauge coupling is still large. Thus, the only first principles method to study the phase diagram at low temperatures and densities is lattice QCD, which is restricted to the $\mu=0$ line. Extrapolations from lattice results can only explore the region in the vicinity of $\mu=0$. For larger chemical potential, conclusions have to be drawn from symmetry arguments, or effective models have to be used to approximate the phase structure of QCD. Therefore, currently, the QCD phase diagram is only conjectured. Some simplifying assumptions reduce the complexity of the problem. First of all, the number of quark flavors is reduced to the 2 or 3 lightest quarks. The much heavier quarks

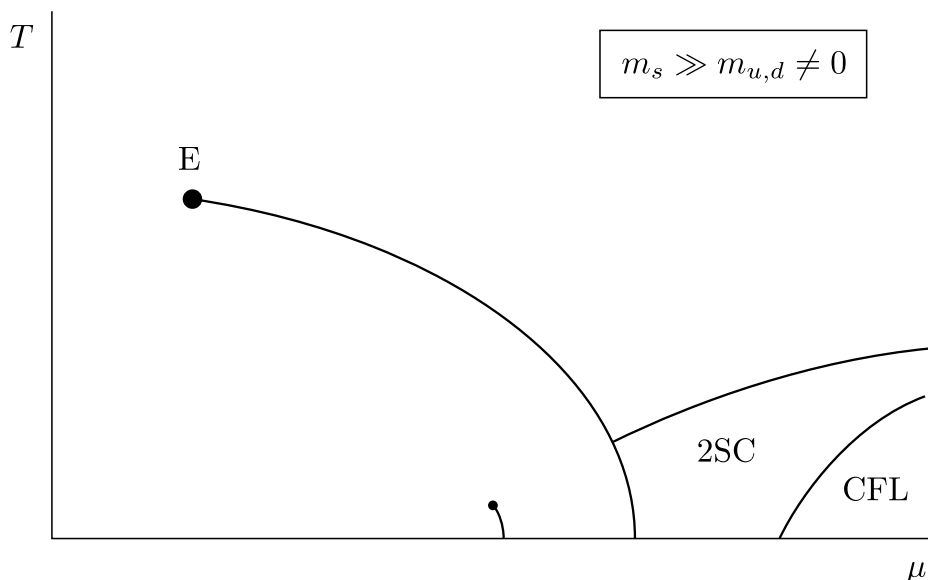


Figure 2.1.: The QCD phase diagram in the T - μ -plane in the approximation of two degenerate light quarks with finite quark mass $m_{u,d}$ and one heavier strange quark m_s , with mass values comparable to physical ones [29]. The two largest phases are the hadronic phase in the left lower corner and the quark gluon plasma for large temperatures. The terms 2SC and CFL stand for the color superconducting phases two-flavor-superconducting phase and the color-flavor-locked phase respectively.

charm, bottom and top play an insignificant role in the dynamics of the system. The two lightest quarks up and down are considered to be degenerate $m_u = m_d = m_{u,d}$, as their physical mass values are very similar. The strange quark mass m_s is much larger than these two. However, considering the two light quarks and the heavier strange quark is a good approximation. In principle, the variation of the quark masses leads to different QCD phase diagrams, which provides insight into the physical phase diagram. As in the next section 2.3 the variation of the quark masses is discussed for $\mu=0$, here, only physical quark masses are considered. The QCD phase diagram, reflecting this situation according to [29], is shown in figure 2.1. In the following, the different phases in this phase diagram are explained qualitatively. For a good overview, also the phases at high chemical potential are discussed briefly, although only the $\mu=0$ line is subject of the research of this thesis.

The hadronic phase in the lower left corner for low temperatures and low baryochemical potential is delimited by a first order phase transition line, which ends in the critical endpoint E. The critical endpoint represents a second order phase transition and is in the Ising universality class. From this point to the vertical temperature axis, the transition from the hadronic phase to the quark-gluon-plasma for high temperatures turns into a smooth crossover. This transition at $\mu=0$ and T_c will be subject of the next section 2.3, where the type of the phase transition is investigated depending on the masses of the three lightest quarks $m_{u,d}$ and m_s . Another transition for the hadronic phase is the nuclear liquid-gas phase transition, which is represented in figure 2.1 by the short line emerging from the horizontal axis. On the left of this line, the nucleons exist as single,

unbound nucleons. When undergoing this first order liquid-gas phase transition, the nucleons bind and form a liquid.

At high densities, two color superconducting phases are believed to exist, which will not be discussed here in detail. For more information on the high density phases see [1]. In the two-flavor-superconducting (2SC) phase the two lightest quarks build Cooper pairs, using two of the three colors. In the color-flavor-locked (CFL) phase also the heavier strange quarks form Cooper pairs. Here, the color degrees of freedom are locked to the three flavor degrees of freedom, hence the origin of the name. The CFL phase can again be investigated using first principles, as QCD becomes analytically tractable for very large densities.

Finally, situations in experiments or in nature can be related to the QCD phase diagram, clarifying the importance of understanding the phase structure of QCD. For example, during the evolution of the early universe, the fast expansion cooled the quark gluon plasma. Near the $\mu=0$ axis, the quark matter was undergoing the QCD thermal transition, i.e. a crossover transition to hadronic matter. The cores of neutron stars are presumably located at low temperatures and high densities in the phase diagram. Experimental heavy ion collisions explore the QCD phase diagram for high temperatures and rather small densities. Experiments are performed for example at the Large Hadron Collider (LHC) at CERN and at the Relativistic Heavy Ion Collider (RHIC) in Brookhaven.

The actual focus of this thesis is on the deconfinement transition at $\mu=0$. Lattice QCD calculations for physical quark masses have shown, that the QCD thermal transition is a smooth crossover [2] with a critical temperature in the range of about 150MeV to 170MeV [7]. The resulting critical temperature depends on the choice of the determining observable. In the next section 2.3, only this QCD thermal transition at $\mu=0$ will be subject of the discussion of the Columbia plot.

2.3. The Columbia Plot

When performing finite temperature lattice QCD Monte Carlo simulations at zero chemical potential, parameters to be tuned are the quark masses and the temperature. For the QCD transition at the critical temperature T_c , the type of the transition can be visualized in a two dimensional plot, where the quark masses $m_{u,d}$ and m_s of the three lightest quarks are on the horizontal and vertical axis, respectively. An early version of this so called Columbia plot was already developed by a group at the Columbia University in 1990 [8]. It has to be noted, that the Columbia plot combines the types of the phase transitions connected to the chiral and the center symmetry. For the chiral symmetry, the chiral condensate is the order parameter connected to the chiral transition. For the center symmetry, the Polyakov loop is the order parameter connected to the deconfinement transition.

A qualitative version of the Columbia plot is shown in figure 2.2. The quark mass for the up and down quark is represented by the horizontal axis and the strange quark mass is represented by the vertical axis. Three lines identify the points in the phase diagram for which either one, two or three quarks are degenerate. This follows from the fact, that infinitely heavy quarks decouple from the theory. The $N_f=1$ line marks infinitely heavy up and down quarks on the right vertical axis. Towards infinite strange quark mass, a

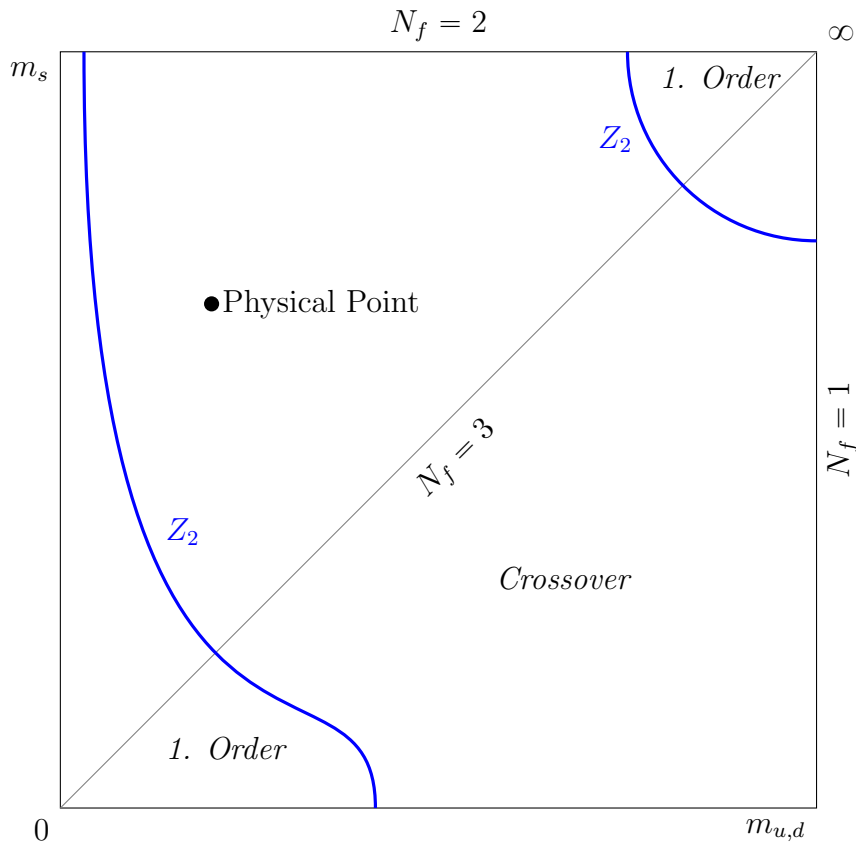


Figure 2.2.: The Columbia plot, showing qualitatively the type of the QCD transition at $\mu=0$ in the plane of the quark masses $m_{u,d}$ and m_s . Areas, where a first order phase transition takes place, are marked by *1. Order*. Areas, marked with *Crossover*, indicate a crossover transition and the blue lines, marked with Z_2 , represent second order phase transitions in the Ising universality class.

two-fold degeneracy of the up and the down quark is represented by the upper horizontal axis. A degeneracy of all three quark masses corresponds to the diagonal line from the lower left corner to the upper right corner. The other points in the plane are different combinations of the quark masses $m_{u,d}$ and m_s , being denoted as $N_f=2+1$. Finally, the physical point marks the approximate location of the real physical quark masses in the Columbia plot.

Now, the conclusion about the type of the thermal QCD transition, following from of the Columbia plot, is discussed. The physical point, corresponding to the transition at $\mu=0$ in the QCD phase diagram in figure 2.1, is clearly located in the crossover region. For small $m_{u,d}$, a first order region is delimited by a Z_2 line. For $N_f=3$, the chirally symmetric phase appears, when the masses are zero. This first order phase transition is related to the spontaneous symmetry breaking of the chiral symmetry. When increasing the masses, the chiral symmetry is broken explicitly, weakening the first order phase transition for sufficiently small masses. At some point, the phase transition turns into a Z_2 second order phase transition of the Ising universality class. Moving further on the $N_f=3$ line, the large crossover region is entered, for which no non-analyticities occur

in the thermodynamic observables. The Z_2 second order phase transition separates the first order region from the crossover region, at least for small quark masses $m_{u,d}$ and m_s . For larger m_s , the situation is not quite clear yet, as the simulation of smaller quark masses gets computationally more costly. The scenario of the first order region, ending at a finite value of m_s and $m_{u,d}$, is possible. This leads to different possible universality classes for the phase transition at small $m_{u,d}$. As this thesis considers the heavy mass critical deconfinement line in the right upper corner, the details of this discussion are omitted, but they can be found in chapter §2.2 of [34], where different scenarios for the small $m_{u,d}$ region are shown. Figure 2.2 shows one particular scenario, to give an impression of the complete Columbia plot. The heavy masses region in the right upper corner is better understood, because simulations are computationally less costly. This first order phase transition corresponds to the quenched approximation of QCD with quarks being infinitely heavy. As already discussed in section 1.6, pure gauge theory is invariant under center transformations. In this case the Polyakov loop is an exact order parameter. Finite but large masses can be treated as an external field $1/m$ breaking the center symmetry explicitly, which leads to a weakening of the first order phase transition. Hence, the Polyakov loop is not an exact order parameter for the deconfinement transition anymore but an approximate one. The first order region is again enclosed by a Z_2 line, where the explicit center symmetry breaking has weakened the first order phase transition sufficiently, leading to a vanishing latent heat and a second order phase transition. The localization of the point, where the Z_2 line touches the $N_f=2$ line, is the main goal of this thesis.

One reason to show the Columbia plot qualitatively, is the lack of sufficient continuum extrapolations of the critical masses, for which a second order phase transition takes place. In principle, the results from various simulations can be compared by calculating the corresponding pseudo scalar meson mass. A shift of the Z_2 lines has been observed for decreasing the lattice spacing. This behavior is visualized in a study about simulations with $N_f=2$ Wilson fermions [13]. It shows the shift of the Z_2 line for the deconfinement phase transition in the heavy quark mass region to smaller mass values, as the lattice gets finer. The goal for this thesis is also the localization of the same critical Z_2 point, with the difference of using the staggered fermion discretization. The shift of the Z_2 critical point towards finer lattices, however, cannot be evaluated, as only one temporal lattice extent $N_\tau=8$ is simulated for this thesis.

3. Numerical Aspects of Phase Transitions in LQCD

This chapter first discusses the numerical methods to investigate phase transitions and numerical aspects for LQCD calculations in general. Thereafter, a brief section gives an overview over the used tools, which implement the beforehand discussed numerical methods. Section 3.3 about the Python Fitting GUI plays a special role, as the implementation of this tool was a major task during the work for this thesis. Thus, it receives a more detailed reflection in a separate section.

3.1. Numerical Analysis of Phase Transitions

As the analysis of phase transitions with numerical calculations on a finite lattice requires many different methods, the most important ones are discussed in this section. The methods approach the problem of calculating an expectation value of an observable in a statistical system by numerical simulations. A method to estimate the error on the expectation value of an observable has to be found. Furthermore, the particular observables, which help to locate phase transitions and determine their types, are considered. This approach uses the two standardized moments skewness and kurtosis, being discussed in section 3.1.4. In the end, a method to obtain the Z_2 critical mass is explained, which is based on fitting a finite-size scaling formula of the kurtosis of the Polyakov loop to the numerically obtained data at the critical β s. Hence, different ansätze for the kurtosis fit formula are presented, also extending beyond the usual Polynomial fit ansatz.

3.1.1. Monte Carlo Importance Sampling

As already stated in section 1.1, in general, the QCD path integrals are not analytically solvable. Even if the space-time is discretized to a finite lattice, the analytical calculation of the path integrals cannot be performed on a reasonably large lattice. This is the reason for using Monte Carlo simulations to approximate the path integrals. For gauge observables they look like

$$\langle O \rangle = \frac{1}{Z} \int \mathcal{D}[\psi, \bar{\psi}] \mathcal{D}[U] e^{-S_{LQCD}[\psi, \bar{\psi}, U]} O[U], \quad (3.1)$$

where the partition function is given by

$$Z = \int \mathcal{D}[\psi, \bar{\psi}] \mathcal{D}[U] e^{-S_{LQCD}[\psi, \bar{\psi}, U]}. \quad (3.2)$$

The action S_{LQCD} , depending on the fermion fields ψ and $\bar{\psi}$ and the gauge links U , in general, is a discretization of the continuum QCD action. In formulas (3.1) and (3.2) the

fermion fields $\psi, \bar{\psi}$ can be integrated out analytically, arriving at a fermion determinant $\det[D[U]]$, depending on the gauge links. The path integral (3.1) can therefore be written as

$$\langle O \rangle = \frac{1}{Z} \int \mathcal{D}[U] e^{-S_G[U]} \det(D[U]) O[U] = \frac{1}{Z} \int \mathcal{D}[U] e^{-S_{eff}[U]} O[U], \quad (3.3)$$

where the property of the fermion determinant, being real and non negative, is used to introduce the substitution $S_{eff}[U] = S_G[U] + \ln(\det(D[U]))$. The same substitutions are applied to the partition function in formula (3.2). The idea of the Monte Carlo importance sampling method is approximating such integrals by a sum over configurations $\{U\}$, which are randomly sampled with a probability weight $e^{-S_{eff}[U]} = e^{-S[U]}$. One configuration $\{U\}$ is the set of all gauge links on the lattice. The sum, approximating the path integral (3.1), can be denoted as

$$\langle O \rangle \approx \frac{1}{N} \sum_{\substack{\{U\}_n \\ \text{sampled} \\ \propto e^{-S[U_n]}}} O[U_n]. \quad (3.4)$$

It has to be evaluated on a sufficiently large number of configurations N to give an adequate result. A detailed introduction to Monte Carlo methods can be found in chapter 4 of *Quantum Chromodynamics on the Lattice* [17], whereas here, only the general concepts are presented.

The challenge is to efficiently find new configurations $\{U\}_n$, which are sampled according to the probability distribution density

$$dP(U) = \frac{e^{-S[U]} \mathcal{D}[U]}{\int \mathcal{D}[U] e^{-S[U]}}. \quad (3.5)$$

The concept of the Markov Chain helps to tackle this challenge. A Markov Chain is a set of ordered configurations, where the n th configuration is generated, depending on the $(n-1)$ th configuration. Starting with an initial configuration after a thermalization process, the generation of new Markov Chain elements is designed, such that overall, the new configuration is drawn randomly with a probability proportional to the Boltzmann weight $e^{-S[U]}$. This requires an efficient pseudo random number generator, because real random numbers are not available on conventional computers. Additionally, the large amount of pseudo random numbers required must not lead to recurring patterns and so a distortion of the statistics produced by the Markov Chain.

There are many ways of generating new Markov Chain elements, in this case new gauge configurations, but they depend on the applied action. For this thesis, always the rational hybrid Monte Carlo (RHMC) algorithm [10] was used. It is required for the staggered fermion action, which relies on the rooting trick explained in section 1.2. The details of the RHMC algorithm are once again omitted and the focus is on the rough idea. The algorithm relies on evolving the configurations by integrating the classical Hamiltonian equations of motion in a discretized computer time. This involves the calculation of a force term, consisting among others of a term with the inverse Dirac operator. The *rational* property of the RHMC algorithm refers to the approximation of the inverse Dirac operator. In this case, it is a *rational* function. The algorithm is nevertheless exact, because in the end, a Metropolis accept-reject-step accounts for the approximations in

the integration of the Hamiltonian equations and for the approximation of the inverse Dirac operator. Referring to the classical Hamiltonian equations of motion, one update of a configuration is also called trajectory.

The gauge configurations are produced with the RHMC algorithm, on which the gauge observables are evaluated. An important issue is the correlation between the trajectories, a simple consequence of the fact, that in a Markov chain, a configuration always depends on the previous one. When calculating the mean and the error of an observable, the correlation of the trajectories has to be taken into account. This problem is subject of the next section 3.1.2.

3.1.2. Analyzing an Observable

For each trajectory in the Markov Chain, several observables can be measured on the gauge configurations. Here, one example observable X is considered, for which the measurements $\{x_i\}$, $i \in [1, \dots, N]$ have been collected. It is not as easy to evaluate the equation (3.4) as it seems to be, because the autocorrelation of the measurements $\{x_i\}$ has to be considered. Additionally, observables depending on the measurements (i.e. $O[\{x_i\}]$) are calculated and an error for the mean value of O has to be specified. The following describes the general analysis of an observable, which was performed throughout this thesis.

On a given set of N measurements of X , leading to the data set $\{x_i\}$, the integrated autocorrelation time τ_{int} can be calculated for any observable O , depending on this data. The autocorrelation time is a measure for the number of trajectories, over which they are typically correlated. For this thesis, the method to calculate an effective τ_{int} proposed by Ulli Wolff [39] was used. Having obtained τ_{int} , a binning procedure can be performed, implying a division of the measurements into equally large parts (bins) of the size of (at least) two times the autocorrelation time. The mean value of the measurement X is calculated for these bins, creating a new data set of $K = \frac{N}{\tau_{int}}$ data points, being uncorrelated with respect to the observable O . Ideally, N is a multiple of $2 \cdot \tau_{int}$, otherwise the remaining data is discarded.

The binned data set of K data points $\{x'_i\}$ can now be used to calculate the mean and the error of the mean value of the observable. Several methods exist for that, but here, only the jackknife method is discussed, because it is the only relevant one for this thesis. Given the data set of K uncorrelated measurements, the jackknife method first creates K new subsets of the data $\{x'_i\}$, $i \in [1, \dots, K]$ by removing the n th entry from the original data set to obtain the n th jackknife sample $\{x'_1, \dots, x'_{n-1}, x'_{n+1}, \dots, x'_K\}$. The observable O is evaluated on these jackknife samples, obtaining K jackknife replicates O_n^J , $n \in [1, \dots, K]$.

$$\hat{O} = \frac{1}{K} \sum_{i=1}^K O_n^J \quad (3.6)$$

is quoted as a biased estimator for the mean value of O . The estimator of the variance of the mean value of O can be determined as

$$\sigma_{\hat{O}}^2 = \frac{K-1}{K} \sum_{n=1}^K \left(O_n^J - \hat{O} \right)^2. \quad (3.7)$$

The final result is quoted as $\hat{O} \pm \sigma_{\hat{O}}$.

The mean of X is considered as a trivial observable

$$\hat{X} = \frac{1}{K} \sum_{i=1}^K \hat{X}_n^J, \quad (3.8)$$

where the \hat{X}_n^J are evaluated according to

$$\hat{X}_n^J = \frac{1}{K-1} \sum_{i=1, i \neq m}^K x_i. \quad (3.9)$$

The result for \hat{X} is the same for the jackknife method and the conventional method of calculating a mean, but only for this special case. Higher moments, being discussed in section 3.1.4, evaluate differently and also composed quantities have to be considered, specifically the standardized moments

$$B_n = \frac{\mu_n}{\mu_2^{n/2}}, \quad (3.10)$$

where the μ_n are the central moments $\mu_n = \sum_i (x_i - \hat{X})^n$. As \hat{X} can be calculated without any jackknife method, the standardized moments $n > 2$ are composed of two quantities, i.e. the numerator and the denominator in a fraction, for which the jackknife replicates have to be evaluated separately. Clearly, the bin sizes in the beforehand binning procedure have to coincide and therefore, always the larger bin size, related to the autocorrelation time of the quantities, is chosen to be on the safe side. Subsequently, the jackknife method is applied for the two quantities. The observable $O = \frac{x}{y}$ is assumed, being composed of the quantities x and y . These quantities can be analyzed with the jackknife method, leading to jackknife replicates x_n^J and y_n^J , being evaluated on the same jackknife sample for each n . The jackknife replicates x_n^J and y_n^J combine to the jackknife replicate

$$O_n^J = \frac{x_n^J}{y_n^J}. \quad (3.11)$$

Subsequently, the known formulas (3.6) and (3.7) can be applied.

In the end, there is a clear procedure of the calculation of the jackknife estimators of the mean and the variance of any observable depending on the correlated measurements of the Markov Chain. In this way, the order parameter of a phase transition is analyzed at particular points in the parameter space consisting of spatial extent N_s , the mass m and the inverse gauge coupling β . Due to the high computational cost, the discretization of the parameter space is coarse and an interpolating method is required, to gain insight in for example the more precise variation of the order parameter, depending on parameters like β . One possible interpolating method is discussed in the next section 3.1.3.

3.1.3. Reweighting

The reweighting method, also formally known as the multiple histogram method, combines several simulations at different values in the parameter space to estimate the observable at non-simulated values of the parameter. The condition for this parameter of the simulation is the linear appearance in the action. This interpolating method was first

introduced in 1989 by Ferrenberg and Swendsen [16]. This section does not focus on the derivation of the formulas or the implementation details, which can be found in chapter 8 of Newman and Barkema's *Monte Carlo Methods in Statistical Physics* [24]. Instead, the rough idea behind the multiple histogram method is outlined and the relevant formulas are presented. In the end, it is illustrated, how this method helps to locate the critical β and to find an indicator of the type of the phase transition.

The discussion will be restricted to reweighting in the inverse gauge coupling β , although it is possible to generalize it to other parameters. The parameter β enters the probability weight as $\exp(-S_G) = \exp(-\beta E)$, where S_G is the gauge action and $E = \frac{S_G}{\beta}$ is the conjugated quantity to β . The idea of this method descends from the single histogram method [15], offering the possibility to extrapolate an observable to values of β in the vicinity of one simulated point. These estimates of several values at β s in between the simulated β s can be combined, giving a weight according to the accuracy of the extrapolated value of the observable. The way, how these estimates from different β s are combined, depends on the density of states, which describes the number of states of the systems with a certain value of one observable. The important property of the density of states is the independence of β , such that simulations at different β s give estimates for the same function of the density of states. Combining these estimates with a weight according to their accuracy, leads to a good estimate of the density of states over the complete range of the conjugated quantity E , as long as the gauge action histograms of the different simulated β values overlap sufficiently. Having outlined the rough idea behind the multiple histogram method, the formula of a reweighted observable Q at an arbitrary β is shown. It is assumed, that several simulations at different β_j have been performed and for each β the observable Q is measured n_j times. Hence, the reweighted quantity Q is

$$\langle Q(\beta) \rangle = \frac{1}{Z(\beta)} \sum_{i,s} \frac{Q_s(\beta_i)}{\sum_j n_j Z_j^{-1} e^{(\beta-\beta_j)E_s(\beta_i)}}. \quad (3.12)$$

The partition function $Z(\beta)$ in this formula follows from

$$Z(\beta) = \sum_{i,s} \frac{1}{\sum_j n_j Z_j^{-1} e^{(\beta-\beta_j)E_s(\beta_i)}}, \quad (3.13)$$

where $Z_j = Z(\beta_j)$. Due to the dependence of $Z(\beta)$ on the Z_j in equation (3.13), it is a recursive function. This can be solved numerically by giving any starting value to the Z_j and solving this equation to obtain new values of Z_j with a higher accuracy. Iterating this process leads to an approximation of Z_j with an acceptable accuracy at some point. The indices i and j are referencing the simulations at different β s. The index s references the trajectories in the i th simulation, running from 1 to n_i .

To obtain an error on the reweighted quantity, the already discussed jackknife method from section 3.1.2 is used. The idea is, to reweight the observable Q several times at a specific β , every time omitting a different data point (with respect to the binned, uncorrelated data), thus obtaining the jackknife estimators $Q_n^J(\beta)$. The mean and the variance can be calculated with these jackknife estimators, as it was discussed before.

The multiple histogram method for lattice QCD observables is implemented in PLASMA, as explained in section 3.2.3. In the following, it will be illustrated briefly, how the multiple histogram technique helps to locate a phase transition by determining a critical β . As will be explained in the next section 3.1.4, the skewness of the order

parameter becomes 0 at the critical β . The reweighting of the skewness of the order parameter helps to locate this critical β , where the absolute value of the reweighted skewness is closest to zero. As will be clear also in the next section 3.1.4, the kurtosis of the critical β gives information about the type of the phase transition. Thus, by reweighting the kurtosis, the value of the kurtosis is determined at the critical β . This value can be used to examine the type of the phase transition. A figure, illustrating the steps to finding the value of the kurtosis at the critical β , is shown in the last chapter 4, when discussing the obtained kurtosis data. Figure 4.1 shows the results of the analysis and the reweighting of the skewness and the kurtosis for a particular mass $am=0.55$ and volume $N_s=56$.

3.1.4. Skewness and Kurtosis

The skewness and kurtosis of a random variable say something about the shape of the probability distribution of the random variable. This will help to identify the critical point of the phase transition and it will also be helpful to determine the type of the phase transition. The meaning of the skewness and the kurtosis values for the shape of the probability distribution will be explained after the introduction of the moments, central moments and standardized moments, of which the skewness and the kurtosis are two special cases.

For a random variable $X \in \mathbb{R}$ with a given probability density function $f(X)$, the n th moment is defined as

$$m_n = \int_{-\infty}^{\infty} dX f(X) \cdot X^n. \quad (3.14)$$

Additionally, the n th central moment is defined as

$$\mu_n = \int_{-\infty}^{\infty} dX f(X) \cdot (X - m_1)^n, \quad (3.15)$$

where m_1 is the first moment, also called the mean. The second central moment μ_2 is called the variance. It is useful to define a moment generating function, which generates the moments by taking derivatives with respect to a source t and setting it to zero afterwards. The definition for the moment generating function is

$$M_X(t) = \int_{-\infty}^{\infty} dX f(X) \cdot e^{tX} \quad (3.16)$$

and hence, the n th moment is given by

$$m_n = \left. \frac{d^n}{dt^n} M_X(t) \right|_{t=0} = M_X^{(n)}(0). \quad (3.17)$$

Having defined the moment generating function, also a cumulant generating function can be defined, which generates the cumulants κ_n analogously to the moments. The cumulant generating function

$$K_X(t) = \ln(M_X(t)) \quad (3.18)$$

generates the cumulants

$$\kappa_n = \left. \frac{d^n}{dt^n} K_X(t) \right|_{t=0} = K_X^{(n)}(0). \quad (3.19)$$

General relations can be derived between the cumulants and the central moments by first calculating both the cumulants and the central moments as functions of the moments. The results are only shown for selected relations, which are required in the next subsection 3.1.5 for the finite size scaling of the kurtosis. The first relation of interest considers μ_2 and κ_2 leading to

$$\mu_2 = \kappa_2 = m_2 - m_1^2, \quad (3.20)$$

having used formulas (3.15) and (3.19). The same formulas can be applied to κ_4 and μ_4 :

$$\mu_4 = m_4 - 4m_3m_1 + 6m_2m_1^2 - 3m_1^4 \quad (3.21)$$

$$\kappa_4 = m_4 - 4m_3m_1 + 12m_2m_1^2 - 6m_1^4 - 3m_2^2 \quad (3.22)$$

Comparing the coefficients of the terms, the result is

$$\mu_4 = \kappa_4 + 3(m_1^4 - 2m_2m_1^2 + m_2^2) \quad (3.23)$$

and by also inserting the result from equation (3.20), the final relation

$$\mu_4 = \kappa_4 + 3\kappa_2^2 \quad (3.24)$$

is obtained

Having introduced these definitions and the relevant relations, the standardized moments are discussed, including the skewness and the kurtosis. They are defined by a fraction of the central moments

$$B_n = \frac{\mu_n}{(\mu_2)^{n/2}}. \quad (3.25)$$

The first standardized moment B_1 is zero, since the first central moment is also zero. The second standardized moment is 1, as the numerator and the denominator both are the variance.

The first nontrivial standardized moment is the third one, called the skewness. It is a measure for the asymmetry of the distribution of the random variable. It assumes negative values, if the bigger part of the distribution is concentrated on the right side. It becomes zero, if the parts of the distribution are distributed evenly around the center and positive values are obtained, if the main part of the distribution concentrates on the left side.

The highest standardized moment, being discussed here, is the kurtosis B_4 . As the skewness, it also says something about the shape of the distribution of a random variable. For a long time, the kurtosis was related to the peakedness of the distribution, which in fact is a misinterpretation, as it actually gives very little in evidence about the peak or the center of a distribution [37]. A better meaningful interpretation for the kurtosis is the tailedness. Consequently, a distribution with a large kurtosis generates more outliers with respect to the center of the distribution than distributions with a smaller kurtosis. The shape of the tails of the distribution is much more reflected in the kurtosis than the shape of the center.

The question, how the kurtosis and the skewness can help to locate and identify the phase transition, is approached in the following. For the localization of the phase transition, the temperature is scanned, which is equivalent to a scan in β for LQCD. The critical temperature is reached, when all phases are equally probable for a first order transition or when the critical phase is present for the second order phase transition.

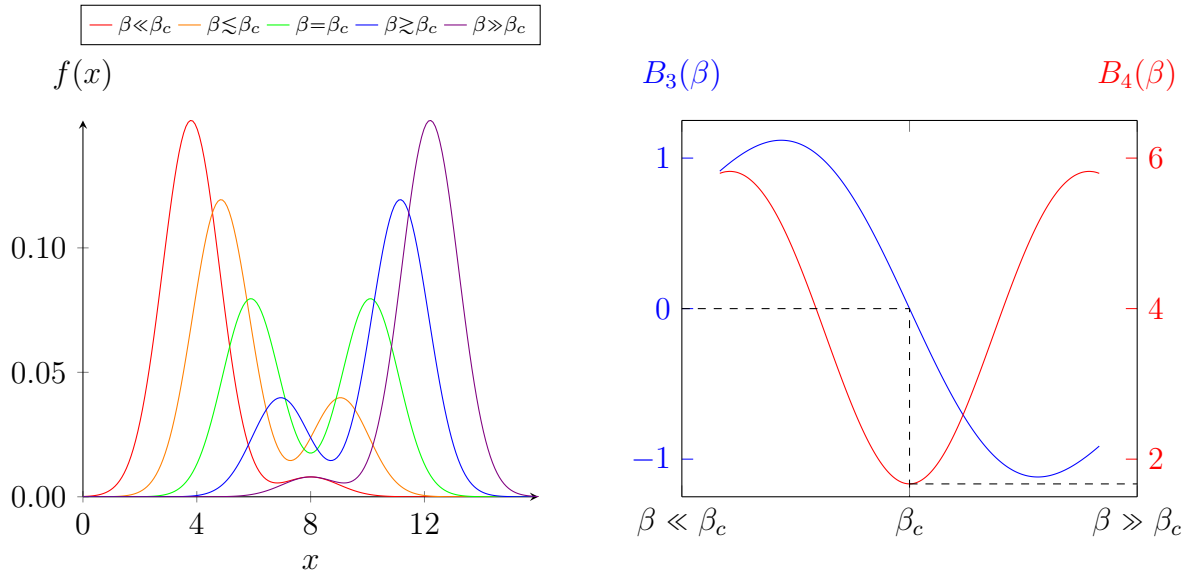


Figure 3.1.: **Left:** Modeled probability distributions of the order parameter x for 5 β -values around β_c . At β_c , two separate coexisting phases indicate a first order phase transition. The probability distributions are two additive Gaussian distributions with different relative weight for each β .

Right: A modeled course of the skewness $B_3(\beta)$ and the kurtosis $B_4(\beta)$, qualitatively corresponding to the distributions on the right and the indication of the zero crossing of the skewness, determining β_c and the localization of $B_4(\beta_c)$. (Plots inspired by [11].)

The order parameter for different temperatures is calculated in finite systems, implying that a true phase transition cannot take place (referring to section 2.1) and the order parameter is distributed continuously. Several modeled distributions of the order parameter for β values around β_c are shown in figure 3.1 on the left. The distribution of the order parameter becomes symmetric, if the critical temperature (critical β) is reached, because at that point, the two phases of a first order phase transition are equally favorable for the system. As the skewness measures the asymmetry of the distribution, a temperature is sought, at which the skewness becomes zero. For numerical simulations, this can be done by applying the reweighting technique introduced in section 3.1.3, avoiding a very fine and computationally expensive scan in the temperature. In figure 3.1 on the right, the qualitative courses of the skewness and the kurtosis corresponding to the distributions on the left are plotted as a function of β . The zero crossing of the skewness at the critical β is indicated. This helps to determine the critical β and the kurtosis at the critical β . The kurtosis assumes a minimum at β_c , but when relying on reweighted data, the determination of β_c from the zero crossing of the skewness is more accurate.

As the critical temperature is found by searching for a zero-transition of the skewness, now the type of the phase transition can be determined. The kurtosis at the critical temperature assumes distinct values for different types of phase transitions in the infinite volume limit. In table 3.1 the kurtosis values of the relevant transitions are shown. The values for the first order transition and the crossover transition can be computed

Transition Type	1. Order	Z_2 (Ising 3D)	Crossover
$B_4(T_c)$	1	1.604(1)	3
Notation	$B_4(\infty, 1.O)$	$B_4(\infty, Z_2)$	$B_4(\infty, CO)$

Table 3.1.: The values of the kurtosis at the critical temperature for different types of transitions (Z_2 value from [5]). The notation, which is used in the following, is shown at the bottom. ∞ refers to the infinite volume limit.

analytically, using Gaussian distributions. For the Crossover, it is just one Gaussian distribution and for the first order transition, two of them are summed up. They have to be sufficiently far apart, implying a much larger difference of the means $\Delta\mu$ than the individual standard deviations σ : $\Delta\mu \gg \sigma$. The value of the kurtosis at a Z_2 second order phase transition for the Ising 3D model can only be obtained numerically, it is thus not exact and the statistical error is appended in brackets. The value in table 3.1 is obtained by Monte Carlo simulations of the 3D Ising model according to [5].

The goal to find the critical mass, where a second order phase transition takes place, can in principle be achieved by considering the kurtosis values of the order parameter at the critical temperature and in the infinite volume limit. Since such numerical simulations always use a finite lattice, it is necessary to perform a finite size scaling analysis to relate the results obtained in a finite volume to values in the thermodynamic limit. This is done in the next section 3.1.5 for the kurtosis of the Polyakov loop, forming the basis for finding suitable kurtosis fit formulas to determine the critical mass in section 3.1.6.

3.1.5. Finite Size Scaling of the Kurtosis

In the previous subsection, the kurtosis was introduced and its expression as fractions of the central moments was shown. Inserting the relations of the cumulants (3.20) and (3.24), leads to

$$B_4 = \frac{\mu_4}{\mu_2^2} = \frac{\kappa_4}{\kappa_2^2} + 3. \quad (3.26)$$

These cumulants can be written as derivatives of the free energy, allowing a derivation of a scaling law for the kurtosis from the scaling laws of the free energy density.

In the last subsection, the generation of cumulants by the cumulant-generating function $K_X(t)$ was discussed. To obtain a cumulant-generating function, the moment-generating function is considered, which is the partition function $Z = \text{Tr}\left(e^{-\tilde{\beta}\hat{H}(\alpha_i)}\right)$. The Hamiltonian \hat{H} depends on the coupling constants α_i . For preventing of mixing up the inverse gauge coupling β and the inverse temperature, $\tilde{\beta}$ is used as the inverse temperature. The analogy with equation (3.16) shows, that the partition function can indeed be used as the moment generating function, which has to be differentiated with respect to $\tilde{\beta}$ or the α_i .

The cumulant-generating function is the logarithm of the moment generating function according to (3.18), such that $\ln(Z) = -\tilde{\beta}F$ represents the cumulant-generating function in statistical physics, where F is the free energy. As an abbreviation, the reduced free energy is introduced as

$$\tilde{F} = -\tilde{\beta}F, \quad (3.27)$$

which will be used as the cumulant-generating function from now on.

From section 2.1.2, the finite size scaling of the reduced free energy is

$$\tilde{F}(t, h, N_s^{-1}) = \tilde{F}(tN_s^{y_t}, hN_s^{y_h}, 1), \quad (3.28)$$

where ℓ is chosen arbitrarily and is set to $\ell = N_s$. N_s is the number of spatial lattice points. The finite size scaling analysis of the kurtosis is derived for the Ising model with its parameters h and t , which subsequently can be transferred to the lattice QCD model in the heavy mass regime with its parameters β and $\frac{1}{m}$. This is possible, because universality guarantees the same scaling laws for both models in the vicinity of a critical Z_2 point. $\frac{1}{m}$ is the parameter of heavy mass lattice QCD, since it is the center symmetry breaking parameter. If $\frac{1}{m} = 0$, the center symmetry is restored for the quenched approximation. In this section 3.1, m represents the mass in lattice units. Additionally, general simplified relations between the coupling parameters of each model have to be assumed. Linear mixing of the parameters in the vicinity of the critical point [21] is assumed

$$t = a(\beta - \beta_c) + b \left(\frac{1}{m} - \frac{1}{m_c} \right) \quad (3.29)$$

$$h = c \left(\frac{1}{m} - \frac{1}{m_c} \right) + d(\beta - \beta_c), \quad (3.30)$$

where a, b, c, d are constants, later being absorbed into fitting parameters. Recalling the definitions of h and t from section 2.1.2, they are the reduced temperature and the reduced magnetic field, respectively. First, the finite size formula for the kurtosis has to be elaborated with these Ising model parameters.

The steps, to analyze the finite size scaling of the kurtosis shown here, follow the presentation in [35]. First, a purely magnetization like observable O is assumed, for which the kurtosis is calculated. This leads to the representation

$$O = c_M \cdot M \rightarrow c_M \frac{\partial}{\partial h}. \quad (3.31)$$

To simplify the following derivation of the finite size scaling of the kurtosis, the abbreviation

$$\frac{\partial^n}{\partial h^n} \tilde{F}(t, h) = \tilde{F}^{(n)}(t, h) \quad (3.32)$$

is used. Following equation (3.26), the fourth and the second cumulant are calculated according to

$$\kappa_4 = \frac{\partial^4}{\partial h^4} \tilde{F}(tN_s^{y_t}, hN_s^{y_h}, 1), \quad (3.33)$$

$$\kappa_2 = \frac{\partial^2}{\partial h^2} \tilde{F}(tN_s^{y_t}, hN_s^{y_h}, 1). \quad (3.34)$$

Hence, the kurtosis is

$$B_4 = \frac{N_s^{4y_h} \tilde{F}^{(4)}(tN_s^{y_t}, hN_s^{y_h}, 1)}{N_s^{4y_h} \left(\tilde{F}^{(2)}(tN_s^{y_t}, hN_s^{y_h}, 1) \right)^2} + 3 = \frac{\tilde{F}^{(4)}(tN_s^{y_t}, 0, 1)}{\left(\tilde{F}^{(2)}(tN_s^{y_t}, 0, 1) \right)^2} + 3, \quad (3.35)$$

where h is set to zero. The reason to set h to zero becomes clear, when considering the phase diagrams in the coupling parameter space of the Ising model and lattice QCD,

each in the vicinity of the critical point. The two phase diagrams are shown in figure 3.2. Below a critical temperature, the Ising model exhibits a first order phase transition (PT) at $h = 0$, where the spontaneous magnetization jumps between $-|M(0)|$ and $|M(0)|$, tuning h across $h = 0$. At the critical temperature, this transition becomes continuous, resulting in the Z_2 critical end point. Lattice QCD exhibits a first order phase transition in the quenched approximation, where the mass is infinitely large, thus $\frac{1}{m} = 0$. The 1. order phase transition weakens, when the center symmetry breaking parameter $\frac{1}{m}$ is increased, leading to a second order critical end point. The critical values of β , where the first order phase transition takes place, decrease as the mass is decreased.

As explained in the previous section 3.1.4, the strategy is scanning in β around the critical β at a fixed mass value, to find the critical β and determine the value of the kurtosis at that point. This is applied for the first order line and its symmetrical extension into the crossover region. The kurtosis values at this critical line can be mapped onto the phase diagram of the Ising model, where the same line is located at $h = 0$. Finding the kurtosis values at the critical β values allows to set $h = 0$, as the correspondence of the two phase diagrams in the vicinity of the critical Z_2 point has shown.

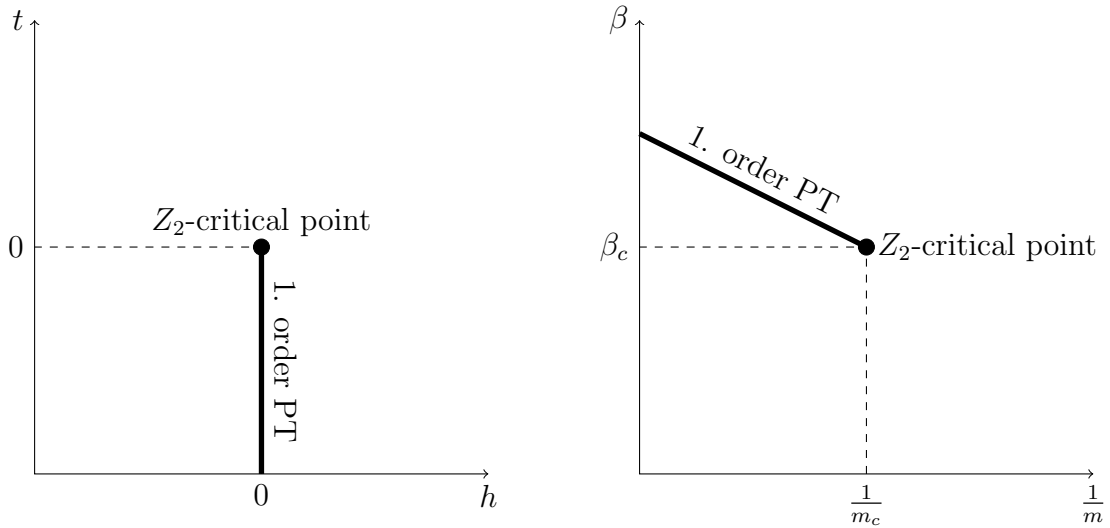


Figure 3.2.: Comparison of the phase diagrams in coupling parameter space of the Ising model and the lattice QCD model in the heavy mass regime. t is the reduced temperature and h the reduced external magnetic field. For the lattice QCD phase diagram, β is the inverse gauge coupling and $\frac{1}{m}$ is the inverse mass of the two degenerate fermions.

The right hand side of equation (3.35) can be expanded as a series around $t = 0$. The expression for the Taylor series expansion is

$$B_4 = A + B \cdot t N_s^{\frac{1}{\nu}} + \mathcal{O}\left(t^2 N_s^{\frac{2}{\nu}}\right), \quad (3.36)$$

where $\frac{1}{\nu} = y_t$ from section 2.1.2 was used. A and B are constants to be determined by universality or a fit.

The observable in equation (3.31), for which the kurtosis is calculated, is assumed to be purely magnetization like. The property of the order parameter Polyakov loop, not being

exact but approximate, leads to a mixture of an energy like part and a magnetization like part in the observable:

$$O = c_E \cdot E + c_M \cdot M \rightarrow c_E \cdot \frac{\partial}{\partial \tilde{\beta}} + c_M \cdot \frac{\partial}{\partial h}, \quad (3.37)$$

where c_E and c_M are the constants, belonging to the energy part and the magnetic part, respectively. In this case, $\tilde{\beta}$ is the inverse temperature, being related to the reduced temperature t via $\tilde{\beta} = (T_c(t+1))^{-1}$. The derivative with respect to $\tilde{\beta}$ leads to an additional correction term for the formula, already presented in equation (3.36). The precise derivation is given in appendix A and the result is

$$B_4 = \left(A + B \cdot t N_s^{\frac{1}{\nu}} + \mathcal{O}\left(t^2 N_s^{\frac{2}{\nu}}\right) \right) \cdot \left(1 + C \cdot N_s^{y_t - y_h} + \mathcal{O}\left(N_s^{2(y_t - y_h)}\right) \right), \quad (3.38)$$

where C is again a constant to be obtained as a fit parameter. One last step is relating the reduced temperature to the coupling parameters of lattice QCD. The already introduced linear mixing of the parameters is used

$$t = a(\beta - \beta_c) + b \left(\frac{1}{m} - \frac{1}{m_c} \right) \quad (3.39)$$

and in the vicinity of the critical point the terms $\beta - \beta_c$ and $\frac{1}{m} - \frac{1}{m_c}$ are assumed to be proportional, leading to

$$\beta - \beta_c = d \left(\frac{1}{m} - \frac{1}{m_c} \right), \quad (3.40)$$

with d being a constant. Inserting this into equation (3.39) yields

$$t = D \left(\frac{1}{m} - \frac{1}{m_c} \right), \quad (3.41)$$

where D is again another constant. Equation (3.41) has to be inserted into equation (3.38), yielding a formula, which expresses the finite size scaling of the kurtosis of the order parameter at the heavy Z_2 point:

$$B_4 = \left(A + B \left(\frac{1}{m} - \frac{1}{m_c} \right) N_s^{\frac{1}{\nu}} + \mathcal{O}\left(\left(\frac{1}{m} - \frac{1}{m_c} \right)^2 N_s^{\frac{2}{\nu}} \right) \right) \left(1 + C N_s^{y_t - y_h} + \mathcal{O}\left(N_s^{2(y_t - y_h)} \right) \right) \quad (3.42)$$

It is the basic formula for fitting the numerically obtained kurtosis data. In the next section 3.1.6, the development of possible fit ansätze from formula (3.42) is discussed.

3.1.6. Fitting to the Kurtosis

The last step of determining the value of the critical mass in lattice units is fitting the kurtosis data obtained from the simulations to the finite size scaling formula, which was derived in the last section 3.1.5. This section discusses several possible fit ansätze. It is important to consider the constraints, entering the fit ansätze, and to reduce the number

of degrees of freedom of the fit function. Beforehand, some important general aspects of fitting, including terminology, have to be introduced. Also, the evaluation of the quality of a fit is discussed. This will help to choose the best ones from several possible fits, which differ in the fit ansatz and the selection of data points.

Some important terminology is introduced, concerning the procedure of fitting data to a model function. The fitting data consists of M data points of the form (x_i, y_i) , $i = 1, \dots, M$, where in principle, the x_i and y_i can be vector like. This data set shall be modeled by a function $f(x)$, depending on N fit parameters a_α , $\alpha = 1, \dots, N$. Consequently, the modeled points $(x_i, f(x_i))$ are the counterparts to the data points (x_i, y_i) . By tuning the fit parameters to specific values minimizing the χ^2 , it is ensured, that these sets are as close as possible. For the definition of the χ^2 , note that usually, the data points come with error bars σ_i on the y_i -values. The χ^2 is given as

$$\chi^2 = \sum_{i=1}^M \left(\frac{y_i - f(x_i)}{\sigma_i} \right)^2. \quad (3.43)$$

Another important property of a fit is the number of degrees of freedom, depending on the number of data points M and the number of fit parameters N . It is defined as

$$N_{DOF} = M - N. \quad (3.44)$$

For the determination of the error of the fit parameters, N_{DOF} has to be at least 2. Their calculation depends on the determination of the covariance matrix U , which is an $N \times N$ -matrix and, roughly speaking, a generalization of the variance for N dimensions. Usually, the covariance matrix is returned by the fit algorithm as well as the results for the fit parameters. The variance of the parameters a_α is on the diagonal of U , thus $\sigma_\alpha^2 = U_{\alpha\alpha}$ and the result for the fit parameter is quoted as $a_\alpha \pm \sigma_\alpha$.

The demand for errors of the fit parameters, being as small as possible, already serves as one criterion to evaluate a fit. However, there are two more quantities to evaluate the quality of a fit. One is the χ^2 per number of degrees of freedom, which will be denoted as $\chi_{ndf}^2 = \frac{\chi^2}{N_{DOF}}$. For a good fit, χ_{ndf}^2 assumes values near 1, resulting from the χ^2 distributions for sufficiently large numbers of degrees of freedom. In this case, the distribution approaches a normal distribution with a central value at N_{DOF} . Considering equation (3.43), values of χ_{ndf}^2 larger than 1 would mean a larger average deviation $y_i - f(x_i)$ than the average error on the data points σ_i . This implies, that the fit function does not hit the data points well in the interval of one standard deviation, thus indicating a bad fit in the sense, that it does not model the data points well. The other possibility χ_{ndf}^2 , being smaller than 1, implies, that the average deviation of $y_i - f(x_i)$ is smaller than the average of σ_i . Consequently, the fit function models the data points more precisely than it should be possible due to the fluctuations of the data points y_i , being expressed in σ_i . This can indicate an overfitting of the fit function, implying a bad quality of the fit, which can be explained by considering different samples of the data points generated by the same probability distribution. The fit would only model the sample of data points accurately, on which it was performed, but not the other samples. Thus, for a good fit, a χ_{ndf}^2 as close as possible to 1 is demanded.

Another quality measure of a fit is the Q parameter given by the following formula

$$Q = \frac{1}{\Gamma(N_{DOF}/2)} \int_{\chi^2/2}^{\infty} y^{(N_{DOF}/2)-1} e^{-y} dy, \quad (3.45)$$

for which a derivation is found in the notes by P. Young [40]. $\Gamma(x)$ is the Euler gamma function defined by

$$\Gamma(x) = \int_0^{\infty} dt t^{x-1} e^{-t}. \quad (3.46)$$

This quantity Q gives the probability, that, for a certain fit, a different data set from the same probability distribution could have occurred with a χ^2 greater than or equal to the value, being found initially. It is assumed, that the unknown probability distribution generates the data points with a Gaussian noise. Therefore, the range of Q is $[0, 1]$, with 0.5 being optimal for a good fit. This can be explained as follows. A quality close to 1 amounts to a huge probability of a larger χ^2 on a different sample of the data for one fit. This implies, that the fit would not model the different samples as good as the sample, on which it was performed, also indicating a form of overfitting. On the other hand, a quality close to 0 means a larger probability for a smaller χ^2 with respect to a different set of data points. With regards to the minimizing procedure of the χ^2 , the fit parameters don't really minimize the χ^2 , because smaller values for the χ^2 on different samples of the data points are very likely. Therefore, small values of Q imply meaningless values of the fit parameters.

To gain insight in the development of possible fit ansätze, the finite size scaling formula of the kurtosis (3.42) is considered again. However, taking a step backwards, this formula is expressed without the Taylor expansion in the first term. The correction term is left unchanged and for convenience, the scaling variable is abbreviated as

$$x = \left(\frac{1}{m} - \frac{1}{m_c} \right) N_s^{\frac{1}{\nu}}, \quad (3.47)$$

where m_c is a fit parameter. The first term in formula (3.42) is written as a function of the scaling variable x : $F(x)$. Omitting the Taylor expansion, the resulting general kurtosis fit function is

$$B_4(x) = F(x)(1 + CN_s^{y_t - y_h}), \quad (3.48)$$

where the function $F(x)$ has to be expanded in some specific form of a function and higher orders of the correction term are neglected. The correction term does not play a role in the following discussion about the form of $F(x)$. However, there is always the option to turn it on or off by either using C as a fit parameter or setting it to zero.

It is useful to develop an imagination of the course of the kurtosis at β_c in the vicinity of m_c for different volumes N_s . A schematic illustration of the expected finite size scaling of the kurtosis at the Z_2 critical point is shown in figure 3.3. All kurtosis lines for different volumes share the same crossing point at the critical mass, where the kurtosis assumes the value from the Ising 3D universality class $B_4(\infty, Z_2)$ in the infinite volume limit. For inverse masses different from the inverse critical mass, the transition either turns into a crossover or a first order phase transition. Hence, the kurtosis in the infinite volume assumes either $B_4(\infty, CO) = 3$ for a crossover or $B_4(\infty, 1.O) = 1$ for a first order PT. The values of the kurtosis at β_c in the infinite volume limit correspond to the values shown in table 3.1. The course of the kurtosis for finite volumes should strive towards the infinite volume kurtosis values for inverse masses, that are sufficiently far from the critical point.

The straightest idea to represent $F(x)$ in a specific form is the use of polynomials of degree N to approximate the function $F(x)$, which is equivalent with a Taylor expansion

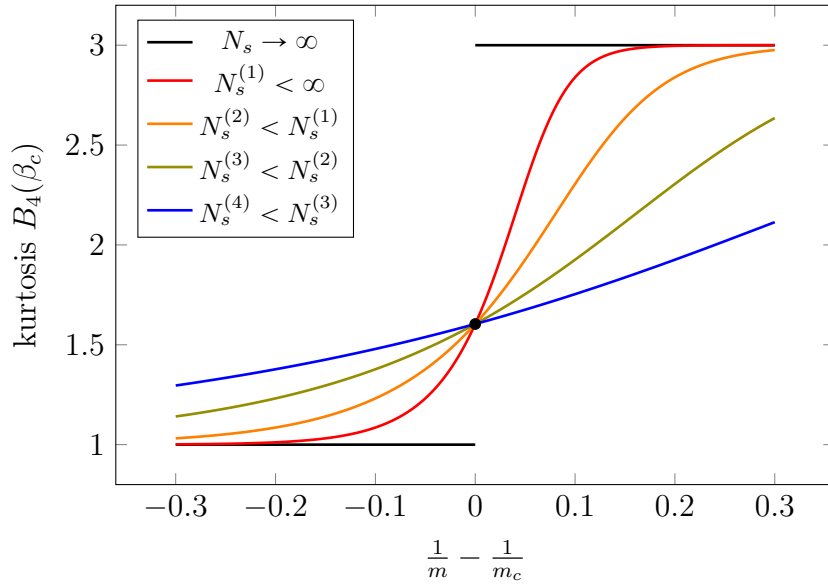


Figure 3.3.: Modeled course of the kurtosis at β_c for different volumes $N_s^{(i)}$ as a function of the inverse mass, showing the finite size scaling schematically. Here, the kurtosis of a purely magnetization like observable is shown, resulting in a common crossing point at $1/m=1/m_c$ and $B_4(\infty, Z_2)$.

to $\mathcal{O}(x^N)$. Hence, the resulting formula is

$$F(x) \approx a_0 + \sum_{n=1}^N a_n x^n, \quad (3.49)$$

where the a_n are the additional fit parameters. At the critical point, the scaling variable becomes 0 and as presented in table 3.1, the value of the kurtosis in the infinite volume limit at the critical point is known. Since $F(x=0)$ assumes the same value for every volume, meaning, that the curves of F for different volumes N_s have a crossing at $x=0$,

$$F(0) = a_0 = B_4(\infty, Z_2) \quad (3.50)$$

follows. This determines one parameter of the fit ansatz. Hence, the resulting polynomial ansatz for $F(x)$ is

$$F_P(x) = B_4(\infty, Z_2) + \sum_{n=1}^N a_n x^n, \quad (3.51)$$

with N fit parameters a_n . It is necessary to restrict the fit parameters to sensible ranges to prohibit oscillations of the fit function, for example. A monotonically increasing or decreasing course of the fit function has to be ensured.

If a polynomial fit ansatz fails to fit the kurtosis points around the critical point accurately, another suitable form of the function $F(x)$ has to be found. One example for a polynomial fit ansatz being insufficient, is the case of kurtosis points being located in the asymptotic region of the expected course of the kurtosis (see figure 3.3). This might happen, if the simulated masses are too far from the critical mass, such that the values almost assume the expected kurtosis values in the infinite volume limit in the crossover

or first order regime. Another possibility is a sufficiently large aspect ratio of some of the simulated points, leading to kurtosis values in the vicinity of the asymptotes, despite being close to the critical mass.

If these points, which the polynomial ansatz hardly catches for a good fit, can not be excluded, other fit functions have to be found, modeling the course of the kurtosis values also in the asymptotic regions far from the critical point. These functions are required to be monotonically increasing or decreasing and to fulfill the constraint, that $F(0) = B_4(\infty, Z_2)$. Additionally, the constraints from the asymptotes for kurtosis values far from the critical point shall be reflected in these functions. These constraints can be written as

$$F(\infty) = B_4(\infty, PT_r) \quad (3.52)$$

$$F(-\infty) = B_4(\infty, PT_l), \quad (3.53)$$

where the abbreviations PT_r and PT_l represent the type of phase transition on the right and on the left side of the critical point, respectively. Here, these transitions are either the crossover (CO) or the first order phase transition ($1.PT$). The notation and the numerical values are shown in table 3.1.

These constraints lead to considering suitable functions in the class of sigmoidal functions, because they exhibit constant asymptotes, as the argument either tends towards $-\infty$ or ∞ and they are monotonically increasing or decreasing. Due to the asymmetry of the crossing point of the curves with different volume N_s , only the functions accounting for this symmetry are considered for modeling the function $F(x)$. In the following, two possible candidates will be considered, namely the generalized logistic function and the Gompertz function. The general form of the generalized logistic function is

$$F_{GL}(x) = L + \frac{R - L}{(1 + Qe^{-rx})^A}, \quad (3.54)$$

where the parameters L, R, Q, r, A can be partially determined by the introduced constraints or serve as fit parameters. The constraints are applied to this form of the function in appendix B.2. The result is given here as

$$F_{GL}(x) = B_4(1.O, \infty) + \frac{B_4(CO, \infty) - B_4(1.O, \infty)}{\left[1 + \left(\left[\frac{B_4(CO, \infty) - B_4(1.O, \infty)}{B_4(Z_2, \infty) - B_4(1.O, \infty)}\right]^{\frac{1}{a}} - 1\right) \cdot \exp(-rx)\right]^a}, \quad (3.55)$$

where r and a are fit parameters. A flipped version of this formula, which is mathematically different from formula (3.55), is obtained by setting $r \rightarrow -r$ and interchanging $B_4(CO, \infty)$ and $B_4(1.O, \infty)$, wherever they occur. In appendix B.2, different possible parametrizations of this formula are shown.

In general, the Gompertz function [19] has the form

$$F_G(x) = L + R \exp(-Be^{-sx}), \quad (3.56)$$

where again the parameters L, R, B, s are either fitting parameters or to be determined by the given constraints. The result of the kurtosis fitting function is found in appendix

B.3, being shown here as

$$F_G(x) = B_4(1.O, \infty) + (B_4(CO, \infty) - B_4(1.O, \infty)) \exp\left(-\frac{\ln\left(\frac{B_4(CO, \infty) - B_4(1.O, \infty)}{B_4(Z_2, \infty) - B_4(1.O, \infty)}\right)}{\exp(sx)}\right). \quad (3.57)$$

The only fit parameter is s and a flipped version can be obtained similarly, as described above, with the difference $s \rightarrow -s$.

All these fit ansätze can be combined with the correction term from equation (3.48) and by fitting them to numerically obtained kurtosis data, the critical mass can be extracted as a fit parameter. In these formulas, m_c hides in the scaling variable x as well as the volume dependency of these fit functions. The fit ansätze can only be evaluated in combination with a kurtosis data set, which will be subject of section 4.3.

3.2. Numerical Tools

This section provides information about conducting the simulations and about the numerical tools used to process and analyze the data. These explanations are not detailed, but important references are given to enable the reconstruction of the data processing. In section 3.2.1, a brief overview over the software CL²QCD is given, which is used to produce the configurations. BaHaMAS is used to submit and monitor the simulations, as described in section 3.2.2. In section 3.2.3, a brief overview over the tool to analyze the data, named PLASMA, is given. The mass measurement and scale setting tools are discussed in section 3.2.4.

3.2.1. CL²QCD

All the Monte Carlo simulations for this master's thesis were performed with the lattice QCD code CL²QCD. This program was developed in the group of Prof. Owe Philipsen and a first publication about it was published in 2011 [28]. The code is online available on the Gitlab page of the Institute of Theoretical Physics of the university of Frankfurt. <https://gitlab.itp.uni-frankfurt.de/lattice-qcd/ag-philipsen/cl2qcd>.

CL²QCD is based on OpenCL, which is a standard for parallel programming, allowing the code to be run on CPUs or GPUs. The possibility to run the code on GPU is beneficial compared to code running on CPUs only. Some examples are the lower cost of acquisition per performance of GPUs and a better energy efficiency. The evaluation of exemplary GPU hardware with respect to these measures using CL²QCD has been investigated in [3]. Another important aspect is the better performance of GPUs for lattice QCD calculations in general. The reason is, that lattice QCD calculations are memory bandwidth limited and GPUs offer a comparatively high memory bandwidth [27].

The features of CL²QCD are the production of gauge configurations using different algorithms and the measurement of fermionic and gauge observables. The initial executables were `su3heatbath` for the generation of gauge fields for $SU(3)$ pure gauge theory, `hmc` for the generation of gauge fields for $N_f=2$ twisted mass Wilson fermions, `inverter` for the measurement of fermionic observables on given gauge configurations

and `gaugeobservables` for the measurement of gauge observables on given gauge configurations. Later, after staggered fermions had been added to the code and the Rational Hybrid Monte Carlo (RHMC) algorithm had been implemented, a new executable `rhmc` was added, which produces gauge configurations for staggered fermions [27]. An overview of the implementation of the RHMC algorithm for staggered fermions can be found in [34]. For this thesis, only the executables `rhmc` for the production of the gauge configurations and `inverter` for the measurement of pion masses were used.

The simulations, using CL²QCD, were conducted on the Lattice Computer for Scientific Computing (L-CSC) cluster at the GSI in Darmstadt on a partition with GPU-nodes, each consisting of AMD GPUs. For this thesis, only the GPUs of type FirePro S9150 with a Hawaii chip were used, where four of them build up one node. Further information about the L-CSC cluster can be found in [30]. On L-CSC, the simulations are handled by the program BaHaMAS, which simplifies to submit and monitor the simulations. The following section 3.2.2 contains a brief overview of some use cases of BaHaMAS.

3.2.2. BaHaMAS

As BaHaMAS played an important role in the everyday-work to handle the Monte Carlo simulations of this master's thesis, a brief description of this tool is given and some use cases are shown to get an insight in the efficient operation of CL²QCD by BaHaMAS. More information about BaHaMAS can be found in [33] and in the wiki associated to the publicly available Git repository <https://gitlab.itp.uni-frankfurt.de/lattice-qcd/ag-philipsen/BaHaMAS>.

The requirement of a huge number of Monte Carlo simulations is characteristic to thermal lattice QCD projects. Running them at the same time and monitoring them, requires a tool to save time and effort. This program BaHaMAS, mainly developed by Alessandro Sciarra, fulfills these requirements. In the following, only the most important features are described.

BaHaMAS is written in `bash` and can be operated via the command line. Currently, the cluster scheduler `slurm` and the lattice QCD codes `openQCD` and `CL2QCD` are supported. One important feature is the submission of jobs to run the simulations, either starting a new one, doing the thermalization or continuing a simulation. As an example, Monte Carlo simulations are continued with the command `BaHaMAS continue` and some optional command line options. Subsequently, BaHaMAS evaluates a `betas` file, containing information like the β and seed values. On the basis of this information and meaningful directory names, it produces a job script and an input file for CL²QCD to submit the simulation with the job scheduler on the cluster. Another important feature of BaHaMAS is the database functionality (`BaHaMAS database`), which helps a lot to monitor the huge amount of simulations. For each simulation, the status and the collected trajectories are shown. However, also quantities indicating the health of the simulation are displayed, for example the acceptance rate or `maxSpikeDS/s`, which is the maximum number of standard deviations from the mean of the Hamiltonian for any trajectory. A large `maxSpikeDS/s` suggests that, at some trajectory, the numerical values of the Hamiltonian are in a unreasonable range, often indicating a broken GPU. Hence, BaHaMAS simplifies checking huge amounts of simulations for accurate calculations every day.

3.2.3. PLASMA

Having obtained the data from CL²QCD, an analysis of the data and if necessary a reweighting of some observables has to be performed. For this purpose, PLASMA was initially developed by Christopher Pinke, but since then, it was refactored and maintained by Francesca Cuteri and Alessandro Sciarra. The name PLASMA represents **P**ython **L**ibrary for **A**utomatized **S**tatistics **M**anagement and **A**nalysis. As the title suggests, PLASMA contains more functionality than just analysis and reweighting, but this overview will be limited to the two features analysis and reweighting, mainly used in this thesis. Currently, PLASMA is not yet released, as a refactoring and updating project by Alessandro Sciarra and David Palao is bringing the software to a new releasable state. The new version will be available at <https://gitlab.itp.uni-frankfurt.de/lattice-qcd/ag-philipsen/plasma> and some general information about PLASMA can be found in the eponymous section of the AG Philipsen Workflow [32].

In the following, the usage of PLASMA is described in more detail, mainly to track the data analysis and the reweighting for this thesis. In general, PLASMA is one main `python` script with different modes, depending on the command line options passed to the script. The observables are analyzed with the mode `A` and they are reweighted with the mode `r`. The options to be used in both modes are:

- `--analyzeWithJackknife`: This option performs the jackknife of the specified observables according to section 3.1.2.
- `--analyzeSingleChains`: Using this option, not only the merged chains, but also the single chains for one specific β , are analyzed separately.
- `--deactivatePlaq`: This point also represents all the observables not being analyzed in this run of the analysis, in this case it is the plaquette.

In the following, the options, being used in combination with the reweighting mode, are:

- `--doNotUseSimulatedPointsAsNewPoints`: When using this option, the data points, depending on β , which come from the pure analysis of the simulations, are not taken into the end result of the interpolated data points. Only the reweighted data points are taken into account.
- `--newBetaRange` specifies the range of the reweighting of the observables. Always, the smallest and the largest simulated β values were used as standard values for this range.
- `--newPoints` is the option, giving the number of points, for which the observables are reweighted. The number, applied for thesis, depends on the formula

$$n = \frac{\beta_{max} - \beta_{min}}{0.0001}, \quad (3.58)$$

thus, keeping the distance of the reweighted β -values constant at $\Delta\beta = 0.0001$.

Another important feature of PLASMA is the extraction of the critical beta from the reweighted observables with the mode `bC`. Therefore, the skewness is analyzed for a zero-crossing, implying, that the β -value, for which the skewness is closest to zero, is taken

as the critical β . The corresponding kurtosis value can be extracted from the reweighted kurtosis-data at the critical β with an extra `bash`-script. The result is a data file for one specific N_τ , containing the kurtosis values at the critical β as a function of the spatial extent N_s and the mass values. This file serves as input file for the fitting tool PFG (see section 3.3).

3.2.4. Mass Measurement and Scale Setting Handling

As all the steps from the Monte Carlo simulations to the analysis of the observables and the determination of the critical mass are conducted using lattice units, finally, these quantities have to be expressed in physical units. The measurement of the pion mass is required, as the quark mass from the simulations is a bare parameter. Additionally, the scale setting determines the lattice spacing in physical units and thus all other lattice unit quantities like the pion mass. The two tools used for these purposes are briefly introduced here.

Starting with the measurement of the pion mass, the configurations are generated with CL²QCD on a $N_\tau=32$ and $N_s=16$ lattice, consistently. The quark correlators are measured on these configurations, also using the CL²QCD software leading to eight correlator files for each configuration. These correlator files can be used by a script called `massMeasurementHandler.sh` to obtain the pion mass in lattice units. This script is a wrapper around Matlab scripts, which perform the actual mass calculation. Beforehand, the quark correlator files are converted to a suitable format to be used for the computation of the specific correlators. There is the option to specify the type of meson, which is the pseudo-scalar meson for measuring the pion mass in this case. As a last step, the pion mass is extracted from the plateau of the effective mass vs. $n_t \in [0, N_\tau/2 - 1]$ plot by using a fit. A fit range has to be specified, spanning the flat region of the plateau. The errors are calculated using a Matlab code by Ulli Wolff [39].

Having obtained the pion mass in lattice units, it has to be converted to physical units as well as other quantities like the temperature. For the scale setting, the same configurations as for the pion mass measurement are used. As the external scale setting code relies on a different format of the configurations, they are converted correspondingly beforehand. The conversion and scale setting are handled together within a script called `scaleSettingHandler.sh` and optionally another one called `ProduceJobToRun_scaleSettingHandler.sh`. The latter one is designed to run the scale setting on a super computer as it takes a considerably large amount of computational time. Having converted the configuration files to the `nersc` format, the Wilson flow [23] is evaluated on each configuration by the external `wilson_flow` code, which is written in C [6]. Using the Wilson flows, the quantity w_0 is calculated in lattice units, which allows to convert the temperature and the pion mass to physical units with the script `scaleSettingHandler.sh`.

3.3. Python Fitting GUI

One of the main goals of this thesis was the development of a tool to easily produce many different fits. The file, containing the kurtosis values at the critical β s is given as input file. The results of the fit, namely the resulting fit parameters and some quality

measures, have to be displayed. Additionally, the plot of the fit on top of the used data points has to be shown.

It turned out, that Python is the programming language for this project for several reasons. In the beginning of this project, the author was already familiar with programming in Python. Another reason is the large pool of libraries in Python, allowing easy plotting and fitting, for example. In general, Python is well suited for data analysis projects.

Additionally, it was decided to develop this program as a graphical user interface (GUI). Exemplary advantages are the handy performing of different fits by clicking and at the same time viewing the result as a plot. A drawback is, that it cannot be operated and therefore automatized from the command line. However, this seems not to be a big problem, since the fitting of the kurtosis is the last step in obtaining a critical mass and a monitoring of the fits by eye is always mandatory.

In this section, the program will be explained in more detail, as the PFG is described here for the first time. First, a brief motivation for the need of a completely new program is given, outlining the abstract features, the GUI should be capable of. Subsequently, an overview over the structure of the code of the program is described, including the most important implementation details. Thereafter, the available fit functions are presented and their use is explained. In the end, it has to be justified, that the fitting results are correct. Hence, some tests with sample data have been conducted and compared to a different fitting tool.

The program is not publicly available, but for members of the Institute of Theoretical Physics (ITP) at the University of Frankfurt, the code can be accessed in the Gitlab repository of the ITP, following the link <https://gitlab.itp.uni-frankfurt.de/lattice-qcd/ag-philipsen/python-fitting-gui>. An incomplete wiki is affiliated to this Gitlab repository, but it only contains a page about the available fit functions.

3.3.1. Motivation

As already a script in gnuplot to perform kurtosis fits existed, it is necessary to motivate the implementation of a completely new fitting program. The gnuplot script is operated by giving command line options, specifying the fit function. Different sets of data points can be selected by commenting out the corresponding lines in the file of the kurtosis values at the critical β . This is time consuming, whenever the selection of the data points or the choice of the fit function is changed.

Therefore, the idea was to concentrate the selection of the data points, the choice of the fit function and the fit result as well as the plot of the fit into one window. A further improvement is the availability of buttons, check boxes and similar elements in a GUI. A click selects a data point and checking a checkbox modifies the fit function. As a GUI allows extending the functionality of these basic features of fitting and plotting, some useful additional features should be integrated into the new program. As many different possible fits exist, regarding the selection of data points and the choice of the fit function, it is beneficial to compare fits and therefore save them in the GUI, allowing access to the results and to replot the corresponding fit. Also, a graphical comparison of the values being obtained by different fits should be possible. The resulting fit parameters are compared in a stability plot. Some minor goals were the possibility to modify the plot and the presentation of the fit results supported by colors (i.e. the quality measures of

the fit). This seems to be a less important feature, but time is saved when evaluating the fits.

On the side of the code, the goal was the implementation of a program with a well readable and well structured object-oriented code in Python, following PEP 8, the style guide for Python code [31]. Another important goal for the code was the possibility of easily extending and generalizing it. Especially, the possibility to implement new fit functions in a simple way, without interfering in many parts of the code, was an important goal. The simplification of implementing new fit functions has progressed, but the current solution is not optimal. Another subtle goal is the sensible handling of undefined or erroneous user input as well as the handling of internal errors of the program. The search for and the localization of as many cases as possible, where errors can occur, are very delicate. Throughout the development of the GUI, the error handling has improved, as the code was tested by a lot of trial and error. However, this cannot guarantee the detection of all cases of errors and there still might be better solutions for the handling of internal errors of the program.

3.3.2. Overview over the Structure

Python structures the code of programs by modules, which are files containing functions and classes. The relations of the modules of the program Python Fitting GUI are shown in figure 3.4. The kernel is the module `fitting` defining the fit functions and performing the fitting. The module `data_io` provides the functions and classes to read from the data file with the kurtosis values and pass it to the fitting module. The results from the fitting and the data points are passed to the module `plotting`. The code-wise largest module `gui` displays the plot, the results and operational elements in a Qt5-window. There are some minor modules (see right part of figure 3.4), also being discussed briefly in the following. A paragraph is devoted for each other module, explaining the most important properties. This detailed description of the program code also serves as a starting point for users of the code, who want to manipulate the code for their specific use cases.

`data_io`

As the name of this module suggests, it handles the input and output of the kurtosis data. The kurtosis at the critical β for all the simulations is collected in a file of a certain format. The data in this file has to be arranged in columns containing the mass, the volume, the kurtosis and its error with a suiting header. Currently, either `mass` or `k` (for κ) are supported as header for the mass with Staggered fermions or the hopping parameter with Wilson fermions, respectively. The basic class `DataContainer` processes this input file. When instantiating, it takes the filename as argument and having loaded the data, it provides several methods to easily access the kurtosis data. Another method exports the data and saves it in a file. This class does not only handle the data input and output, but also instantiates the dynamic objects, storing the state of selected and unselected data points. An important external module being used by this class is `numpy`, which is publicly available and can be found at <https://numpy.org/>. It contains many mathematical functions and classes, which are used in the PFG.

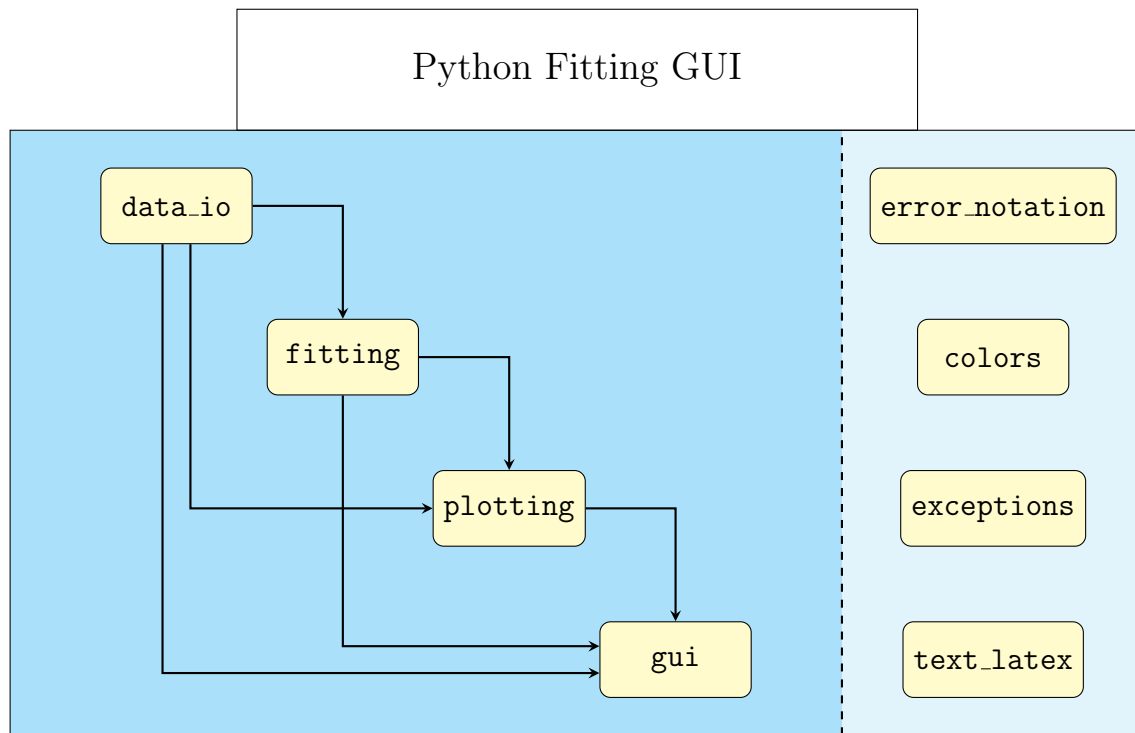


Figure 3.4.: Flow chart of the structure of the PFG modules, indicating the dependence of the main modules and showing the minor ones on the right side.

fitting

The fitting procedure is divided into two separate parts. One part only considers the definition and handling of the fit functions. This includes the creation of a Python function, being handed over to the function, that performs the actual fit. In this part, also constants and fit parameters are defined, including \LaTeX -code describing the complete fit formula. The other part only considers the fitting process. A class for a `Fit`-object is implemented, which takes a fit function as argument and performs the fit on the given data.

The base class `FitFunction` only serves as an example for the definition of new fit functions and is not applied for fitting to data in this project. One important method to be reimplemented, when inheriting from this class, is `_create_fit_function(self)`. This method defines the function, being used in the class `Fit` as actual fit function. It also returns the created fit function, becoming an attribute of the object `FitFunction`. Additionally, some methods exist to define the names of the fit parameters and the constants used in the fit formula. The fit formula has to be a string in \LaTeX -code to be compiled and displayed as an image by the other modules of the PFG. Still, some delicate details have not been mentioned, especially considering the specific kurtosis fit functions, but it is left to the interested reader to look at the code.

The second part of the module `fitting` is the class `Fit`. It takes an object of the type `FitFunction` and the kurtosis data, which is an object of the type `DataContainer`, as arguments. The following code snippet shows the definition of this class and the beginning of the `__init__`-method, indicating, that the data and the fit function of a certain fit can always be accessed through the attributes of this object of type `Fit`.

```

1 class Fit:
2     """This class can instantiate a fit object which fits the kurtosis
3     data given by the data argument to the fit
4     function given by the fit_function argument."""
5     def __init__(self, data: data_io.DataContainer, fit_function:
6         FitFunction):
7         self.data = data
8         self.fit_function = fit_function

```

The most important method of the class `Fit` is the function `fit(self)`, which actually performs the fit. There, all the fit options, being set before by various other methods of this class, are handed over to the `curve_fit`-function from the external `scipy`-module. `scipy` is a library for fundamental scientific computing and is publicly available at <https://www.scipy.org/>. An article about `scipy` [36] focuses on the capabilities of `scipy` and some development practices. However, the specific documentation of the function `curve_fit` from the module `fitting` can be found at https://docs.scipy.org/doc/scipy/reference/generated/scipy.optimize.curve_fit.html. The code fragment, where `curve_fit` is employed, is shown for a more detailed examination of the function `curve_fit`.

```

1 p, cm = curve_fit(self.fit_function.function, self._masses_nss,
2                 self._kurtosis, sigma=self._kurtosis_error, absolute_sigma=True,
3                 p0=self._initial_parameters, bounds=self._boundaries,
4                 method=self._fit_method)

```

The return values of the function `curve_fit` are the fitted parameters `p` and the covariance matrix `cm`. `curve_fit` takes the fit function as first argument. An array `self._masses_nss` combining the mass and volume data is handed over to the function, after which the corresponding kurtosis values also enter the function as an array. Additionally, there is the option to specify the absolute error on the kurtosis data with the keyword `sigma` and setting the keyword `absolute_sigma` to `True`. The keyword `p0` takes an array with the initial values for the optimization of the fit parameters. Some optimization algorithms, being specified by the keyword `method`, can use boundaries (`bounds`) on the fit parameters to restrict the fit range. More details, concerning these options, are given in the documentation cited above. The values of these options have to be set before executing the function `fit(self)` of a `Fit` object by calling the corresponding methods.

All the fit results can be derived from the parameters `p` and the covariance matrix `cm`. How these results (e.g. errors on the parameters, quality, etc.) are obtained, is not discussed here, but the source code is referenced, which contains methods of the class `Fit` for every relevant quantity.

plotting

The next important issue is visualizing the results of the fit by plotting the fit function along with the corresponding data. This module `plotting` relies on the external library `matplotlib`, also being publicly available at <https://matplotlib.org/>. `matplotlib` is a Python library to visualize data in all facets and as a further-reading, an article by the lead developer of `matplotlib`, John Hunter, is cited [20].

The base structure of this module are functions, plotting the data, the fit or the title to an `Axes` object of the `matplotlib` library. The `Axes` object can be described as a coordinate system within a figure, which can be shown or exported as a PDF file. These plotting functions take the data, the fit or information about the plot title as arguments. The arguments are processed in the body of these functions to obtain a nice visualization of the data and the fits. Details of the appearance can be tuned by the user of these functions, but this brief overview of the module `plotting` does not cover this aspect.

gui

The module `gui` unites the functionality of the previously described modules into a graphical user interface (GUI). The GUI is implemented by using the external library `Pyside2`, which provides access to the Qt5 framework. Qt5 is a cross-platform toolkit for development of GUIs written in C++. This is, why `Pyside2` is a Python binding of Qt5, thus allowing Python to use the original Qt code. The wiki pages can be found at https://wiki.qt.io/Qt_for_Python and `Pyside2` is publicly available under the GNU general public license.

The details of implementing the GUI of this fitting tool, concerning the handling of user input and the design of the layout of the application, are more complicated. Covering this would go beyond the scope of this thesis. Instead, the appearance and the operational elements of the GUI are explained. Additionally, it is discussed in what extent some of the goals from section 3.3.1 could already be achieved.

The main window of the PFG is shown in figure 3.5. The numbered frames have been included to simplify the description of the different elements of the layout of the PFG. 1 labels the plotting area, showing the kurtosis B_4 as a function of the inverse mass $\frac{1}{m}$ (m in lattice units). The dots with error bar visualize the simulated data points and the solid lines represent the fit function. The different volumes N_s are represented by different colors and the translucent points in the plot are data points, which were not included in the fit. The points in this plot are shifted horizontally around their actual value to allow a better distinction of different volumes and to avoid overlapping points with the same mass value. In frame 2, the fit results are displayed below the plotting area. The fit formula of the currently plotted fit is displayed on top. The lower left box gives the values of the fixed constants, being used in the fit formula. In the middle, the results of the fit parameters are given, including the errors in brackets. In the right box, the measures concerning the quality of the fit are displayed. This includes the number of degrees of freedom ndf , the χ^2 per number of degrees of freedom and the Q parameter. The colors of the χ_{ndf}^2 and Q indicate the distance of the current values to the optimal values $\chi_{ndf,opt.}^2 = 1$ and $Q_{opt.} = 0.5$. Green is very close and over yellow and orange the values recede from the optimal ones, arriving at red indicating a huge distance to the optimal values. In frame 3, the control elements to adjust the fit form, the fit options and some plot options are shown. The fit form consists of one base function, choosing either the polynomial fit, the general logistic fit or the Gompertz fit and the possibility of adding the correction term. The details of the implemented fit functions will be described in section 3.3.3. The fit options can be modified in another tab, which are highly related to the options, being passed to the function `curve_fit()`, as described in `fitting`. The plot options allow to modify the plot, being shown in the plotting area. As an example, the small horizontal shift can be turned on and off on this tab. Below these tabs, several

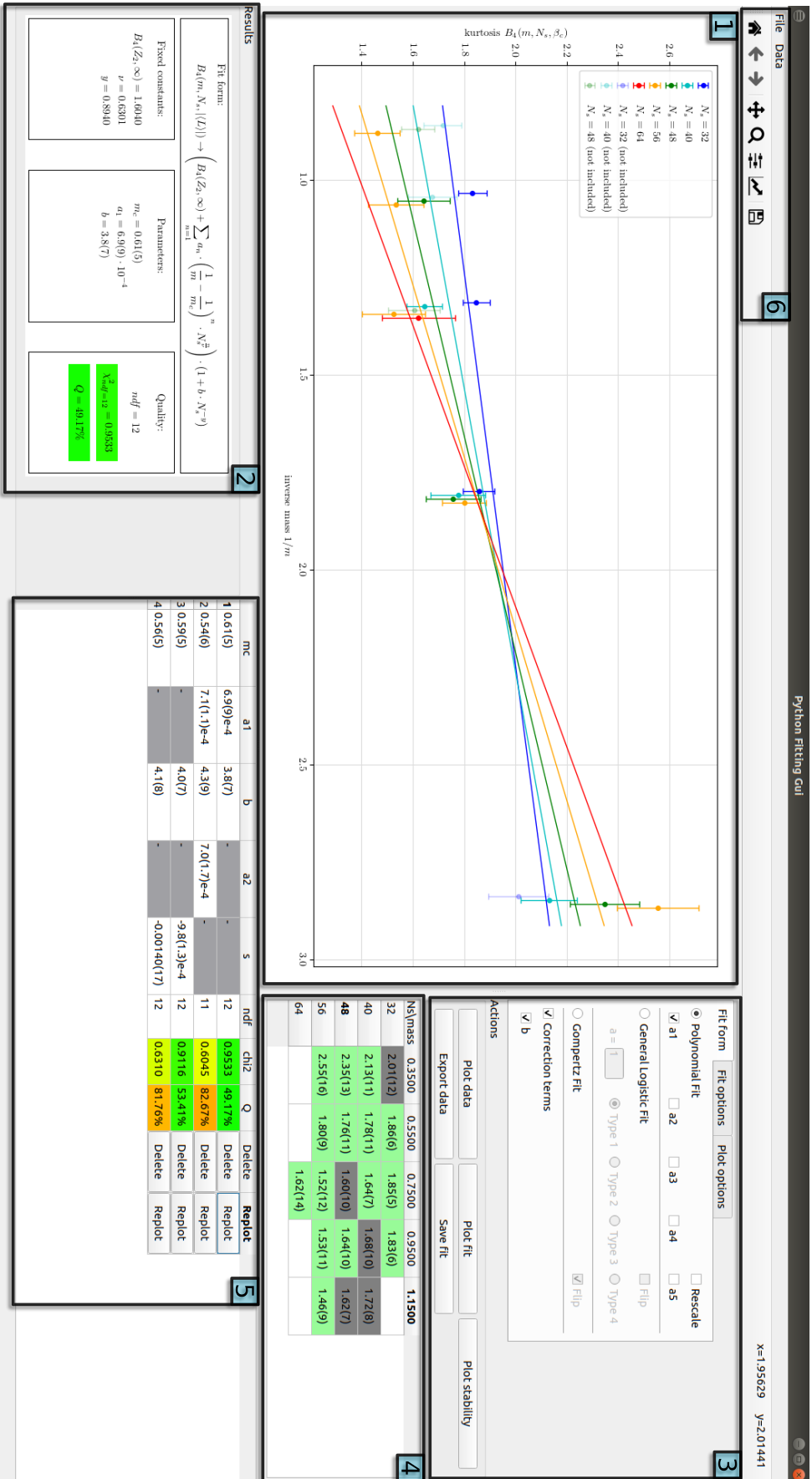


Figure 3.5.: The main window of the PFG with sample data and fits. The frames were added to allow a structured description of the layout elements. [1] plotting area, [2] display of the fit results, [3] control elements to adjust the fit or the plot, [4] table with the data points of the kurtosis, [5] table of the saved fits, [6] rudimentary menu and control elements of the matplotlib backend for Pyside2 to modify the figure with the plot.

buttons induce the execution of some actions. The *Plot data* button only plots the data points without the fit function. The *Export data* exports the data into a data file of the same format as the input data file. Additionally, it adopts the selection of data points by commenting out the corresponding lines. The *Plot fit* button plots the fit and the data points to the plotting area, depending on the choices from the tabs and the selection of data points. The *Save fit* button saves the currently displayed fit into the table of the saved fits in frame [5]. The last button *Plot stability* also uses the plotting area to plot one or two columns of the saved fits table. Therefore, the columns have to be selected before by clicking on the headers of the columns of the saved fits table. In frame [4], the table of the data points is shown, where each row stands for one volume N_s and each column for one mass value. The kurtosis value with the error in brackets is shown inside the cells. Clicking on these cells selects or deselects that specific data point. A green background indicates a selected data point, whereas a grey background indicates a deselected data point. A white cell indicates a non-existing combination of volume and mass in the data. In frame [5], the saved fits are shown in a table, where each line represents one saved fit. The columns on the left contain the values of the fit parameters, if they exist for that type of fit. The number of degrees of freedom, the χ^2 per degree of freedom and the Q parameter are displayed in the next columns, adopting the same color scheme from the display of the fit results. Furthermore, there is the possibility to delete each saved fit, removing the corresponding line in the table. The fit can be replotted to the plotting area and the control elements (check boxes, radio buttons, etc.) in the tabs as well as the table of the data points are adjusted to the status of the saved fit. Finally, in frame [6], a rudimentary menu is displayed, containing some self-explaining actions related to keyboard shortcuts. Some buttons from the `matplotlib` back-end for `PySide2` are placed underneath, allowing an elementary configuration of the figure, containing the plot. There, the figure can be saved to a file.

The goal of an easy switching between different fit function has been achieved, as becomes apparent in frame [3]. All possible combinations of fit parameters can be adjusted by just clicking on check boxes or radio buttons. One drawback still is, that the variety of fit functions is restricted to the ones, being implemented in the source code. One improvement would be to allow user input of own fit functions. The table of the data points in frame [4] shows the simple selection and deselection of data points. Additionally, the used data points can be seen. Two more goals are fulfilled by the saved fits table. First, this offers the possibility to replot several fits and compare them. Secondly, a stability plot can be performed, allowing a graphical comparison of the fit parameters of different fits. This gives a good overview over the fits and allows a profound evaluation. By closing the program PFG, the saved fits are lost and currently, there is no possibility to save these fits to a file and reload them later or in an external session of the program. This improvement would allow to prepare a fit analysis of a data set and present it to or share it with other researchers. This feature remains a goal of the future.

This concludes the description of the main window of the GUI. Some details have not been explained, however, the mostly self-explanatory elements are an advantage of GUIs. Examples are warning or error messages, which pop up at an occurrence of an error. The displayed message is sufficient for the user to understand and avoid the problem.

`colors`, `error_notation`, `exceptions`, `text_latex`

These are all essential modules for the program, but they are of minor importance for the process of fitting and analyzing the fits. Thus, for completeness, a brief description is given for all of them. The `colors` module handles the display of the correct colors in the plot and the quality measures of the fit. The module `error_notation` implements the representation of the correct errors for all quantities having errors. The values of those quantities are rounded and the corresponding error is displayed in brackets. To handle program internal errors, the module `exceptions` contains specific exception classes. The last module `text_latex` contains functions, which produce the tex-files for the fit results box. Subsequently, these tex files are compiled with `pdflatex` and the pdf version is converted to a png image, which is displayed in the GUI.

3.3.3. Available Fit Functions

This section gives an overview over the currently available fit functions and relates the possible choices in the fit form tab (see figure 3.6) to formulas. The formulas are derived in appendix B. In the following, the formulas are presented, being the result of a particular combination of selected check boxes and radio buttons

Figure 3.6.: The fit form tab, showing all available fit functions. The detailed description and the corresponding formulas are given in the text of section 3.3.3 and in appendix B.

As an overall principle, the implemented kurtosis fit functions all have the general form

$$B_4(m, N_s) = F(m, N_s) \cdot C(N_s), \quad (3.59)$$

where $F(m, N_s)$ is a model function for $F(x)$ in the formula (3.48) and $C(N_s)$ is the correction term function. The radio buttons *Polynomial Fit*, *General Logistic Fit* and *Gompertz Fit* select one of these functions to model $F(x)$. Thus, the selection of these functions is exclusive and a selection of one of them is mandatory. The correction terms $C(N_s)$ can be switched on with the first check box, as this enables the possibility to

switch on the coefficients of the Taylor expansion of the correction terms. Currently, only the first order is implemented, being denoted by b . A deselection of the correction terms implies $C(N_s) = 1$. If b is selected,

$$C(N_s) = 1 + bN_s^{y_t - y_h}, \quad (3.60)$$

where y_h, y_t are the critical exponents introduced in section 2.1.2.

In the following, only the model functions $F(m, N_s) = F(x)$ are considered. They can also be written as functions of the scaling variable x , as shown in equation (3.47). The basic formula of the *Polynomial Fit* is

$$F_P(x) = B_4(Z_2, \infty) + \sum_{n \in M} a_n x^n, \quad (3.61)$$

where M is a subset of $\{1, 2, 3, 4, 5\}$. Consequently, any combination of the coefficients a_n can enter the fit formula by selecting the corresponding check boxes. Checking the *Rescale* check box, multiplies the sum in equation (3.61) with a factor $R(x)$, leading to

$$F'_P(x) = B_4(Z_2, \infty) + R(x) \sum_{n \in M} a_n x^n. \quad (3.62)$$

$R(x)$ can be expressed, using the Heaviside step function $\Theta(x)$,

$$R(x) = 1 + (f - 1)\Theta(x), \quad (3.63)$$

where $f = 0.4327$. A motivation for this rescaling term can be found in appendix B.1.

Having selected the *General Logistic Fit*, one of the 4 types of the general logistic fit functions has to be selected. The first one allows to manually choose the asymmetry parameter a of the generalized logistic function

$$F_{GL,12}(x) = B_4(1.O, \infty) + \frac{B_4(CO, \infty) - B_4(1.O, \infty)}{\left[1 + \left(\left(\frac{B_4(CO, \infty) - B_4(1.O, \infty)}{B_4(Z_2, \infty) - B_4(1.O, \infty)}\right)^{\frac{1}{a}} - 1\right) \cdot \exp(r \cdot x)\right]^a}. \quad (3.64)$$

The fit parameter r is the growth rate. The *Flip* check box interchanges the two constants $B_4(1.O, \infty)$ and $B_4(CO, \infty)$. Additionally it adds a minus sign in front of r . Thus, the result is

$$F_{GL,12}^f(x) = B_4(CO, \infty) + \frac{B_4(1.O, \infty) - B_4(CO, \infty)}{\left[1 + \left(\left(\frac{B_4(1.O, \infty) - B_4(CO, \infty)}{B_4(Z_2, \infty) - B_4(CO, \infty)}\right)^{\frac{1}{a}} - 1\right) \cdot \exp(-r \cdot x)\right]^a}, \quad (3.65)$$

where the flip is shown once, as the flipped formula will be omitted for the other types of the *General Logistic Fit* and the *Gompertz Fit*. The second type of the *General Logistic Fit* is expressed with the same formula as type 1, but the asymmetry parameter a turns into a fit parameter as well.

For the third type, the same basic generalized logistic function was used to derive the fit formula, but the constraints were used differently to eliminate a and to keep q . This might make a difference in the numerical fitting process. The resulting formula is

$$F_{GL,3}(x) = B_4(1.O, \infty) + \frac{B_4(CO, \infty) - B_4(1.O, \infty)}{\left[1 + q \cdot \exp(r \cdot x)\right]^{\log\left(\frac{B_4(CO, \infty) - B_4(1.O, \infty)}{B_4(Z_2, \infty) - B_4(1.O, \infty)}\right) \log^{-1}(1+q)}}, \quad (3.66)$$

where r and q are the fit parameters.

The fourth and last type of the *General Logistic Fit* is a linear combination of exponentials in the denominator to avoid the numerically difficult to handle asymmetry parameter a . The formula is

$$F_{GL,A}(x) = B_4(1.O, \infty) + \frac{B_4(CO, \infty) - B_4(1.O, \infty)}{1 + q \cdot \exp(r_1 x) + \left(\left(\frac{B_4(CO, \infty) - B_4(1.O, \infty)}{B_4(Z_2, \infty) - B_4(1.O, \infty)} \right) - 1 - q \right) \cdot \exp(r_2 x)}, \quad (3.67)$$

where r_1, r_2 and q are the fit parameters. In general, fitting to this formula is very complicated due to the poles that may occur in the denominator. Actually, this fit formula has never been used on kurtosis data to evaluate fit parameters like m_c . This type is only given here to show the complete set of implemented functions.

The *Gompertz Fit* cannot be varied, except for the *Flip*. The formula is

$$F_G(x) = B_4(1.O, \infty) + \frac{B_4(CO, \infty) - B_4(1.O, \infty)}{\exp \left[\ln \left(\frac{B_4(CO, \infty) - B_4(1.O, \infty)}{B_4(Z_2, \infty) - B_4(1.O, \infty)} \right) \cdot \exp(s \cdot x) \right]}, \quad (3.68)$$

where s is the only fit parameter. The derivation of the explicit form of this fit function is subject of appendix B.3.

3.3.4. Tests

It is always useful to test newly developed programs. Possible failures in displaying the data and the fit and interaction problems of the GUI are not considered here, but faulty fit results. The correctness of these values is very important, as the fit parameters and the quality of the fit are used to draw physical conclusions. As a fitting script for specific kurtosis fit functions already existed, it was decided to compare the results of both programs to evaluate the correctness of the fitting procedure of the PFG. This is also motivated by the difference of the numerical frameworks of both approaches. The script `BinderFitVSmass.sh` uses the `fit` command of `gnuplot`, allowing multi-branch fits. As already stated in section 3.3.2, the PFG uses the function `curve_fit` from the `scipy`-module.

Since the script `BinderFitVSmass.sh` is only capable of some specific fit functions, only linear and cubic fits with and without correction term are compared, leading to four different fit functions to test. The corresponding fit formulas are named and expressed as follows:

linear

$$B_4(m, N_s, |\langle L \rangle|) \rightarrow B_4(Z_2, \infty) + a_1 \cdot (m - m_c) \cdot N_s^{\frac{1}{\nu}} \quad (3.69)$$

linear with correction

$$B_4(m, N_s, |\langle L \rangle|) \rightarrow \left(B_4(Z_2, \infty) + a_1 \cdot (m - m_c) \cdot N_s^{\frac{1}{\nu}} \right) \cdot \left(1 + b \cdot N_s^{y_t - y_h} \right) \quad (3.70)$$

cubic

$$B_4(m, N_s, |\langle L \rangle|) \rightarrow B_4(Z_2, \infty) + \sum_{n=1,3} a_n \cdot (m - m_c)^n \cdot N_s^{\frac{n}{\nu}} \quad (3.71)$$

cubic with correction

$$B_4(m, N_s, |\langle L \rangle|) \rightarrow \left(B_4(Z_2, \infty) + \sum_{n=1,3} a_n \cdot (m - m_c)^n \cdot N_s^{\frac{n}{\nu}} \right) \cdot (1 + b \cdot N_s^{y_t - y_h}) \quad (3.72)$$

The fits are compared for the scaling variable $(m - m_c)N_s^{1/\nu}$, instead of $(1/m - 1/m_c)N_s^{1/\nu}$, because this is the only mass dependent scaling variable, for which the script `BinderFitVSmass.sh` can perform fits. This is not a problem at this point, because the results are not of physical interest here. The mass m is given in lattice units. The tests are performed for one data set of kurtosis values for $N_f=2$ staggered fermion simulations at $N_\tau=8$ and $\mu_i=0$. The used numerical data is provided in appendix C in table C.1. To increase the test cases and the possibility to hit an exceptional case of a failure of the fitting, three subsets of this data set are built and tested for all four different fit functions. The three different subsets of the complete data set of kurtosis points can be described as follows:

data set 1 All data points are included in the fits

data set 2 The data points with $N_s=32$ and $am=1.15$ are excluded.

data set 3 The two smallest volumes $N_s=32, 40$ are excluded from the fits.

For all tests, the initial values for the fit parameters were set to 1, for the PFG and the script. As the fit function of gnuplot always employs the Levenberg-Marquard algorithm for finding the optimal fit parameters, this option was also chosen in the PFG.

The results of the fit parameters and its errors and the χ_{ndf}^2 are compared, omitting the Q parameter, as it only depends on the number of degrees of freedom ndf and on χ_{ndf}^2 . It was decided to compare 6 relevant digits, as this is much more precise than the typical errors of the parameters. Some deviations of both programs can be found with this precision, as can be seen in table 3.3. It shows the test results for the cubic kurtosis fits. This comparison is used as an illustrative example of the occurrence of deviations. The other tables, comparing fit results of the remaining fit functions, can be found in appendix C. Some numbers in these tables show up with less than 6 digits implying, that the missing relevant digits are trailing zeros, which are cut off. For a better visualization, the deviations have been marked according to a color scheme. If no color is applied to a cell, there is no deviation of the result from the PFG x_{PFG} to the result of the script x_S within the 6 relevant digits. The deviations δ are determined by $\delta = |1 - x_{PFG}/x_S|$ and table 3.2 gives the color scheme. The color, corresponding to the larger deviation in a cell, either of the fit parameter or its error, is applied to that cell.

range of δ	color
$[10^{-6}, 10^{-5})$	blue
$[10^{-5}, 10^{-4})$	green
$[10^{-4}, 10^{-3})$	yellow
$[10^{-3}, 10^{-2})$	orange
$[10^{-2}, 10^{-1})$	red

Table 3.2.: Colors in tables C.2, C.4, 3.3, C.5

The results of the comparison of the test data are briefly discussed here. First, the linear fits do not exhibit any deviations. The linear fit with correction term also shows only very occasional and very small deviations. Bigger deviations start to rise with the cubic fit, where deviations in the range of 10^{-4} to 10^{-2} are found in the fit parameters. Even

	program	$m_c \pm \Delta m_c$	$a_1 \pm \Delta a_1$	$a_3 \pm \Delta a_3$	χ_{ndf}^2
data set 1	PFG	1.00987 ± 0.0505843	-0.000990514 ± 0.000268658	-7.53625 · 10 ⁻⁹ ± 3.54622 · 10 ⁻⁹	3.9358
	Script	1.00882 ± 0.0502655	-0.000994701 ± 0.000268509	-7.54742 · 10 ⁻⁹ ± 3.56071 · 10 ⁻⁹	3.93585
data set 2	PFG	0.817362 ± 0.0487578	-0.000894939 ± 0.000494623	-3.75045 · 10 ⁻⁸ ± 1.52875 · 10 ⁻⁸	1.12099
	Script	0.817425 ± 0.0487703	-0.000894948 ± 0.000494983	-3.74854 · 10 ⁻⁸ ± 1.52821 · 10 ⁻⁸	1.12099
data set 3	PFG	0.886779 ± 0.036425	0.000151856 ± 0.000398336	-3.39107 · 10 ⁻⁸ ± 1.11687 · 10 ⁻⁸	0.848554
	Script	0.886762 ± 0.0364099	0.000151941 ± 0.000397994	-3.3915 · 10 ⁻⁸ ± 1.11699 · 10 ⁻⁸	0.848554

Table 3.3.: comparison of the fit results for the cubic kurtosis fit

larger deviations up to $\delta = 10^{-1}$ occur with the cubic fit with correction term. The deviations mainly affect the fit parameters, lesser the χ_{ndf}^2 . A trend becomes apparent: The results of the fit parameters are becoming prone to deviations, the more non-linearities the fit ansatz contains. Even the correction term, being multiplied with the polynomial, implies a non-linearity for the fit function. As Young [40] points out, the covariance matrix for a non-linear model is not a constant as for a linear model. This has an implication on the numerical determination of the error of the fit parameters. Non-linearities in the fit function might also have an effect on the numerical minimization process of the χ^2 . However, finding the differences of the fitting process of the script `BinderFitVSmass.sh` and the PFG is not the goal of this section. It can just be observed, that overall, the results of both programs coincide well, but deviations are becoming worse for non-linear fit functions. Therefore, the user of the PFG is encouraged to pay attention, when using non-linear fit functions. Especially the generalized logistic and the Gompertz fit functions, which have not been compared to a different program yet, have to be used with care. A possible way to examine the obtained fit results within the PFG is changing the minimization algorithm in the Fit options tab of the PFG. Additionally, the initial values of the fit parameters can be altered to check, if the fit results are changing.

4. Locating the Heavy Z_2 -point

Having introduced the theoretical background in the first two chapters and having discussed the numerical methods to analyze a phase transition on the lattice, the presentation of the results from the simulations follows. This chapter is subdivided into four sections. In the first section, an overview over the simulations is given, including information on the simulation parameters and the statistics. The next section 4.2 reflects on the obtained kurtosis points and covers important aspects of obtaining the kurtosis values from the raw data. The crucial topic of how to find good fits from the numerous possible fits is subject of the next section 4.3, also focusing on the comparison of the different fit ansätze presented in section 3.1.6. Finally, results for the critical mass at the Z_2 point are presented in section 4.4, relating the results in lattice units to physical units.

4.1. Overview over the Simulations

All of the simulations, generating the Markov chains, were performed on the high performance computing GPU-cluster L-CSC using the lattice QCD code CL²QCD (see section 3.2.1). The executable `rhmc` was employed, generating trajectories according to the rooted staggered fermion action with two tastes. The temporal extent of the lattice is $N_\tau=8$, thus achieving a similar lattice spacing for all simulations. For the following simulation parameters, only the ranges are given, as the exact values can be seen in table 4.1. This table also lists the combinations of various parameters, for which simulations have been performed. For up to five different mass values in the range of $am \in \{0.35, 0.55, 0.75, 0.95, 1.15\}$, up to five different volumes have been simulated. The volumes are multiples of N_τ , leading to integer valued aspect ratios $\{4, 5, 6, 7, 8\}$. For most of the masses, the volumes $N_s \in \{32, 40, 48, 56\}$ have been simulated, but one larger volume $N_s=64$ in the vicinity of the expected Z_2 critical point has been added. For each of the simulated volumes, 2 to 5 β s around the critical value of β have been selected. The number of β values depends on the number of the needed guesses, to locate the critical β region, and on the computational cost of the particular simulation. Sometimes, additional β values have been inserted in the already existing range of the β s. This turned out to be necessary, if the reweighting (see section 3.1.3) performed too poorly, because of a just slim overlap of the histograms of the gauge actions. Subsequently, for each β , a number of 4 separate Markov chains with different seeds have been simulated. The number of the integrator steps of the 2MN integrator have been tuned to values, such that the acceptance rates are in a range of 80% to 90%. The submission and monitoring of the main part of the simulations were done by Alessandro Sciarra, only a few simulations for the volumes $N_s=56, 64$ have been taken over by the author.

The β values, which were simulated for certain combinations of masses and volumes, are shown in table 4.1. The cumulative number of trajectories is given next to the β

		masses am									
		0.35		0.55		0.75		0.95		1.15	
		β	traj.	β	traj.	β	traj.	β	traj.	β	traj.
volumes N_s	32	5.910	800 k	5.975	1200 k	6.005	1200 k	6.020	400 k		
		5.920	1200 k	5.980	1200 k	6.010	1200 k	6.025	800 k		
		5.930	1200 k	5.985	1200 k	6.015	1200 k	6.030	1200 k		
		5.940	800 k	5.990	1200 k	6.020	1200 k	6.035	800 k		
		-	-	-	-	-	-	6.040	400 k		
	40	5.914	1000 k	5.977	800 k	6.010	1000 k	6.022	400 k	6.035	1200 k
		5.920	1000 k	5.982	1000 k	6.014	1000 k	6.027	800 k	6.040	1200 k
		5.926	1000 k	5.987	1000 k	6.018	1000 k	6.032	800 k	6.045	1200 k
		5.932	1000 k	5.992	800 k	6.022	800 k	6.037	800 k	-	-
		-	-	-	-	-	-	6.042	400 k	-	-
	48	5.918	800 k	5.981	1200 k	6.009	1200 k	6.027	200 k	6.038	1200 k
		5.922	800 k	5.985	1200 k	6.012	1200 k	6.030	600 k	6.040	1200 k
		5.926	800 k	-	-	6.015	1200 k	6.033	600 k	6.042	1200 k
		-	-	-	-	6.018	1200 k	6.036	600 k	6.044	1200 k
	56	5.918	~760 k	5.981	1200 k	6.012	1200 k	6.030	1200 k	6.040	1200 k
		5.921	~760 k	5.983	~1090 k	6.015	1200 k	6.033	1000 k	6.042	1200 k
		5.924	~760 k	5.985	1200 k	-	-	-	-	6.044	1200 k
		-	-	-	-	-	-	-	-	6.046	1200 k
	64					6.011	~680 k				
						6.013	~650 k				
						6.015	~670 k				

Table 4.1.: Statistics and β values for the simulated combinations of masses am and volumes N_s . Since four Markov chains have been produced for one β , the number of trajectories (traj.), ($k = 10^3$), is the cumulative number. Cells with dashes indicate a lower number of β s, being simulated for this volume. Large empty cells correspond to combinations of volumes and masses, for which no simulations were performed. A \sim -sign signals, that these simulations are still running and that the number of trajectories is an approximate one.

value, with one fourth of these trajectories being accumulated for each Markov chain. A hard upper boundary of 300 k trajectories per chain (or 1200 k cumulative) had been set to stay within bearable limits of computational cost. Lower numbers of trajectories may result from the fact, that an acceptable error on the desired observables was reached early and a more precise measurement of the observables would not pay off in the overall context. This was the case especially for the smaller volumes, where, in general, smaller integrated auto-correlation times lead to a smaller error for the same amount of statistics. For the volumes $N_s=56, 64$, some simulations are still running at the moment, leading to a lower number of trajectories. These unfinished simulations can be recognized by a \sim -sign in front of the number of trajectories. This number is an approximate one and also the four different Markov chains differ in their number of trajectories, but the difference is not larger than a few thousand trajectories within one particular β . This shows, that the analysis presented here, is not final and these unfinished simulations require attention, when analyzing the kurtosis and performing the kurtosis fits, as discussed in the next sections.

Another important aspect is the thermalization process, consisting of two steps. The first step is called “thermalization from hot”, as the gauge links of the initial configuration are initialized randomly. After a certain number of thermalizing updates, the second step “thermalization from configuration” begins, where also a certain number of updates is performed. The “thermalization from hot” is only performed once (one Markov chain) for one particular combination of mass and volume at one of the possible β values. Thereafter, the “thermalization from configuration” is launched with the last configuration from before, however, this time several Markov chains are generated, each at the desired β value. Subsequently, the actual simulations for which the observables are measured are launched. For each β value, four Markov chains are submitted with different seeds. This procedure is chosen to reduce the computation time in comparison to each Markov chain, being thermalized on its own. A number of 1000 trajectories was chosen for the “thermalization from hot”. Combining this number with the 4000 trajectories for the “thermalization from configuration”, gives a total number of 5000 thermalizing steps for each Markov Chain. Just to be sure, the number of trajectories in table 4.1 does not include the thermalizing trajectories.

Finally, the simulations for the measurement of the pion mass and the scale setting are discussed. In principle, these simulations have to be performed at zero temperature. Consequently, the temporal lattice extent N_τ has to become large. Therefore, $N_\tau=32$ was chosen to meet the requirement of a large temporal extent. The number of spatial lattice points was chosen to be $N_s=16$. For each quark mass value, a pion mass and a lattice spacing at the critical β had to be found. The critical β was determined from the finite temperature simulations with the largest volume available to minimize the systematic error from finite size effects. If the accumulated statistics for the largest volume were not sufficiently large to determine a reliable critical β value, it was determined from the next smaller volume with a sufficient number of trajectories. For each mass value am , the thermalization was performed at the critical β as explained before. Again four different Markov chains with different seeds were set up for the generation of the configurations, which are used for the measurement of the pion mass. A total number of 10k trajectories per chain was accumulated, saving every 50-th configuration. In total, $200 \cdot 4 = 800$ configurations could be used to measure the pion mass and set the scale using the Wilson flow.

4.2. Discussion of the Obtained Kurtosis Points

The data can now be used to obtain a kurtosis value of the Polyakov loop at each combination of a mass and a volume by using the methods and concepts, discussed in section 3.1. Here, the details of those concepts are not repeated, but rather important aspects are pointed out on exemplary data.

First, it has to be checked, whether a sufficient amount of statistics has been accumulated for the analysis of both observables skewness and kurtosis of the Polyakov loop. A way to obtain an impression is considering the histograms of the Polyakov loop. It can be estimated qualitatively by eye, if the accumulated statistics might fulfill the requirement of smooth curves in the histograms. Additionally, it gives a first qualitative insight about the type of the phase transition.

Following [34], two more quantitative ways to evaluate the amount of the accumulated

β	chain	traj.	$B_3(\beta)$	events	$B_4(\beta)$	events
5.981	merged	1200 k	0.34(12)	138	1.95(5)	294
	1	300 k	0.4(3)	33	2.17(13)	74
	2	300 k	0.00(26)	32	1.75(8)	96
	3	300 k	0.26(21)	48	1.84(8)	122
	4	300 k	0.75(24)	40	2.47(17)	55
5.983	merged	~ 1090 k	-0.24(13)	120	1.95(5)	237
	1	~ 267 k	-0.09(29)	30	1.87(9)	84
	2	~ 272 k	-0.41(24)	44	2.16(11)	85
	3	~ 277 k	-0.30(24)	38	1.98(9)	85
	4	~ 277 k	-0.24(27)	30	1.87(10)	64
5.985	merged	1200 k	-1.20(13)	121	3.91(17)	133
	1	300 k	-1.3(3)	18	4.1(5)	19
	2	300 k	-1.37(20)	45	4.3(4)	45
	3	300 k	-1.02(25)	46	3.40(22)	53
	4	300 k	-1.0(4)	37	3.9(4)	40

Table 4.2.: The results for the jackknife analysis of the skewness and the kurtosis of the absolute value of the Polyakov loop from $am=0.55$ and $N_s=56$. First, the merged data and underneath, the data of the single chains is shown.

statistics are given here. First, the calculation of the integrated autocorrelation time τ_{int} for a particular observable determines the number of independent events in one Markov chain. If N is the total number of trajectories,

$$M = \frac{N}{2\tau_{int}} \quad (4.1)$$

is the number of independent events for binning $2\tau_{int}$ data. Note, that some data has to be discarded in the most cases, as the number of data in every bin has to be the same. In general, τ_{int} is larger for a system in the vicinity of a first order phase transition. The Markov chain has to tunnel between the two distinct phases to explore all regions of the phase space. The gap between the two phases prevents frequent tunneling between the phases, leading to a comparatively large τ_{int} . For finite volumes, the phases are smeared, but in general, larger volumes lead to an increasing τ_{int} . At a critical point, where the correlation length diverges, another phenomenon leads to the increase of the integrated autocorrelation time. As the correlation length cannot exceed the spatial length N_s of the system, the relation $\tau_{int} \propto L^z$ holds, where $z \geq 0$ is a dynamical critical exponent, depending on the Markov chain updating algorithm [17]. Nevertheless, the analysis has to be performed on the uncorrelated data, being reduced by τ_{int} . In this case, the jackknife analysis is applied, leading to a statistical error σ on the corresponding observable and Markov chain. The observables are the skewness and the kurtosis.

The second way to evaluate the amount of collected trajectories is considering the standard deviations σ for all four chains of one β . The number of standard deviations,

for which the most distinct chains are compatible, is defined as

$$n_\sigma = \max_{i < j} \left(\frac{|\langle O \rangle_i - \langle O \rangle_j|}{\sqrt{\sigma_i^2 + \sigma_j^2}} \right), \quad (4.2)$$

where $\langle O \rangle_i$ is the expectation value of the observable O for Markov chain i and σ_i is its statistical error. In [34], a maximum value $n_\sigma = 3$ and a minimum number of independent events M were used in combination to evaluate the amount of trajectories as sufficient. Subsequently, the chains are merged and τ_{int} is calculated to perform a jackknife analysis on the merged and binned data.

In table 4.2, the final analysis of the skewness and the kurtosis of the three different β s is displayed with its four chains, each for $am=0.55$ and $N_s=56$. Mostly, the number of independent events for single chains is larger than 30. The exceptions for the first chain of $\beta = 5.985$ have to be accepted, as already the upper boundary of the number of simulated trajectories is reached. However, it is beneficial to keep this in mind and to be careful, when performing the further analysis. The main implication is, that due to the few independent events, the error on the corresponding observable is presumably comparatively large. Obviously, the merged data provides a larger number of independent events, leading to smaller errors on the observables.

The results of the skewness and kurtosis in table 4.2 can also be seen in figure 4.1. The single chains are plotted on the left side and the merged chains on the right side. For the single chains plots, n_σ is given for each β . Usually, n_σ , being larger than 3, are not observed. For $\beta = 5.981$ a larger n_σ can be ascribed to smaller error bars, although the points are close. However, the upper limit of 300 k trajectories per chain has also been reached for this β , such that these points are accepted with care, as they are. As almost all single chains have been shown to be compatible with each other within a 3σ range, they are merged and the jackknife analysis is done again, obtaining the red points in figure 4.1 b) and d).

The next goal is to find β_c , where the skewness is zero and subsequently, to determine the kurtosis at β_c . As it is difficult to find these values considering only the points from the merged chains, the skewness and the kurtosis are reweighted, as explained in section 3.1.3. Beforehand, it is necessary to check, whether the overlap of the histograms of the gauge action for the merged chains is sufficiently large. If the simulated β values are too far apart, the reweighting becomes unreliable. This has been observed for $am=0.55$ and $N_s=56$, where initially, only the two outer β values (see figure 4.1) had been simulated. The simulation for the β value in between was launched later, having recognized, that the small overlap of the gauge action histograms leads to larger errors on the reweighted data in between the two outer β -values. As this region is particularly important for the localization of β_c and the determination of $B_4(\beta_c)$, the results of the reweighting have been improved by including the simulation at $\beta = 5.983$.

The reweighted skewness and kurtosis can be seen in figure 4.1 b) and d). The range, for which the observables were reweighted, was always set to $[\beta_{min}, \beta_{max}]$ of the available simulated β -values. The resolution of the new β values was set to 0.0001, which is sufficiently precise for the determination of β_c in relation to the statistical error. β_c is determined by finding the smallest absolute value of the skewness, as is implied by the dashed line in figure 4.1 b). Following the dashed line to the reweighted kurtosis, $B_4(\beta_c)$

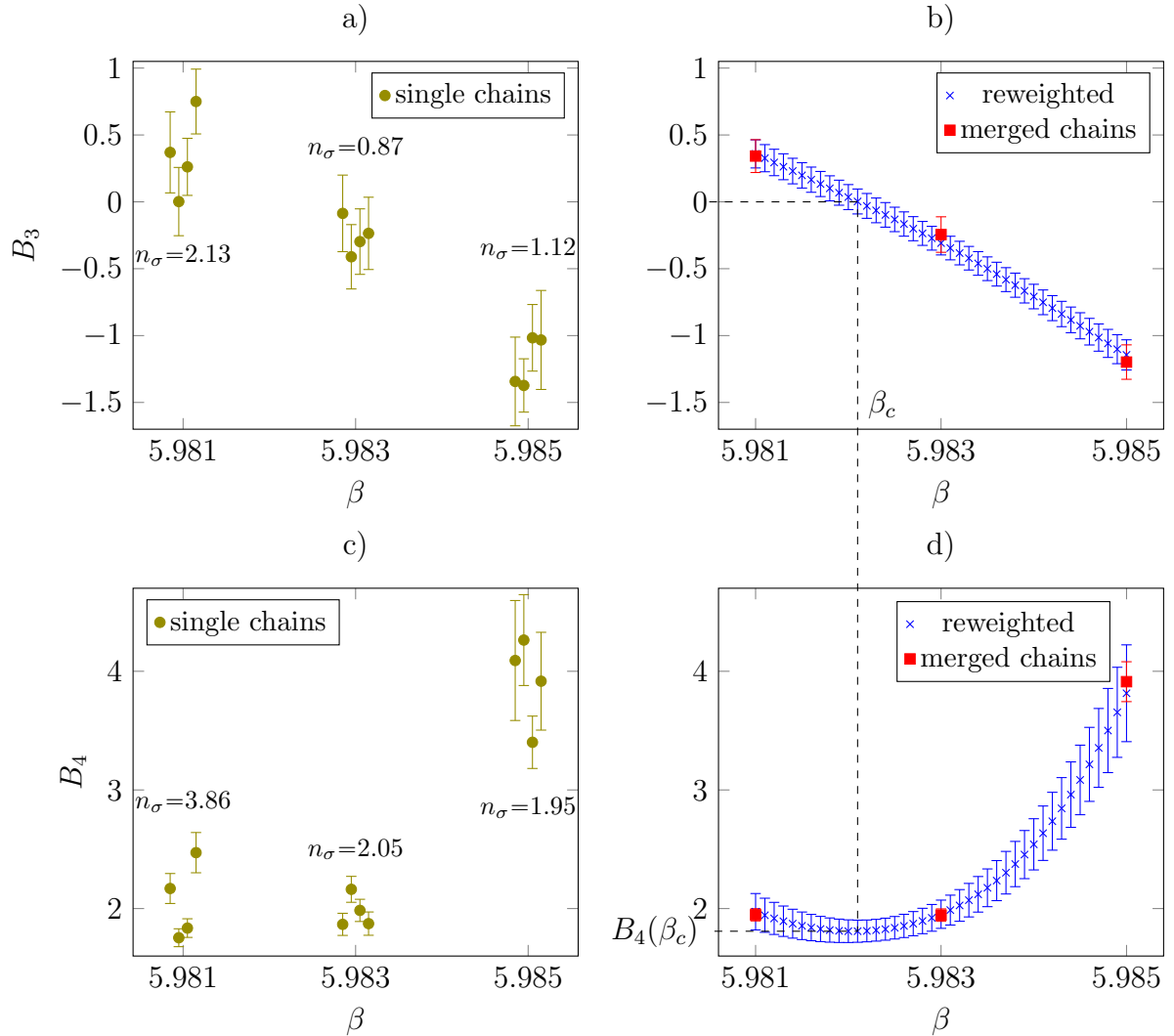


Figure 4.1.: Analysis and Reweighting of skewness B_3 and kurtosis B_4 of the Polyakov loop for $am=0.55$ and $N_s=56$. Skewness a) and kurtosis c) for single chains. Merged chains and reweighted skewness b) and kurtosis d). Values for the single chains are shifted horizontally for readability. For the single chains, n_σ is given. The dashed line indicates the extraction of β_c and $B_4(\beta_c)$.

can be determined. In principle, the zero crossing of the skewness should coincide with the minimum of the kurtosis. As locating a zero crossing is more precise than locating an extremum, always the skewness is used to determine β_c . Nevertheless, checking roughly, if β_c is located at the minimum of the reweighted kurtosis, is a good test of the reliability of the data in general and of the reweighted data.

All kurtosis values at β_c can be extracted, as described above, and afterwards gathered into one table, containing the columns mass, N_s , $B_4(\beta_c)$ and $\Delta B_4(\beta_c)$. This data table forms the basis for performing the kurtosis fits. The table is not shown here, as a plot of the kurtosis values versus the mass is more illustrative.

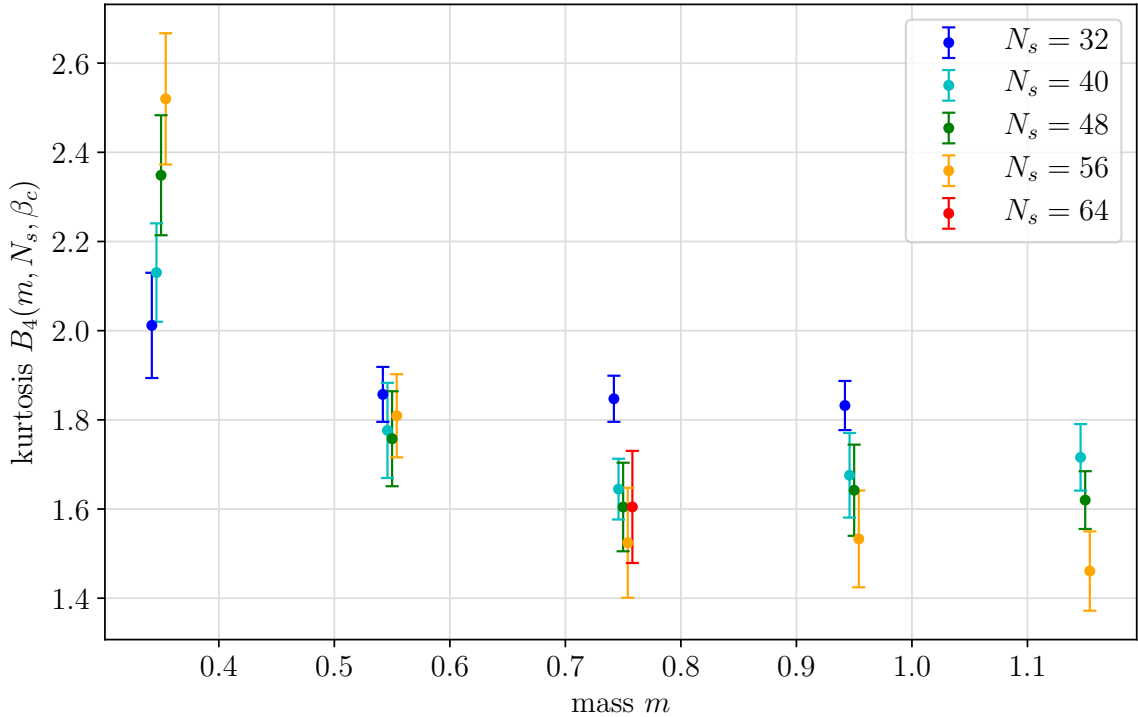


Figure 4.2.: The kurtosis values for different volumes N_s (different colors) as a function of the mass m . The points are shifted horizontally around the true mass value for better readability.

In figure 4.2, the bare quark mass m was chosen to represent the horizontal axis instead of the inverse quark mass $1/m$, which is preferred for the evaluation of the fits in section 4.3. The reason is the easier relation of the kurtosis points to table 4.1. In this plot and in the following plots, the mass m is always represented in lattice units. Figure 4.2 shows the kurtosis points for different volumes N_s with different colors. The orange point at mass $am=0.55$ was discussed above and some simulations for it are still running. Nevertheless, the analysis has shown, that this point can be accepted as reliable. The orange point for $am=0.35$ is more problematic in this sense, since currently, significantly less statistics have been accumulated. The condition $n_\sigma < 3$ is not always given and the reweighting of the kurtosis and the skewness shows small deviations from the expected course of both reweighted observables as a function of β . Therefore, this point has to be accepted with care and in case of doubt, has to be excluded from fitting. The only

other point, for which the simulations are still running, is the red one at $am=0.75$. This point is the most critical one, concerning the reliability, as neither the condition $n_\sigma < 3$ is fulfilled, nor the number of independent events is larger than 30 for most of the chains for skewness and kurtosis. With respect to the drift of the kurtosis points at $am=0.75$ for all volumes, a further decrease of the kurtosis value of the red $N_s=64$ point is expected. As this is not the case, the further investigation of this point with respect to the amount of statistics is motivated. Additionally, the irregular and noisy distributions of the histograms of the Polyakov loop for this point are an indicator for insufficient statistics. When including this point into the fits, the problematic nature of this point should definitely be remembered for the further analysis.

Overall, it is evident, that the kurtosis values decrease from smaller masses to larger masses. This behavior gets stronger for larger volumes N_s , as expected. The range of the kurtosis values coincides with the expected one. The upper value 3, coming from the crossover is not exceeded and no point is located below 1, which corresponds to the first order phase transition. First deductions about the range of the critical mass can be derived from the order of the points of different volumes at one particular mass. Considering the smallest mass value $am=0.35$, the order, that smaller volumes correspond to smaller kurtosis values and larger volumes correspond to larger kurtosis values, indicates a crossover. A similar argument applies, at least for the two largest masses 0.95 and 1.15, being in the first order region. These observations can be supported by the shapes of the histograms of the Polyakov loop, which are evaluated qualitatively by eye. For masses in the crossover region, only a single peak of the histogram, shifting with varying β , can be identified. On the opposite, the histograms in the first order region show two peaks, although they are not separated by a clear gap. Constructing a range for possible critical mass values helps a lot, when fitting to the kurtosis data, as will be seen in the next section 4.3.

4.3. Finding Good Fits

The main problem of finding good fits, which give the critical mass as a fit parameter, is the large amount of possible fits. One reason for this problem is the number of possible kurtosis fit functions. In section 3.1.6, some of them were presented. Additionally, the selection of kurtosis points from figure 4.2, being included in the fit, can be varied, thus giving yet many more possible fits. Therefore, it is important to find strategies to limit the number of possible fits, however, keeping the good ones. Basically, the term *good fit* relies on the quality measurements Q and χ_{ndf}^2 of the fit introduced in section 3.1.6. The number of possible fits can be reduced by raising constraints to the fit. This mainly concerns the fit parameters, as is discussed in section 4.3.1. Moreover, the different fit ansätze can be compared to each other under general aspects to exclude some of them. Among other things, this will be subject of section 4.3.2.

4.3.1. Discussion of the Constraints to the Fits

General reflections on the data can lead to constraints of the fit parameters. The most important fit parameter is the critical mass m_c . As already mentioned in section 4.2, the rough range of the critical mass m_c can be deduced from the kurtosis data. As the PFG

allows to set boundaries for the fit parameters, this can be used to narrow the search for a good fit. Independently of the used fit function, the critical mass can be constrained to the range $am_c \in [0.35, 0.95]$. If the optimization algorithm of the PFG hits a boundary for the result of one of the fit parameters, the PFG gives a warning. Indeed, this result cannot be taken as a valid fit, because it does not represent a local minimum of the χ^2 . Therefore, it is useful to always choose broader boundaries than actually required. A fit, for which one of the fit parameters reaches the boundary, has to be discarded.

Constraints can also be set up for the other fit parameters. However, the constraints of the fit parameters depend on the chosen fit function. In the following, only some general constraints of fit functions are discussed. The discussion of the various fit ansätze in the next section 4.3.2 includes some explicit boundaries for the fit parameters. The most important constraint is, that the fit function, depending on the scaling variable $x = (1/m - 1/m_c)N_s^{1/\nu}$, has to be monotonically increasing. This implies constraints to the fit parameters. For example, the linear fit function of the form $f(x) = a_1x + a_0$ leads to a strictly positive a_1 . An additional cubic term a_3x would impose the constraint, that a_3 is also strictly positive. Especially, for the more complicated fit functions Gompertz and generalized logistic function, also mathematical constraints on the fit parameters have to be considered. Singularities must not be possible to occur in the fit function. The particular cases are discussed in appendix B, where the general functions are adjusted for the fitting to the kurtosis.

Some constraints on the selection of the kurtosis points, being included in the fits, can be required. Following the discussion in section 4.2, the unreliable points can be excluded from the fits. Arguments like large finite size effects can count to exclude smaller volumes. Excluding masses, which are far apart from the expected critical mass, can be reasonable. One reason may be the universal scaling, only applying for the close region around a critical point. Considering the linear fit from above, the linear approximation, which is best close to $x = 0$, can justify an exclusion of data points far from the expected critical mass. To clarify, it is not useful to randomly exclude or include points into the fits. One reason is the missing physical or mathematical motivation to justify the decision. Hence, overfitting issues might easily appear, where the fit is accidentally good, but does not correspond to the real situation. Secondly, there are just too many possibilities of subsets of the kurtosis points, for which fits have to be performed. The number of possible fits can be narrowed further by analyzing the different fit ansätze in the following.

4.3.2. Analysis of the Different Fit Ansätze

An overview over all discussed fit ansätze is given here. An overall principle states, that good fits should get along with as few fit parameters as possible. The correction term can be applied for all fit ansätze, so its discussion is postponed to the end, when a better understanding of the basic fit ansätze has been developed. First, there is the polynomial fit function, where terms with larger orders of the scaling variable do not have to be excluded from the beginning. Furthermore, there is the generalized logistic fit, still being problematic with respect to the numerical fitting with `curve_fit` from `scipy`. Due to the high non-linearity and the parameter a or q , appearing twice in formula (3.55), the fit results become unstable with respect to varying initial values for the fit parameters. Especially the errors on the fit parameters a or q seem to be determined incorrectly, as they are either very large or very small. This problem has not been solved yet and

therefore, the generalized logistic fit is excluded from the discussion here. This is also motivated by the availability of a different fit function with similar properties concerning the shape of the curve, namely the Gompertz fit function. The problems from above do not occur there and it can be analyzed, how the kurtosis fit analysis benefits from fit functions with two asymptotes.

Although implications of the correction term on the results of the fit have not been discussed, the analysis of the polynomial fits will always include the correction term. The reason is, that the usage of the correction term allows to include also the data points for the smallest volumes $N_s=32, 40$ to obtain good fit results. This observation will be analyzed later in more detail, but already here it is used for a general discussion of the different polynomial fit ansätze. The red point $am=0.75$, $N_s=64$ from figure 4.2 is always excluded in this analysis to avoid any unwanted impact of this comparatively unreliable point on the outcome of the fits.

am_c	a_1	a_2	a_3	b	ndf	χ_{ndf}^2	Q
0.62(6)	$6.2(8) \cdot 10^{-4}$	-	-	3.7(7)	16	0.9709	48.59%
0.54(6)	$6.6(1.0) \cdot 10^{-4}$	$5.0(2.2) \cdot 10^{-7}$	-	4.0(8)	15	0.6005	87.71%
0.62(4)	$3.7(1.5) \cdot 10^{-4}$	-	$1.2(6) \cdot 10^{-9}$	3.4(4)	15	0.6052	87.34%
0.50(7)	$5.2(2.0) \cdot 10^{-4}$	$9(7) \cdot 10^{-7}$	$1.1(7) \cdot 10^{-9}$	4.0(7)	14	0.4483	95.90%

Table 4.3.: Fit results for the linear (1st row), quadratic (2nd), cubic (3rd) and quadratic + cubic (4th) fit with correction according to equation (4.3). - indicates a non-existing fit parameter.

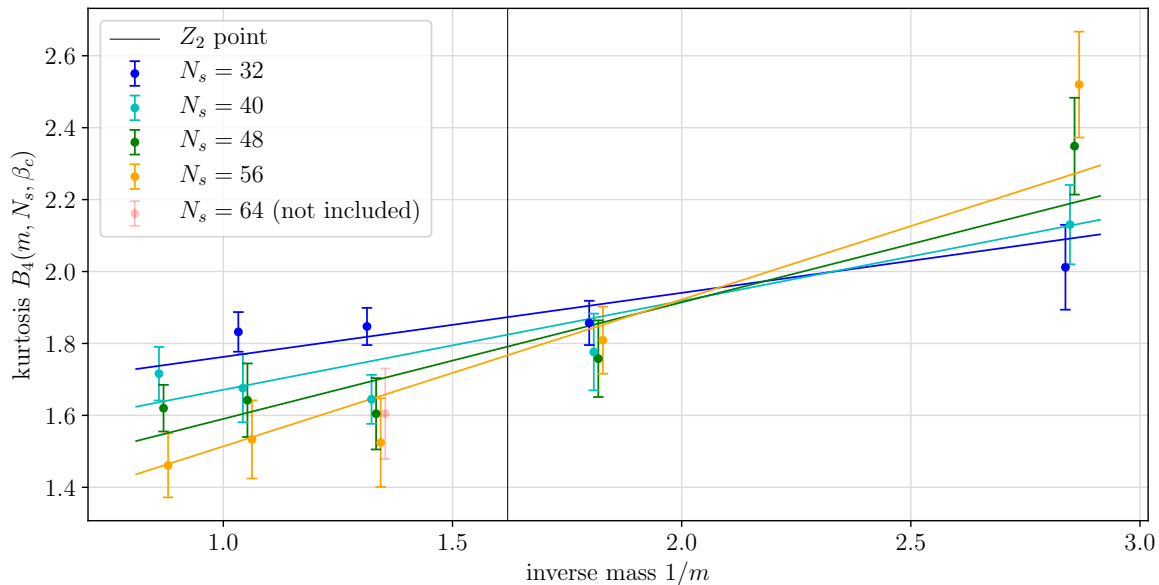
The discussion is restricted to the polynomial fit function of the form

$$B_4(x, N_s) = \left(B_4(\infty, Z_2) + \sum_{n=1}^3 a_n x^n \right) \cdot (1 + b N_s^{y_t - y_h}), \quad (4.3)$$

see also equation (3.51), where $x = \left(\frac{1}{m} - \frac{1}{m_c} \right) \cdot N_s^{1/\nu}$ is the scaling variable (m_c, m in lattice units). It is decided to only discuss powers of the scaling variable up to three, thus having a linear, a quadratic and a cubic term. These may be combined arbitrarily, but there is no good reason to exclude the linear term. Thus, four combinations, whose results can be seen in table 4.3, are discussed.

The corresponding plots of the fits are shown in figures 4.3 - 4.5. The last plot for the cubic + quadratic fit is not shown here, as it does not contain qualitatively new information. For the linear fit, the χ_{ndf}^2 and the Q parameter are good, as they are close to the optimal values 0.5 and 50%, respectively. However, for the smallest mass on the right of figure 4.3, the fit does not hit the two points of the larger volumes very well. This can be traced back to their larger error bars and therefore the lower impact on the fit in general. It can also be argued, that the small masses (1 on the right) are less represented than the large masses (2 to 3 on the left). This may lead to a fit function, that mainly fits to the points of large masses and only weakly to the points in the small mass region.

When considering the quadratic fit (see figure 4.4), the points of small masses are hit better by the fit. On the other hand, the χ_{ndf}^2 decreases significantly, which can not be attributed to the smaller number of degrees of freedom $ndf = 15$, instead of $ndf = 16$. The Q parameter $Q = 87.71\%$ also indicates an overfitting of this fit ansatz. Another



am_c	a_1	b	ndf	χ_{ndf}^2	Q
0.62(6)	$6.2(8) \cdot 10^{-4}$	3.7(7)	16	0.9709	48.59%

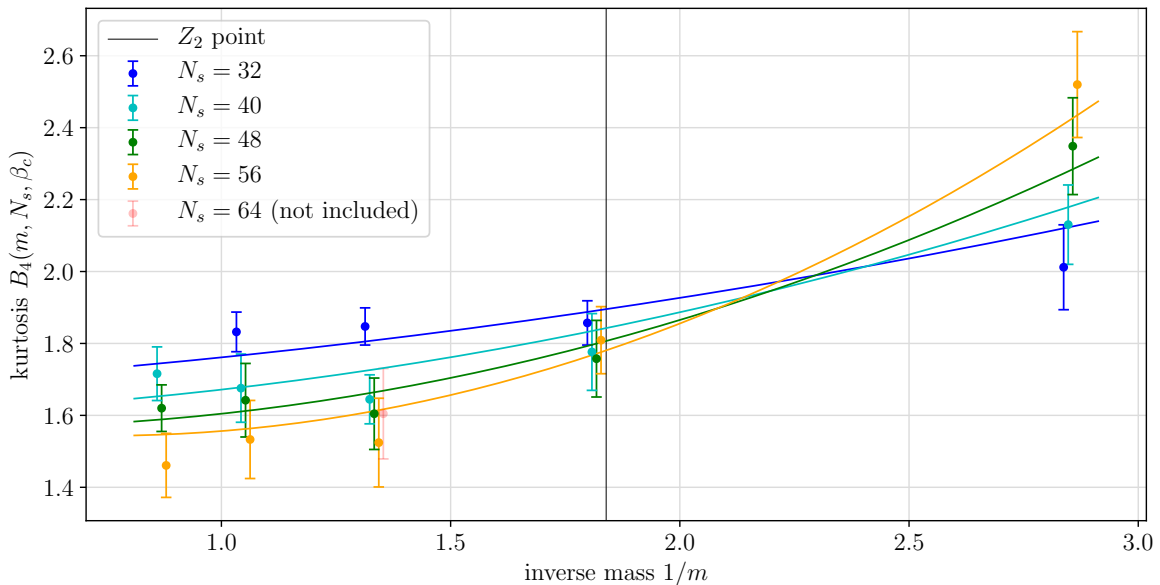
Figure 4.3.: Linear kurtosis fit with correction according to equation (4.3). The kurtosis points are shifted horizontally around their mass value for readability.

problem arises, when considering, that a quadratic fit function is not monotonically increasing, although for the relevant domain (see figure 4.4) it is. In any case, quadratic fits should be treated with care.

The polynomial fit with linear and cubic term also shows the properties of a small χ_{ndf}^2 and a Q parameter close to 90%. The same arguments of the overfitting apply here as well. Additionally, the shape of the cubic fit contradicts the expected shape of the kurtosis from figure 3.3 qualitatively. Figure 4.5 shows, that the fit function tends towards ∞ or $-\infty$ for large scaling variables x or $-x$, respectively. The expected behavior of the fit function in the large or small mass limit should be an approaching of two different constant asymptotes. Another aspect related to the shape of the fit function is the slope near the critical mass. A value of the slope for small x close to the maximum is expected for the model displayed in figure 3.3. This is contradicted by the shape of the cubic fit function, for which the slope is minimal at the critical mass.

The last combination of linear, quadratic and cubic terms in the polynomial fit function does not lead to a qualitatively different shape of the function, compared to the cubic fit function. However, considering the fit results in the last row of table 4.3 gives some new insights. The χ_{ndf}^2 is decreasing to 0.4483 and the Q parameter approaches 100%. This confirms the observation, that, using more terms in the polynomial fit results in heavier overfitting effects. In the end, this justifies the decision to only discuss the lower orders of the polynomial fit function. Additionally, the fit parameters a_2 and a_3 become less relevant, as the magnitude of the value and its error are the same.

The discussion of the polynomial fit leads to the conclusion, that for fitting the kurtosis in this particular mass range, only the linear term should be considered for the polynomial fit function. There, it can be assumed, that overfitting does not play an important role



m_c	a_1	a_2	b	ndf	χ_{ndf}^2	Q
0.54(6)	$6.6(1.0) \cdot 10^{-4}$	$5.0(2.2) \cdot 10^{-7}$	4.0(8)	15	0.6005	87.71%

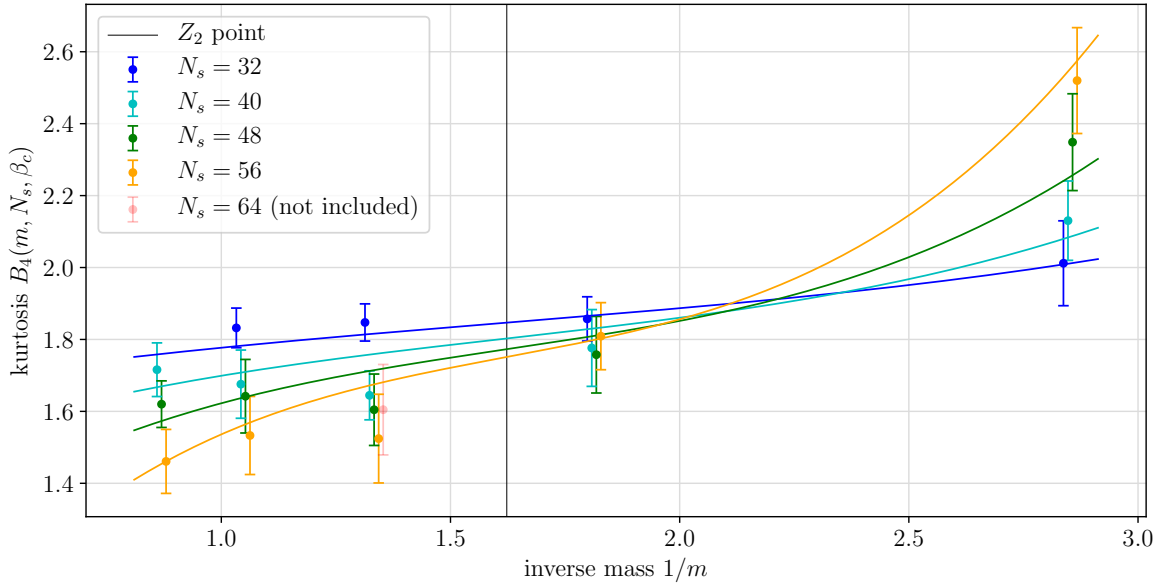
Figure 4.4.: Quadratic kurtosis fit with correction according to equation (4.3). The kurtosis points are shifted horizontally around their mass value for readability.

and the linear shape of the function does not raise explicit contradictions to the expected shape of the kurtosis. From now on, only the linear fit function will be subject of the discussion, for example, when comparing it to the Gompertz fit function.

The Gompertz fit function is recalled for convenience from equation (3.57)

$$F_G(x) = B_4(1.O, \infty) + (B_4(CO, \infty) - B_4(1.O, \infty)) \exp \left(-\frac{\ln \left(\frac{B_4(CO, \infty) - B_4(1.O, \infty)}{B_4(Z_2, \infty) - B_4(1.O, \infty)} \right)}{\exp(sx)} \right). \quad (4.4)$$

In its flipped version, s is replaced with $-s$ and the constants $B(1.O, \infty)$ and $B(CO, \infty)$ are exchanged, wherever they appear. The Gompertz fit with correction term is performed on the same kurtosis data set as the polynomial fits before for comparability. The fit results can be seen in table 4.4 and for both types, the fit parameters am_c and b coincide with each other within the error bars. However, they also coincide with the results of the fit parameters from the linear fit with correction from table 4.3. Another observation is the small growth rate parameter of the Gompertz fit s . Thus, for mass values close to am_c , a straight line is a good approximation for the Gompertz function. This conclusion can also be drawn from the plots of both types of the Gompertz fit in figures 4.6 - 4.7. There, only a weak curvature of the lines is apparent. The flipped Gompertz fit function shows a larger curvature than the normal one, but it is still weak. This difference can be explained by recalling, that the two types of the Gompertz fit approach the two asymptotes at different speed. The flipped type also models the kurtosis points at the smallest mass and the larger volumes more accurately than the normal type, which is similar in its behavior to the linear fit. The χ_{ndf}^2 and the Q parameter, on



am_c	a_1	a_3	b	ndf	χ^2_{ndf}	Q
0.62(4)	$3.7(1.5) \cdot 10^{-4}$	$1.2(6) \cdot 10^{-9}$	3.4(4)	15	0.6052	87.34%

Figure 4.5.: Cubic kurtosis fit with correction according to equation (4.3). The kurtosis points are shifted horizontally around their mass value for readability.

the other hand, are significantly better for the normal type of the Gompertz fit, as they approach the optimal values 1 and 50%, respectively.

type	am_c	s	b	ndf	χ^2_{ndf}	Q
flipped	0.57(6)	$-0.00127(14)$	4.0(7)	16	0.6833	81.36%
normal	0.60(6)	$-8.7(1.1) \cdot 10^{-4}$	3.9(7)	16	0.9369	52.53%

Table 4.4.: Fit results for two Gompertz fits with correction according to equation (4.4).

Overall, the Gompertz fit is well suited to fit this type of data, but it does not have that many advantages over the linear fit at this point. An explanation can be the range of the simulated masses, being sufficiently close to m_c , to stay in the linear region for these volumes. When considering simulations for broader mass ranges or if larger volumes are available, the Gompertz fit might outperform the linear fit. This statement has yet to be confirmed by testing the Gompertz fit on different data sets.

The last point in this section is the evaluation of the impact of the correction term on fit results, especially the critical mass am_c . The multiplicative correction term has the form $(1 + bN_s^{y_t - y_h})$ and as $y_t - y_h$ is a negative number, it is expected, that it becomes irrelevant for fits with sufficiently large volumes. Thus, both, the linear fit and the linear fit with correction, are examined for their behavior, when excluding the smaller volumes. As still the only point for volume $N_s=64$ is excluded, the two largest volumes $N_s=56, 48$ remain. They can not be excluded to prevent an insufficient number of degrees of freedom and overfitting. The linear fit without correction does not lead to good fit results for the largest set of data points. Additionally, the critical mass is not in the expected range $am_c \in [0.35, 0.95]$. Therefore, this fit is not presented in table 4.5. A plot of the linear

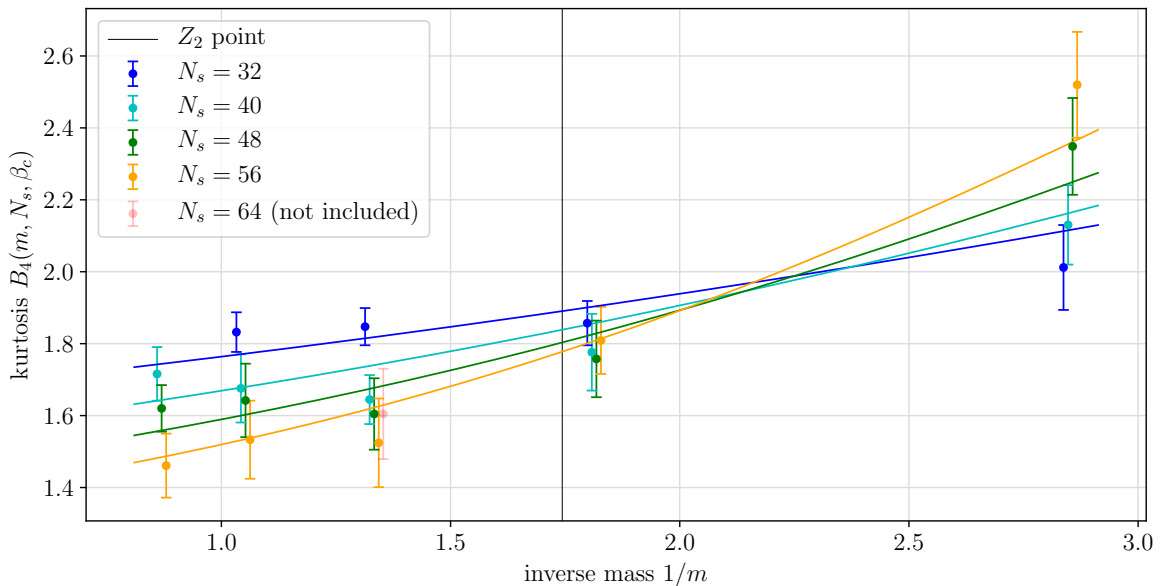


Figure 4.6.: Flipped Gompertz kurtosis fit with correction according to equation (4.4). The kurtosis points are shifted horizontally around their mass value for readability.

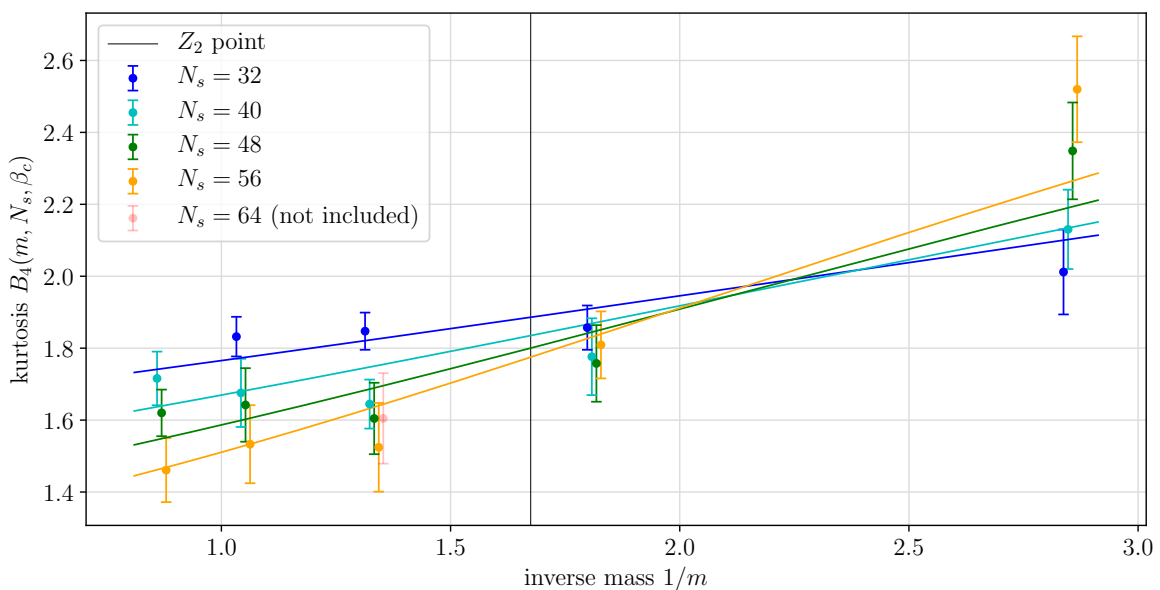
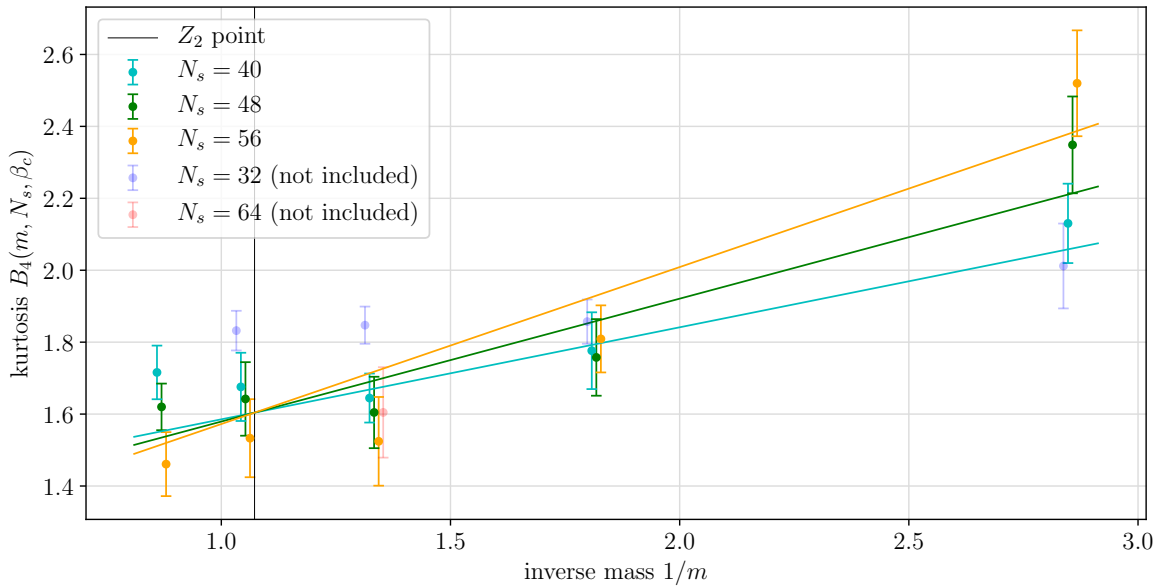


Figure 4.7.: Normal Gompertz kurtosis fit with correction according to equation (4.4). The kurtosis points are shifted horizontally around their mass value for readability.

fit number	N_s	am_c	a_1	b	ndf	χ_{ndf}^2	Q
1	56, 48	0.57(14)	$6.7(1.0) \cdot 10^{-4}$	5(4)	7	1.0669	38.18%
2	56, 48, 40	0.67(10)	$6.8(8) \cdot 10^{-4}$	2.9(1.5)	12	1.0296	41.76%
3	56, 48, 40, 32	0.62(6)	$6.2(8) \cdot 10^{-4}$	3.7(7)	16	0.9709	48.59%
4	56, 48	0.87(6)	$7.7(1.0) \cdot 10^{-4}$	-	8	1.2054	29.10%
5	56, 48, 40	0.93(7)	$7.3(9) \cdot 10^{-4}$	-	13	1.2603	22.90%

Table 4.5.: Fit results from the linear fit with and without correction for different inclusions of the largest simulated volumes N_s .

fit without correction has been already seen in figure 4.3 and as an example for a linear fit without correction, figure 4.8, including the three largest volumes, is shown.



am_c	a_1	ndf	χ_{ndf}^2	Q
0.93(7)	$7.3(9) \cdot 10^{-4}$	13	1.2603	22.90%

Figure 4.8.: Linear kurtosis fit without correction, including the three largest volumes. The kurtosis points are shifted horizontally around their mass value for readability.

The fit parameters m_c and b , being relevant for this examination, can be plotted in a stability plot. This implies the am_c - and b -column of table 4.5, being plotted as a function of the fit number, allowing a better understanding of the behavior of these important parameters for excluding smaller volumes and fitting with and without the correction term.

The stability plot can be seen in figure 4.9. Considering only the critical mass, the values for am_c are compatible for the fits with correction (1 - 3) and for the fits without correction (4 - 5), each. Hence, the two different fit ansätze lead to critical masses in different regions. The fits with the correction term occupy the close region around $am_c = 0.6$, whereas the fits without correction occupy the region around $am_c = 0.9$. The fit parameter b does not change much, when including smaller volumes, but it gets more

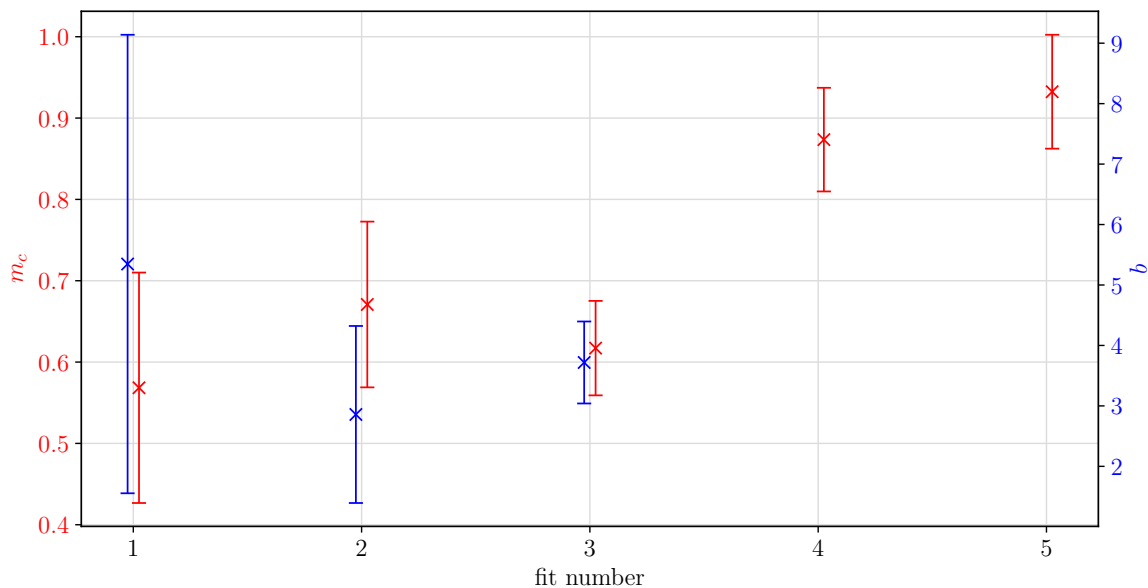


Figure 4.9.: Stability plot of the critical mass m_c (in lattice units) and the correction term parameter b corresponding to the data in table 4.5.

constrained as the error becomes smaller. This is the expected behavior as b obtains larger weight in $(1 + bN_s^{y_t - y_h})$, if smaller volumes are included. Hence, the variation of this fit parameter has a larger effect on the fit.

Two main conclusions can be drawn from these observations. First, the correction term is still relevant for large volumes $N_s=56, 48$. This is supported qualitatively by the plot of the linear fit with correction term in figure 4.3. The crossing points of adjacent volumes shifts down and to the left, getting closer to the Z_2 point. For example, the crossing point of the two smallest volumes $N_s=32, 40$ (blue, cyan) is at approximately $B_4 = 2.0$ and the crossing point of the two largest volumes $N_s=48, 56$ (green, orange) is at approximately $B_4 = 1.88$. This is still far from the crossing point, which can be seen in figure 4.8 at the kurtosis value $B_4(\infty, Z_2) = 1.604$. Fits with correction term will approach this crossing point for pairwise increasing volumes. One consequence of the crossing point in figure 4.8, being forced down to the $B_4(Z_2, \infty) = 1.604$ line, is believed to be the shift to larger masses. According to the fit, all the kurtosis points at the critical mass should fall together, but as can be seen in figure 4.8, this is presumably not the case. Additional quantitative support to this first conclusion comes from the χ_{ndf}^2 and the Q parameter of the fits. Referring to table 4.5, the fits with correction have a significantly better χ_{ndf}^2 and Q .

The second important conclusion only concerns the fits with correction. The exclusion of small volumes leads to larger errors on the fit parameters, especially on the one related to the correction term parameter b . Thus, the use of the correction term is not advised for large volumes only, although it has been shown in the previous paragraph, that the correction term is still relevant for large volumes.

The example fits discussed here are the most illustrative ones, but other fits with different selections of data points, not being shown here, support the conclusions from above. Having reflected on the different ways to obtain a good fit, now, the focus is on

obtaining an actual value for the critical mass and relating it to physical units in the next section.

4.4. Obtaining a Critical Mass

As there is no definite quantitative procedure to select the best fit and its value for am_c , here the arguments are weighed qualitatively, leading to a particular final critical mass. This value is related to physical values and the other simulation parameters are given in physical units as well. Subsequently, it is inevitable to lead a discussion about the finite size effects and the lattice artifacts, that have to be taken into account.

In the previous section many possible fit ansätze and also the corresponding subsets of kurtosis points have been ruled out, leaving the decision between a linear fit and a linear fit with correction. An argument, that would favor the linear fit, is the basic principle, that a fit should be as parsimonious as possible, meaning that the number of fit parameters should be minimized. This increases the chance, that the fit truly models the real situation, instead of just fitting to the sample of the data, on which the fit was performed. On the other hand, as many kurtosis points as possible should be included into the fits. This increases the chance, that biases from single kurtosis points due to statistical errors or even locally limited systematic errors are averaged out in the fit result. As shown in the previous section 4.3, the linear fit only gives a reasonably good result, when excluding many kurtosis points for smaller volumes, whereas the linear fit with correction allows to include all points of all volumes $N_s=32, 40, 48, 56$. Finally, the choice of the linear fit with correction is confirmed by the fit quality. These quantitative measures of the quality are that close to optimal, that this fit seems to be unaffected by overfitting, even when considering the additional fit parameter b . As a preliminary result for the critical quark mass in lattice units, the critical mass from the linear fit with the correction term

$$am_c = 0.62(6) \tag{4.5}$$

from fit number 3 in table 4.5 and in figure 4.3 is quoted here. It is preliminary, because some simulations, as shown in section 4.1, are still running and the result of the fit parameters will possibly change. The relative error of the critical mass with $\sim 10\%$ is still large, but its magnitude is comparable to or even smaller than the errors of am_c for other fits. Indeed, this error reflects the uncertainty of the fit with respect to am_c , which becomes apparent in the stability plot in figure 4.9. The quoted result stems from fit number 3 and exclusion of some more kurtosis points, as it was done for fit numbers 1 and 2, leads to a varying critical mass. However, the fits 1 and 2 are roughly compatible with fit number 3 within one sigma range. A safe way to try to reduce the error of am_c is collection of more statistics. In that case, the kurtosis points in figure 4.2 attain smaller errors, leading to a more powerful constraint of the fits. However, it is dubious if the huge additional computational cost is worthwhile, as the errors decrease proportional to $1/\sqrt{N}$, with N being the total amount of statistics. Especially for larger volumes, where the integrated autocorrelation time is large anyway and the computational time per trajectory is enormous, it is difficult to reduce the error bars of the kurtosis points.

To relate the $am_c = 0.62$ value to physical masses the pion mass is calculated and the scale is set by determining the lattice spacing, as described in 1.5. The simulation parameters are chosen, as explained in the end of section 4.1, thus arriving at physical

am	β_c	am_π	a {fm}	m_π {GeV}	T_c {MeV}
0.35	5.9215	1.40001(10)	0.0906(10)	3.05(3)	272.3(2.9)
0.55	5.9821	1.72039(7)	0.0888(10)	3.82(4)	278(3)
0.75	6.0129	1.98121(7)	0.0872(9)	4.48(5)	283(3)
0.95	6.0305	2.20857(6)	0.0871(9)	5.00(5)	283(3)
1.15	6.0411	2.41361(5)	0.0874(9)	5.45(6)	282(3)

Table 4.6.: Results from the pion mass measurement and the scale setting together with the critical β and the corresponding critical temperature T_c .

values at each am and β_c . The results can be seen in table 4.6. Currently, no physical values for the critical mass m_c have been determined, but for a qualitative classification of this result the values in table 4.6 suffice. When performing the continuum limit, an exact physical value of m_c is necessary, but this calculation can be performed, as required. In this case, the critical β is interpolated to the critical mass value, where the computationally cheap pion mass calculation is performed, as for the other masses. This calculation is postponed, until final results for (4.5) are obtained.

The pion masses in lattice units am_π in table 4.6 show, that, for all simulated bare quark masses, large lattice artifacts have to be expected. The inverse pion mass $1/m_\pi$ can be interpreted as the Compton wavelength. For these simulations, $am_\pi > 1$ means, that the lattice does not resolve the pion for any simulation, as its spatial extent is smaller than the lattice spacing. This clarifies once more the necessity to perform simulations closer to the continuum limit, implying $N_\tau > 8$. This will increase the computational costs, as the spatial extent of the lattice N_s has to grow with N_τ to keep the aspect ratios N_s/N_τ constant. This is mandatory to keep the physical volumes constant, allowing a comparison of the finite size effects for different N_τ .

N_τ	$m_\pi^{Z_2}$ {GeV}
6	5.01(5)
8	4.51(5)
10	4.39(5)

Table 4.7.: The results of $m_\pi^{Z_2}$ for various $a(T_c)$. The relative difference of the smallest and the largest lattice spacing amounts

Another observation is the increase of the lattice spacing for smaller masses. The reason is the decrease of the critical temperature with decreasing bare quark mass. As N_τ is kept constant, the equation $T_c = 1/(a(T_c)N_\tau)$ leads to an increase of the lattice spacing to approximately 4%. Following [14] this effect

might explain different finite size effects for different masses, as the physical volume is smaller for large masses. Indeed, the kurtosis points for the large masses seem to decrease more slowly than for the small masses (see e.g. figure 4.3). In contrast to [14], where this relative deviation of physical volumes amounts to up to 19%, the 4% in this case seem to be negligible. This statement is supported by the observation, that the asymmetry of the kurtosis around its Z_2 inflection point at the critical mass seems to contribute much more to the slower decrease of kurtosis values at large masses.

As expected, the physical value of the pion mass, which is approximately $m_\pi^{phys.} \approx 140$ MeV, is far from the simulated region $m_\pi \in \sim [3, 5]$ GeV. However, it is more useful to compare this result to other lattice calculations for the $N_f=2$ heavy Z_2 point. A project, also investigating the heavy Z_2 point using $N_f=2$ Wilson fermions on $N_\tau=8$ lattices,

showed, that the range of the pion mass is $m_\pi \in [2904(17), 4690(28)]\text{MeV}$ at the heavy Z_2 point [14]. Qualitatively, this is in good agreement with the result obtained here. The project from [14] was recently continued by additionally searching the Z_2 point on $N_\tau \in \{6, 8, 10\}$ lattices [12]. There, the obtained values for the critical point were given as precise pion mass values, allowing a more quantitative comparison with the result obtained here. The critical pion masses from Wilson fermions can be found in table 4.7. The result for $N_\tau=8$ Wilson fermions is in good agreement with the critical pion mass for $N_\tau=8$ staggered fermions, which presumably is in the range of $m_\pi^{Z_2} \in [3.82, 4.48]\text{GeV}$. Yet, the finalization of the currently running simulations has to be awaited. In addition, a comparison with the data from table 4.7, including the other N_τ would be of great interest, as this might give hints, on how the staggered and Wilson formulation affect the behavior of the critical mass towards the continuum limit. Subsequently, the shift to a smaller critical pion mass for a smaller lattice spacing, which can be observed in table 4.7, could also be examined for staggered fermions.

Summary and Conclusion

The goal of this study was to locate the heavy Z_2 point for $N_f=2$ lattice QCD in the staggered fermion discretization at $\mu=0$. To prepare the discussion of phase transitions in lattice QCD and their analysis, the theoretical basis for lattice QCD was presented in the first chapter. Especially the role of the center symmetry of pure gauge theory for the deconfinement transition is pointed out. The Polyakov loop was introduced as an approximate order parameter of the deconfinement transition also for lattice QCD with dynamical quarks. The second chapter is devoted to the discussion of the QCD phase diagram and its relation to the Columbia plot, but beforehand phase transitions, particularly on finite lattices, were discussed more broadly. The finite size scaling analysis of the reduced free energy density was shown, which plays a crucial part in the derivation of a finite size scaling formula of the kurtosis in chapter 3. There, the details of the analysis of observables are outlined, after which the determination of the critical inverse gauge coupling β_c by the skewness is shown. The meaning of the kurtosis value at β_c for the type of the phase transition is given for the cases of a crossover, a first order phase transition and a Z_2 second order phase transition. Next, various fit ansätze for the finite size scaling formula of the kurtosis are presented. This large chapter 3 concludes with the description of some important numerical tools and particularly the presentation of the fitting program PFG, which was newly implemented as part of this master's thesis.

The last chapter discusses the results from the analysis of the skewness and the kurtosis of the Polyakov loop. Various fit ansätze are analyzed on the available data and evaluated with respect to their quality. Some important conclusions can be drawn from this analysis. Using qualitative arguments, the polynomial fit ansätze of second order or higher are ruled out for this particular problem of fitting the kurtosis with this set of kurtosis points. In contrast, the linear fit ansatz produced good fit results. The new idea of choosing the Gompertz function as a fit ansatz for the kurtosis fit was also analyzed. It showed good agreement with the linear fit as its basically curved shape became almost straight for this set of kurtosis points and the range where it was applied. However, its advantage of having two asymptotes in the $-\infty$ and ∞ limits might become useful, when larger ranges of masses are simulated or larger aspect ratios are taken into account. The need of a correction term for the linear fit ansatz has been examined by excluding small volumes. The main conclusion is, that for this set of kurtosis points the correction term is still relevant for the two largest volumes $N_s=48, 56$.

A good linear fit with correction has been found to be the best fit, including all but one kurtosis point, from which a critical mass value has been obtained. This result is a first step towards the localization of the heavy critical Z_2 point with staggered fermions. It has to be emphasized again, that this result is preliminary as some simulations are still running and the fit results might change to some probably small extent. Only for one temporal lattice extent N_τ , simulations were performed, precluding any assessment of the behavior of the critical mass in the continuum limit. As the pion mass in physical units is only calculated for the simulated bare quark masses, the critical pion mass can

only be given as a range. Nonetheless, this allows a rough comparison with the critical pion mass from $N_\tau=8$ Wilson simulations, resulting in a good compatibility.

With the PFG, a fitting program with a graphical user interface has been implemented, which is handy to use and offers numerous features to easily compare a bunch of fits. Several kurtosis fit functions have been implemented and can be used on either data from Wilson fermions (kurtosis depending on κ) or staggered fermions (kurtosis depending on am). Although the PFG in the current state can perform a lot of tasks and has been modified and generalized during this project, some features are to be implemented in the future. To name just a few examples, it should be possible to save fits and the corresponding data in a file, which persists after closing the PFG and can be reloaded. As a bigger feature, a generalization related to the available fit functions and the fit data input could be implemented. These ideas can be implemented, when such features are required.

For the physical aspect of this work, some perspectives can be formulated. The still running simulations are to be completed in the future and the analysis and the fitting will be repeated to obtain a final result for the critical mass for $N_\tau=8$. Even larger N_τ should be investigated for staggered fermions, as it would allow to draw conclusions of the shift of the critical mass with respect to the continuum limit. The problem, however, is the increasing computational cost with increasing lattice sizes. The maximum computational time of this project is required by the $N_s=64$ simulations, with ~ 150 s per trajectory. Simulating 100k trajectories requires roughly half a year without queuing time. Thus, for larger N_τ and a comparable aspect ratio of 7 or 8, this does not seem to be feasible with the current set-up. As a consequence, simulations have to be sped up significantly, for example by the implementation of a parallelized algorithm for staggered fermions in CL²QCD. Currently, each Monte Carlo chain simulation is run on only one GPU or optionally CPU. Distributing the computations for different lattice sites on different devices can speed up the simulations, albeit at similar computational cost. Overall, it has been observed, that the computational cost and time of such thermal lattice QCD simulations often limits the accuracy of the outcome. However, effective and well elaborated methods to analyze the data with regard to phase transitions can lead to satisfying results.

Appendices

A. Derivation of the Kurtosis Correction Term

As it was shown in section 3.1.4, the kurtosis can be expressed in terms of the cumulants κ_i

$$B_4 = \frac{\kappa_4}{\kappa_2^2} + 3, \quad (\text{A.1})$$

where the cumulants can be obtained by applying derivatives on the cumulant-generating function \tilde{F} , the reduced free energy. The goal is deriving a scaling form of the kurtosis of an observable, not only consisting of a magnetic part, but also of an energy part. Thus, the general observable

$$O = c_E \cdot E + c_M \cdot M \rightarrow c_E \cdot \frac{\partial}{\partial \tilde{\beta}} + c_M \cdot \frac{\partial}{\partial h} \quad (\text{A.2})$$

is defined, where the operator with the derivatives with respect to the inverse temperature $\tilde{\beta}$ and the reduced magnetic field $h = \tilde{\beta}H$ has to be applied to the reduced free energy. c_E and c_M are constants for the energy part and the magnetic part, respectively. In contrast to reference [35], where the reduced temperature is used in the derivative of the energy like operator, here, the inverse temperature is used. Nevertheless, a similar result is expected. The notation from sections 2.1.2 and 3.1.5 is used.

The operator from equation (A.2) can be applied to the finite size scaling form of the reduced free energy (equation (2.27)), to generate the cumulants. The derivative $\frac{\partial}{\partial \tilde{\beta}}$ still has to be transformed into a derivative with respect to the reduced temperature. Using $\tilde{\beta} = \frac{1}{T}$, $\frac{\partial}{\partial \tilde{\beta}} = -T^2 \frac{\partial}{\partial T}$ is obtained intermediately and with $T = T_c(t + 1)$, the result is $\frac{\partial}{\partial \tilde{\beta}} = -T_c(t + 1)^2 \frac{\partial}{\partial t}$. Putting all of this together,

$$\kappa_4 = \left(c_E t'^2 \cdot \frac{\partial}{\partial t} + c_M \cdot \frac{\partial}{\partial h} \right)^4 \tilde{F}(tN_s^{y_t}, hN_s^{y_h}, 1) \quad (\text{A.3})$$

is the fourth cumulant, where all signs and constants like T_c have been absorbed in the constant c_E and the simplification $t' = t + 1$ was used. Similarly, the second cumulant squared is

$$\kappa_2^2 = \left[\left(c_E t'^2 \cdot \frac{\partial}{\partial t} + c_M \cdot \frac{\partial}{\partial h} \right)^2 \tilde{F}(tN_s^{y_t}, hN_s^{y_h}, 1) \right]^2. \quad (\text{A.4})$$

For simplicity, the arguments of \tilde{F} are omitted and the abbreviation

$$\frac{\partial^n}{\partial t^n} \frac{\partial^m}{\partial h^m} \tilde{F} = \tilde{F}^{(n,m)} \quad (\text{A.5})$$

is used from now on. κ_2^2 is the first term to be calculated:

$$\kappa_2 = c_M^2 N_s^{2y_h} \tilde{F}^{(0,2)} + c_E N_s^{y_t} t'^2 \left(2c_E t' \tilde{F}^{(1,0)} + 2c_M N_s^{y_h} \tilde{F}^{(1,1)} + c_E N_s^{y_t} t'^2 \tilde{F}^{(2,0)} \right) \quad (\text{A.6})$$

If this term is squared, expanded and $c_M^4 N_s^{4y_h} (\tilde{F}^{(0,2)})^2$ is factored out,

$$\begin{aligned} \kappa_2^2 = c_M^4 N_s^{4y_h} (\tilde{F}^{(0,2)})^2 & \left[1 + \frac{4c_E^2 N_s^{y_t-2y_h} t'^3 \tilde{F}^{(1,0)}}{c_M^2 \tilde{F}^{(0,2)}} + \frac{4c_E N_s^{2y_t-4y_h} t'^6 (\tilde{F}^{(1,0)})^2}{c_M^4 (\tilde{F}^{(0,2)})^2} \right. \\ & + \frac{4c_E N_s^{y_t-y_h} t'^2 \tilde{F}^{(1,1)}}{c_M \tilde{F}^{(0,2)}} + \frac{8c_E^3 N_s^{2y_t-3y_h} t'^5 \tilde{F}^{(1,0)} \tilde{F}^{(1,1)}}{c_M^3 (\tilde{F}^{(0,2)})^2} + \frac{4c_E^2 N_s^{2y_t-2y_h} t'^4 (\tilde{F}^{(1,1)})^2}{c_M^2 (\tilde{F}^{(0,2)})^2} \\ & + \frac{2c_E^2 N_s^{2y_t-2y_h} t'^4 \tilde{F}^{(2,0)}}{c_M^2 \tilde{F}^{(0,2)}} + \frac{4c_E^4 N_s^{3y_t-4y_h} t'^7 \tilde{F}^{(1,0)} \tilde{F}^{(2,0)}}{c_M^4 (\tilde{F}^{(0,2)})^2} \\ & \left. + \frac{4c_E^3 N_s^{3y_t-3y_h} t'^6 \tilde{F}^{(1,1)} \tilde{F}^{(2,0)}}{c_M^3 (\tilde{F}^{(0,2)})^2} + \frac{c_E^4 N_s^{4y_t-4y_h} t'^8 (\tilde{F}^{(2,0)})^2}{c_M^4 (\tilde{F}^{(0,2)})^2} \right] \end{aligned} \quad (\text{A.7})$$

is obtained. All terms of order $\mathcal{O}(N_s^{2(y_t-y_h)})$ are neglected, using $y_t - y_h < 0$ in this case. For the terms with unequal factors in front of y_t and y_h , the fractions are expanded with powers of $N_s^{y_t}/N_s^{y_h}$, such that the factors become equal. The additional factor $N_s^{-ny_t}$, ($n \in \{1, 2\}$) is smaller than 1, since $y_t > 0$ and therefore does not conflict with neglecting terms of $\mathcal{O}(N_s^{2(y_t-y_h)})$. The result is

$$\kappa_2^2 = c_M^4 N_s^{4y_h} (\tilde{F}^{(0,2)})^2 \left[1 + \frac{4c_E N_s^{y_t-y_h} t'^2 \tilde{F}^{(1,1)}}{c_M \tilde{F}^{(0,2)}} + \mathcal{O}(N_s^{2(y_t-y_h)}) \right]. \quad (\text{A.8})$$

Similarly, κ_4 can be derived. Conducting the derivatives in equation (A.3),

$$\begin{aligned} \kappa_4 = c_M^4 N_s^{4y_h} \tilde{F}^{(0,4)} & + 24c_E^4 N_s^{y_t} t'^5 \tilde{F}^{(1,0)} + 24c_E^3 c_M N_s^{y_t+y_h} t'^4 \tilde{F}^{(1,1)} \\ & + 12c_E^2 c_M^2 N_s^{y_t+2y_h} t'^3 \tilde{F}^{(1,2)} + 4c_E c_M^3 N_s^{y_t+3y_h} t'^2 \tilde{F}^{(1,3)} + 36c_E^4 N_s^{2y_t} t'^6 \tilde{F}^{(2,0)} \\ & + 24c_E^3 c_M N_s^{2y_t+y_h} t'^5 \tilde{F}^{(2,1)} + 6c_E^2 c_M^2 N_s^{2y_t+2y_h} t'^4 \tilde{F}^{(2,2)} + 12c_E^4 N_s^{3y_t} t'^7 \tilde{F}^{(3,0)} \\ & + 4c_E^3 c_M N_s^{3y_t+y_h} t'^6 \tilde{F}^{(3,1)} + c_E^4 N_s^{4y_t} t'^8 \tilde{F}^{(4,0)} \end{aligned} \quad (\text{A.9})$$

is obtained. The first term $c_M^4 N_s^{4y_h} \tilde{F}^{(0,4)}$ can be factored out, giving

$$\begin{aligned} \kappa_4 = c_M^4 N_s^{4y_h} \tilde{F}^{(0,4)} & \left[1 + \frac{24c_E^4 N_s^{y_t-4y_h} t'^5 \tilde{F}^{(1,0)}}{c_M^4 \tilde{F}^{(0,4)}} + \frac{24c_E^3 N_s^{y_t-3y_h} t'^4 \tilde{F}^{(1,1)}}{c_M^3 \tilde{F}^{(0,4)}} \right. \\ & + \frac{12c_E^2 N_s^{y_t-2y_h} t'^3 \tilde{F}^{(1,2)}}{c_M^2 \tilde{F}^{(0,4)}} + \frac{4c_E N_s^{y_t-y_h} t'^2 \tilde{F}^{(1,3)}}{c_M \tilde{F}^{(0,4)}} + \frac{36c_E^4 N_s^{2y_t-4y_h} t'^6 \tilde{F}^{(2,0)}}{c_M^4 \tilde{F}^{(0,4)}} \\ & + \frac{24c_E^3 N_s^{2y_t-3y_h} t'^5 \tilde{F}^{(2,1)}}{c_M^3 \tilde{F}^{(0,4)}} + \frac{6c_E^2 N_s^{2y_t-2y_h} t'^4 \tilde{F}^{(2,2)}}{c_M^2 \tilde{F}^{(0,4)}} + \frac{12c_E^4 N_s^{3y_t-4y_h} t'^7 \tilde{F}^{(3,0)}}{c_M^4 \tilde{F}^{(0,4)}} \\ & \left. + \frac{4c_E^3 N_s^{3y_t-3y_h} t'^6 \tilde{F}^{(3,1)}}{c_M^3 \tilde{F}^{(0,4)}} + \frac{c_E^4 N_s^{4y_t-4y_h} t'^8 \tilde{F}^{(4,0)}}{c_M^4 \tilde{F}^{(0,4)}} \right]. \end{aligned} \quad (\text{A.10})$$

As before, the terms with unequal factors in front of y_t and y_h are expanded with suitable powers of $N_s^{y_t}/N_s^{y_h}$, such that the terms of order $\mathcal{O}(N_s^{2(y_t-y_h)})$ can be neglected. The result is

$$\kappa_4 = c_M^4 N_s^{4y_h} \tilde{F}^{(0,4)} \left[1 + \frac{4c_E N_s^{y_t-y_h} t'^2 \tilde{F}^{(1,3)}}{c_M \tilde{F}^{(0,4)}} + \mathcal{O}(N_s^{2(y_t-y_h)}) \right]. \quad (\text{A.11})$$

The fraction κ_4/κ_2^2 has to be evaluated and the approximation for the fraction

$$\frac{1+x}{1+y} = (1+x)(1-y + \mathcal{O}(y^2)) \quad (\text{A.12})$$

is used. Subsequently, the kurtosis B_4 can be written as

$$B_4 = \frac{\tilde{F}^{(0,4)}}{\left(\tilde{F}^{(0,2)}\right)^2} \left[1 + \frac{4c_E N_s^{y_t-y_h} t'^2 \tilde{F}^{(1,3)}}{c_M \tilde{F}^{(0,4)}} + \mathcal{O}(N_s^{2(y_t-y_h)}) \right] \cdot \left[1 - \frac{4c_E N_s^{y_t-y_h} t'^2 \tilde{F}^{(1,1)}}{c_M \tilde{F}^{(0,2)}} + \mathcal{O}(N_s^{2(y_t-y_h)}) \right] + 3, \quad (\text{A.13})$$

which can be expanded and again terms of $\mathcal{O}(N_s^{2(y_t-y_h)})$ are neglected.

$$B_4 = \frac{\tilde{F}^{(0,4)}}{\left(\tilde{F}^{(0,2)}\right)^2} \left[1 + \frac{4c_E N_s^{y_t-y_h} t'^2 \tilde{F}^{(1,3)}}{c_M \tilde{F}^{(0,4)}} - \frac{4c_E N_s^{y_t-y_h} t'^2 \tilde{F}^{(1,1)}}{c_M \tilde{F}^{(0,2)}} + \mathcal{O}(N_s^{2(y_t-y_h)}) \right] + 3 \quad (\text{A.14})$$

is simplified and in a second step some constants can be combined:

$$B_4 = \frac{\tilde{F}^{(0,4)}}{\left(\tilde{F}^{(0,2)}\right)^2} \left[1 + \frac{4c_E t'^2}{c_M} \left(\frac{\tilde{F}^{(1,3)}}{\tilde{F}^{(0,4)}} - \frac{\tilde{F}^{(1,1)}}{\tilde{F}^{(0,2)}} \right) N_s^{y_t-y_h} + \mathcal{O}(N_s^{2(y_t-y_h)}) \right] + 3 \quad (\text{A.15})$$

$$= \frac{\tilde{F}^{(0,4)}}{\left(\tilde{F}^{(0,2)}\right)^2} \left[1 + C N_s^{y_t-y_h} + \mathcal{O}(N_s^{2(y_t-y_h)}) \right] + 3, \quad (\text{A.16})$$

where the substitution $C = \frac{4c_E t'^2}{c_M} \left(\frac{\tilde{F}^{(1,3)}}{\tilde{F}^{(0,4)}} - \frac{\tilde{F}^{(1,1)}}{\tilde{F}^{(0,2)}} \right)$ was used. C is assumed to be constant with respect to t . This approximation is not exact, as $t'^2 = (t+1)^2$ is a factor in C and the derivatives $\tilde{F}^{(n,m)}$ also depend on t . C becomes constant with respect to t for $t \rightarrow 0$. t'^2 becomes 1 if $t \rightarrow 0$. More precisely, the approximation C , being constant is only valid, if terms of $\mathcal{O}(t)$ can be neglected in this case.

B. Derivation of the Fit Formulas

In section 3.1.6, a general form of a kurtosis fit function has been introduced. For a better understanding, equation (3.48) is shown again

$$B_4(x) = F(x)(1 + CN_s^{y_t - y_h}). \quad (\text{B.1})$$

Different approaches to model $F(x)$ are introduced and derived in section 3.1.6, mainly focusing on the polynomial function. The other approaches are derived in this appendix to show, how the resulting fit formulas are achieved.

The main focus of these different approaches is on accounting for the asymmetry of the kurtosis around the critical point. This can be seen in figure B.1, where not only the kurtosis values at the critical β in the infinite volume are shown (black line), but also the finite size behavior, that depends on the spatial extent of the simulated volume (red: large volume, blue: small volume). This schematic plot only models the kurtosis for a purely magnetization like order parameter, implying a vanishing correction term $C = 0$ in formula (B.1), thus modeling $F(x)$. The asymmetry stems from the fact, that the kurtosis at the Z_2 -point is not located in the center between the infinite volume kurtosis of the crossover transition and the 1. order phase transition. All kurtosis lines for different volumes cross at the Z_2 -point, which calls for taking the asymmetry into account for the fit function. This becomes important, if the fit leaves the close region around the Z_2 -point, where the kurtosis lines can be approximated as linear functions.

Another motivation to find more sophisticated fit formulas is the need to include kurtosis points into the fit, which are not sufficiently close to the Z_2 -point to fall into the linear region. The goal will be to find functions, which account for the previously described asymmetry and are bounded from below and above by two constant asymptotes, as can be seen in figure B.1.

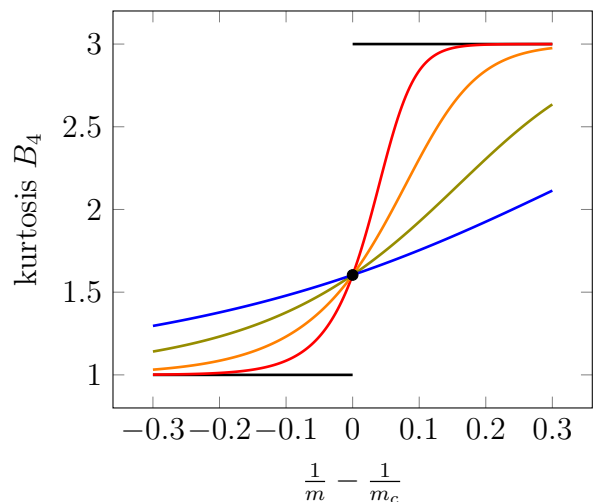


Figure B.1.: Model of the finite size effects of the kurtosis B_4 of a purely magnetization like observable as a function of the inverse mass $\frac{1}{m} - \frac{1}{m_c}$ for small spatial volumes (blue) to large ones (red)

B.1. The Rescaling Term in the Polynomial Fit

To understand the idea of an asymmetric rescaling term, again, the finite size scaling formula of the kurtosis, shown in figure B.1, has to be considered. Since the polynomial functions (restricting them here to uneven powers) are symmetric with respect to the Z_2 point, the idea is to adapt the polynomials to this asymmetry. One approach is to assume, that the finite size values of the kurtosis in the 1. order region are compressed by a factor $\frac{1}{f}$ between the kurtosis value 1 and the kurtosis value at the Z_2 -point 1.604. This compression affects the slope of the polynomials in this region, leading to a new slope s' depending on the old slope s via $s' = f \cdot s$. Thus, the slope s is rescaled by a factor f to a new slope s' , as it can be seen in figure B.2 for a linear function.

An important motivation for this rescaling approach is the assumption, that the kurtosis lines in figure B.1 approach the asymptotes 1 and 3 equally fast. This can be seen in figure B.2, as both lines with different slopes cross the asymptotes at the same distance from the Z_2 -point c .

Having stated the necessary assumptions, the value of the factor f can be derived with the help of figure B.2. With the two slope triangles, the two slopes are

$$s = \frac{a}{c}, \quad (\text{B.2})$$

$$s' = \frac{b}{c}. \quad (\text{B.3})$$

These equations relate via c , which can be eliminated and

$$s' = \frac{B_4(Z_2, \infty) - B_4(1.O, \infty)}{B_4(CO, \infty) - B_4(Z_2, \infty)} \cdot s = f \cdot s \quad (\text{B.4})$$

is obtained as the rescaled slope, with

$$f = \frac{B_4(Z_2, \infty) - B_4(1.O, \infty)}{B_4(CO, \infty) - B_4(Z_2, \infty)} \approx 0.4327. \quad (\text{B.5})$$

A specific fit function is found, exhibiting the property of its slopes, being related in the two different regions by equation (B.4). In the following, the scaling variable $x = \left(\frac{1}{m} - \frac{1}{m_c}\right) N_s^{1/\nu}$ will be used and for $x < 0$ a 1. order phase transition is assumed and for $x > 0$ a crossover. A scaling variable dependent factor $R(x)$ is inserted in front of the terms in the polynomial contributing to its slope. This factor evaluates to

$$R(x) = \begin{cases} 1, & \text{if } x > 0 \\ f, & \text{if } x < 0, \end{cases} \quad (\text{B.6})$$

which can be achieved, using the Heaviside function $\Theta(x)$. Hence, $R(x)$ is represented as

$$R(x) = 1 + (f - 1)\Theta(x). \quad (\text{B.7})$$

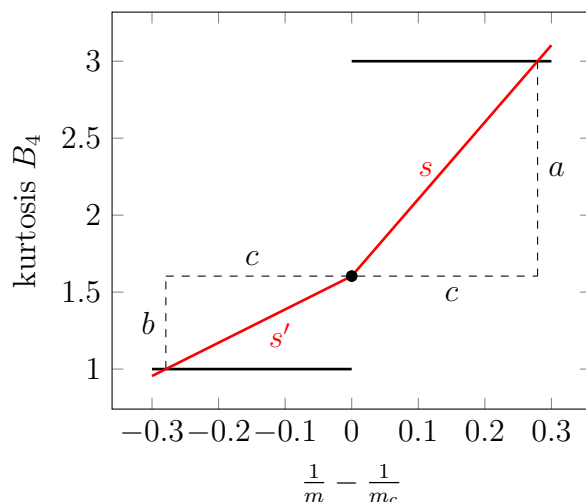


Figure B.2.: Rescaling the slope of the linear kurtosis fit function in the 1. order region from $s \rightarrow s'$

For cases, in which negative values of the scaling variable are related to a crossover and positive values are related to a 1. order phase transition, the Heaviside function $\Theta(x)$ in $R(x)$ has to be changed to $\Theta(-x)$. The final formula for the polynomial fit function with the rescaled slope is

$$F'_P(x) = B_4(Z_2, \infty) + R(x) \sum_{n \in M} a_n x^n. \quad (\text{B.8})$$

B.2. The General Logistic Fit Functions

A function, fulfilling the requirements of two constant asymptotes for the limits to $-\infty$ and ∞ of the domain, is the generalized logistic function

$$Y_1(x) = L + \frac{R - L}{[1 + Q \exp(-rx)]^A} \quad (\text{B.9})$$

and the similar, but not equal function

$$Y_2(x) = R + \frac{L - R}{[1 + Q \exp(rx)]^A}. \quad (\text{B.10})$$

The parameters are $R, L \in \mathbb{R}$ and $r, Q, A \in \mathbb{R}_{>0}$. Additionally, these functions allow an asymmetric crossing point of the functions with different volumes. From now on, $Y_2(x)$ is called the flipped version of $Y_1(x)$, as it is obtained by interchanging R and L and omitting the minus sign in front of r . An example plot of both functions can be seen in figure B.3. The actual fit formula is derived only for $Y_1(x) = Y(x)$, because it can be done analogously for $Y_2(x)$. Considering the “flipped” version of the function, represented in equation (B.9), as an extra fit function is not obvious. Indeed, the “flip” changes the asymmetry of the function around the function value 0. The choice of the version of the function affects, which asymptote is approached faster, implying a larger slope in the vicinity of the asymptote. The first generalized logistic function (B.9) approaches the upper asymptote faster than the lower one.

First, the constraints for the fit formula, originating from the crossing point and the asymptotes, are presented. Again, $x = \left(\frac{1}{m} - \frac{1}{m_c}\right) N_s^{1/\nu}$ is taken as the scaling variable and a first order phase transition is assumed for $x < 0$, likewise a crossover for $x > 0$. Thus, the constraints can be written as

$$Y(\infty) = B_4(CO, \infty) = 3, \quad (\text{B.11})$$

$$Y(-\infty) = B_4(1.O, \infty) = 1, \quad (\text{B.12})$$

$$Y(0) = B_4(Z_2, \infty) = 1.604. \quad (\text{B.13})$$

This will determine some of the parameters as follows.

$$Y(x \rightarrow \infty) = R = B_4(CO, \infty) \quad (\text{B.14})$$

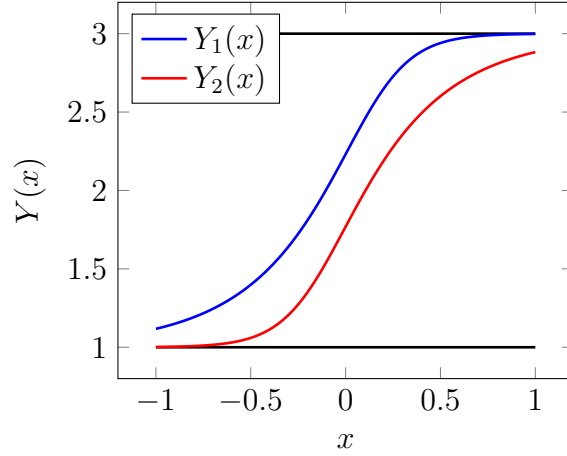


Figure B.3.: Example functions $Y_1(x)$ and $Y_2(x)$ with $L=1$, $R=3$, $Q=3$, $r=7$, $A=0.35$.

determines R in the same way as

$$Y(x \rightarrow -\infty) = L = B_4(1.O, \infty) \quad (\text{B.15})$$

determines L . The last condition can either determine Q or A , depending on the other parameter, respectively.

$$Y(0) = L + \frac{R - L}{[1 + Q]^A} = B_4(Z_2, \infty) \quad (\text{B.16})$$

can be transformed to

$$A = \frac{\ln\left(\frac{R-L}{B_4(Z_2, \infty) - L}\right)}{\ln(1 + Q)} = \frac{\ln\left(\frac{B_4(CO, \infty) - B_4(1.O, \infty)}{B_4(Z_2, \infty) - B_4(1.O, \infty)}\right)}{\ln(1 + Q)} \quad (\text{B.17})$$

or

$$Q = \left[\frac{R - L}{B_4(Z_2, \infty) - L} \right]^{\frac{1}{A}} - 1 = \left[\frac{B_4(CO, \infty) - B_4(1.O, \infty)}{B_4(Z_2, \infty) - B_4(1.O, \infty)} \right]^{\frac{1}{A}} - 1, \quad (\text{B.18})$$

where either Q or A are the only free parameters, which are used as fit parameters. Inserting either equation (B.17) or (B.18) into the formula for the generalized logistic function leads to two equivalent functions with different parametrization, which might differ numerically, when fitting to these functions. Using the determinations of the parameters R and L ((B.14), (B.15)),

$$F_{GL,12}(x) = B_4(1.O, \infty) + \frac{B_4(CO, \infty) - B_4(1.O, \infty)}{\left[1 + \left(\left[\frac{B_4(CO, \infty) - B_4(1.O, \infty)}{B_4(Z_2, \infty) - B_4(1.O, \infty)} \right]^{\frac{1}{a}} - 1 \right) \cdot \exp(-rx) \right]^a}, \quad (\text{B.19})$$

$$F_{GL,3}(x) = B_4(1.O, \infty) + \frac{B_4(CO, \infty) - B_4(1.O, \infty)}{[1 + q \cdot \exp(-rx)]^{\ln\left(\frac{B_4(CO, \infty) - B_4(1.O, \infty)}{B_4(Z_2, \infty) - B_4(1.O, \infty)}\right) \ln^{-1}(1+q)}} \quad (\text{B.20})$$

are obtained, where the small parameter names q and a have been used instead of Q and A to mark those parameters as fit parameters.

As these highly non-linear fit parameters q and a might sometimes be difficult to handle for the fitting algorithm, it was tried to avoid the exponent A , but nonetheless keep the asymmetry property of the function. One way to find such a function is to choose $A = 1$ in equation (B.9) and add another exponential in the denominator

$$Z(x) = L + \frac{R - L}{1 + Q_1 \exp(-r_1 x) + Q_2 \exp(-r_2 x)}, \quad (\text{B.21})$$

where $Q_1, Q_2 \in \mathbb{R}_{>0}$ and $r_1, r_2 \in \mathbb{R}$. Choosing $r_1, r_2 > 0$, the same values for R and L are obtained as for the generalized logistic fit ((B.14), (B.15)). The same argument, that the kurtosis lines all cross in the same point at $x = 0$, also applies here

$$Z(0) = L + \frac{R - L}{1 + Q_1 + Q_2} = B_4(Z_2, \infty). \quad (\text{B.22})$$

This equation can be rearranged to eliminate Q_2 in formula (B.21) and inserting the values for L and R yields

$$Q_2 = \frac{B_4(CO, \infty) - B_4(1.O, \infty)}{B_4(Z_2, \infty) - B_4(1.O, \infty)} - 1 - Q_1. \quad (\text{B.23})$$

Inserting this expression in equation (B.21), the final result is

$$F_{GL,4}(x) = B_4(1.O, \infty) + \frac{B_4(CO, \infty) - B_4(1.O, \infty)}{1 + q \exp(-r_1 x) + \left(\frac{B_4(CO, \infty) - B_4(1.O, \infty)}{B_4(Z_2, \infty) - B_4(1.O, \infty)} - 1 - q \right) \exp(-r_2 x)}, \quad (\text{B.24})$$

where the lowercase letters q, r_1 and r_2 represent the fit parameters. This form of fit function establishes the possibility to run into unwanted singularities due to the structure of the denominator. For a brief analysis, some abbreviating definitions are introduced

$$a \equiv \exp(-r_1 x), \quad (\text{B.25})$$

$$b \equiv \exp(-r_2 x), \quad (\text{B.26})$$

$$C \equiv \frac{B_4(CO, \infty) - B_4(1.O, \infty)}{B_4(Z_2, \infty) - B_4(1.O, \infty)} - 1 \approx 2.3113, \quad (\text{B.27})$$

such that the denominator turns into $d = 1 + qa + (C - q)b$. As all variables q, a, b and the constant C of the denominator are positive, the simplest way to exclude all possible singularities is the restriction of q to the range $q \in (0, C]$. Hence, the denominator cannot become zero and the singularities are avoided. This is clearly a drawback of this fit function and actually, this ansatz was never used in practice to analyze data. The derivation is given nevertheless, since it was implemented in the PFG for experimental use and the appendix section B.2 about the derivation of the implemented general logistic fit functions should not suffer from incompleteness with respect to the available fit functions in the PFG (see section 3.3.3).

B.3. The Gompertz Fit Function

Another function with the properties of two constant asymptotes and an asymmetry around the function value 0 is the Gompertz function. It is named after Benjamin Gompertz, who mentioned this type of function first in a paper in 1825 [19]. A general form of this function is

$$G(x) = L + (R - L) \exp(-D \exp(-s \cdot x)). \quad (\text{B.28})$$

As in the previous section B.2 of this appendix, the constraints

$$G(\infty) = B_4(CO, \infty) = 3, \quad (\text{B.29})$$

$$G(-\infty) = B_4(1.O, \infty) = 1, \quad (\text{B.30})$$

$$G(0) = B_4(Z_2, \infty) = 1.604 \quad (\text{B.31})$$

are used to determine the parameters $L, R \in \mathbb{R}$ and $D \in \mathbb{R}_{>0}$. The parameter $s \in \mathbb{R}$ reflects the growth rate. Again, a first order phase transition is assumed for a scaling variable $x < 0$. For $x > 0$ the transition is a crossover. Using the assumption, that $s > 0$ the results for L and R are

$$G(\infty) = R = B_4(CO, \infty) \quad (\text{B.32})$$

$$G(-\infty) = L = B_4(1.O, \infty). \quad (\text{B.33})$$

Using the third conditional equation (B.31),

$$G(0) = B_4(Z_2, \infty) = L + (R - L) \exp(-D) \quad (\text{B.34})$$

is obtained, which can be transformed, such that D is determined by $D = \ln\left(\frac{R-L}{B_4(Z_2, \infty) - L}\right)$. Using this equation and inserting the values for R and L , the final result for the Gompertz fit function is

$$F_G(x) = B_4(1.O, \infty) + (B_4(CO, \infty) - B_4(1.O, \infty)) \exp\left(-\frac{\ln\left(\frac{B_4(CO, \infty) - B_4(1.O, \infty)}{B_4(Z_2, \infty) - B_4(1.O, \infty)}\right)}{\exp(sx)}\right). \quad (\text{B.35})$$

The only fit parameter is s , meaning, that the asymmetry of the function is not free anymore but determined by the constraint (B.31). This is in contrast to the generalized logistic function from section B.2, where either the fit parameters a or q tune the asymmetry of the function. The fit parameter s is responsible for the growth rate, as can be seen in figure B.4, where two example functions of type (B.28) are plotted for varying s . Here, the asymmetry is determined by the parameter $D = 0.5$.

As for the generalized logistic function, also the Gompertz function has a flipped version. Again, this implies, that the parameters R and L are interchanged and the minus sign in the general Gompertz function (B.28) vanishes. Considering the flipped version of the Gompertz function is mandatory, because the “flip” changes the asymmetry around the function value 0.

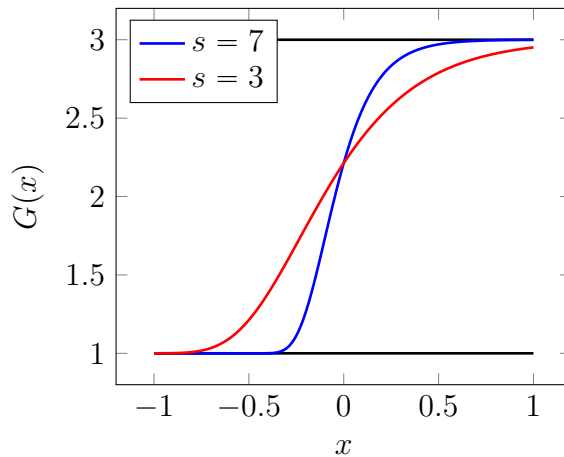


Figure B.4.: Example functions $G(x)$ with $L=1$, $R=3$, $D=0.5$ and varying s .

C. Additional Tables Concerning the PFG Tests

This part of the appendix provides the data of the test of the PFG, comparing the fit results for the PFG with the script `BinderFitVSmass.sh`. How the fit results are obtained, is explained in detail in section 3.3.4, including a discussion of the implications of the test results. First, an overview over the kurtosis data is given in table C.1, which was used to perform the comparison of the script `BinderFitVSmass.sh` and the PFG. The data stems from simulations with $N_f=2$ staggered fermions at $\mu=0$ and $N_\tau=8$. The precision of the numbers in the table is the same as in the data file, being loaded into the fit programs.

mass	N_s	$B_4(\beta_c, \langle L \rangle)$	$\Delta B_4(\beta_c, \langle L \rangle)$
0.35	32	2.011839919846	$1.180137020367 \cdot 10^{-1}$
0.55	32	1.857083793747	$6.157305193067 \cdot 10^{-2}$
0.75	32	1.847246220144	$5.170964017263 \cdot 10^{-2}$
0.95	32	1.832102956146	$5.511508631404 \cdot 10^{-2}$
0.35	40	2.130313420209	$1.103633751420 \cdot 10^{-1}$
0.55	40	1.776282162304	$1.067535194286 \cdot 10^{-1}$
0.75	40	1.644601000008	$6.811929819971 \cdot 10^{-2}$
0.95	40	1.675662976781	$9.485754562186 \cdot 10^{-2}$
1.15	40	1.715857591535	$7.459022441265 \cdot 10^{-2}$
0.35	48	2.348543274750	$1.345902600477 \cdot 10^{-1}$
0.55	48	1.757581191144	$1.065048203167 \cdot 10^{-1}$
0.75	48	1.604510446266	$9.930628757743 \cdot 10^{-2}$
0.95	48	1.642134039813	$1.022491771119 \cdot 10^{-1}$
1.15	48	1.620023303629	$6.480188058879 \cdot 10^{-2}$
0.35	56	2.519318288919	$1.574935639318 \cdot 10^{-1}$
0.55	56	1.807187631840	$9.184898296016 \cdot 10^{-2}$
0.75	56	1.524268874835	$1.233221516074 \cdot 10^{-1}$
0.95	56	1.532968334390	$1.085571101172 \cdot 10^{-1}$
1.15	56	1.460864913312	$8.895867942122 \cdot 10^{-2}$
0.75	64	1.614267226053	$1.248892508557 \cdot 10^{-1}$

Table C.1.: kurtosis data being used to compare the fit results of the PFG with those of the script `BinderFitVSmass.sh`

The color scheme is given again in table C.3, indicating the deviation of the fit results of both programs in the tables C.2, C.4 and C.5. The deviations δ are defined as $\delta = |1 - x_{PFG}/x_S|$, where x_{PFG} is a fit result for the PFG and x_S is the correspond-

	program	$m_c \pm \Delta m_c$	$a_1 \pm \Delta a_1$	χ^2_{ndf}
data set 1	PFG	1.05406 ± 0.0477074	$-0.00133372 \pm 0.00018179$	3.9777
	Script	1.05406 ± 0.0477074	$-0.00133372 \pm 0.00018179$	3.9777
data set 2	PFG	0.828911 ± 0.0334132	$-0.00219748 \pm 0.000311247$	2.16224
	Script	0.828911 ± 0.0334132	$-0.00219748 \pm 0.000311247$	2.16224
data set 3	PFG	0.950745 ± 0.0475213	$-0.00129977 \pm 0.000213453$	3.39004
	Script	0.950745 ± 0.0475213	$-0.00129977 \pm 0.000213453$	3.39004

Table C.2.: comparison of the fit results for the linear kurtosis fit

ing fit result for the script `BinderFitVSmass.sh`. A white cell color indicates a smaller deviation than 10^{-6} , which is thus not observed within the 6 relevant digits. This is the case for all fit results of the linear fit in table C.2. Table C.4 shows the results of the linear fit function with correction. The table, corresponding to the cubic fit, was already displayed in section 3.3.4 and therefore is omitted here. The last table C.5 corresponds to the cubic kurtosis fit with correction term.

	program	$m_c \pm \Delta m_c$	$a_1 \pm \Delta a_1$	$b \pm \Delta b$	χ_{ndf}^2
data set 1	PFG	0.69461 ± 0.08187	$-0.00110507 \pm 0.000166934$	3.62169 ± 0.649791	2.25133
	Script	0.69461 ± 0.08187	$-0.00110507 \pm 0.000166934$	3.62169 ± 0.649791	2.25133
data set 2	PFG	0.722481 ± 0.0756312	$-0.00204107 \pm 0.000305621$	2.31528 ± 1.51475	2.13341
	Script	0.72248 ± 0.0756312	$-0.00204107 \pm 0.000305621$	2.31528 ± 1.51475	2.13341
data set 3	PFG	0.530308 ± 0.20179	$-0.00114981 \pm 0.000188876$	6.67155 ± 3.193	3.20341
	Script	0.530308 ± 0.20179	$-0.00114981 \pm 0.000188876$	6.67154 ± 3.193	3.20341

Table C.4.: comparison of the fit results for the linear kurtosis fit with correction term

		$m_c \pm \Delta m_c$	$a_1 \pm \Delta a_1$	$a_3 \pm \Delta a_3$	$b \pm \Delta b$	χ_{ndf}^2
data set 1	PFG	0.828048 ± 0.0235656	$-0.000113002 \pm 0.000321317$	$-3.43976 \cdot 10^{-8} \pm 9.40164 \cdot 10^{-9}$	2.65465 ± 0.369266	1.37434
	Script	0.8279 ± 0.0235233	$-0.000111617 \pm 0.000321247$	$-3.44422 \cdot 10^{-8} \pm 9.40528 \cdot 10^{-9}$	2.65591 ± 0.369098	1.37434
data set 2	PFG	0.761823 ± 0.0527824	$-0.000668895 \pm 0.000523461$	$-5.33937 \cdot 10^{-8} \pm 2.65166 \cdot 10^{-8}$	1.37608 ± 0.900136	0.919007
	Script	0.760517 ± 0.0519042	$-0.000661639 \pm 0.000524783$	$-5.40122 \cdot 10^{-8} \pm 2.66096 \cdot 10^{-8}$	1.39178 ± 0.894319	0.919149
data set 3	PFG	0.868206 ± 0.0443305	$0.000189158 \pm 0.000429714$	$-3.6375 \cdot 10^{-8} \pm 1.24307 \cdot 10^{-8}$	0.567581 ± 0.987073	0.918911
	Script	0.868216 ± 0.0443531	$0.000188888 \pm 0.000429137$	$-3.6369 \cdot 10^{-8} \pm 1.2433 \cdot 10^{-8}$	0.567467 ± 0.98735	0.918911

Table C.5.: comparison of the fit results for the cubic kurtosis fit with correction term

range of δ	color
$[10^{-6}, 10^{-5})$	blue
$[10^{-5}, 10^{-4})$	green
$[10^{-4}, 10^{-3})$	yellow
$[10^{-3}, 10^{-2})$	orange
$[10^{-2}, 10^{-1})$	red

Table C.3.: colors in test tables

Bibliography

- [1] Mark G. Alford et al. „Color superconductivity in dense quark matter“. In: *Reviews of Modern Physics* 80.4 (Nov. 2008), pp. 1455–1515. ISSN: 1539-0756. DOI: [10.1103/revmodphys.80.1455](https://doi.org/10.1103/revmodphys.80.1455). URL: <http://dx.doi.org/10.1103/RevModPhys.80.1455> (cit. on p. 24).
- [2] Y. Aoki et al. „The order of the quantum chromodynamics transition predicted by the standard model of particle physics“. In: *Nature* 443.7112 (Oct. 2006), pp. 675–678. ISSN: 1476-4687. DOI: [10.1038/nature05120](https://doi.org/10.1038/nature05120). URL: <http://dx.doi.org/10.1038/nature05120> (cit. on pp. 1, 24).
- [3] Matthias Bach et al. „Twisted-Mass Lattice QCD using OpenCL“. In: *PoS LATTICE 2013* (2014), p. 032. DOI: [10.22323/1.187.0032](https://doi.org/10.22323/1.187.0032) (cit. on p. 43).
- [4] A. Bazavov et al. „Nonperturbative QCD simulations with 2+1 flavors of improved staggered quarks“. In: *Reviews of Modern Physics* 82.2 (May 2010), pp. 1349–1417. ISSN: 1539-0756. DOI: [10.1103/revmodphys.82.1349](https://doi.org/10.1103/revmodphys.82.1349). URL: <http://dx.doi.org/10.1103/RevModPhys.82.1349> (cit. on p. 9).
- [5] H. W. J. Blote, E. Luijten, and J. R. Heringa. „Ising universality in three dimensions: a Monte Carlo study“. In: *Journal of Physics A: Mathematical and General* 28.22 (Nov. 1995), pp. 6289–6313. DOI: [10.1088/0305-4470/28/22/007](https://doi.org/10.1088/0305-4470/28/22/007). URL: <https://doi.org/10.1088/0305-4470/28/22/007> (cit. on p. 35).
- [6] Szabolcs Borsányi et al. „High-precision scale setting in lattice QCD“. In: *Journal of High Energy Physics* 2012.9 (Sept. 2012). ISSN: 1029-8479. DOI: [10.1007/jhep09\(2012\)010](https://doi.org/10.1007/jhep09(2012)010). URL: [http://dx.doi.org/10.1007/JHEP09\(2012\)010](http://dx.doi.org/10.1007/JHEP09(2012)010) (cit. on pp. 12, 46).
- [7] Szabolcs Borsányi et al. „Is there still any T_c mystery in lattice QCD? Results with physical masses in the continuum limit III“. In: *Journal of High Energy Physics* 2010.9 (Sept. 2010). ISSN: 1029-8479. DOI: [10.1007/jhep09\(2010\)073](https://doi.org/10.1007/jhep09(2010)073). URL: [http://dx.doi.org/10.1007/JHEP09\(2010\)073](http://dx.doi.org/10.1007/JHEP09(2010)073) (cit. on pp. 2, 24).
- [8] Frank R. Brown et al. „On the existence of a phase transition for QCD with three light quarks“. In: *Phys. Rev. Lett.* 65 (20 Nov. 1990), pp. 2491–2494. DOI: [10.1103/PhysRevLett.65.2491](https://doi.org/10.1103/PhysRevLett.65.2491). URL: <https://link.aps.org/doi/10.1103/PhysRevLett.65.2491> (cit. on p. 24).
- [9] John Cardy. *Scaling and Renormalization in Statistical Physics*. Cambridge Lecture Notes in Physics. Cambridge University Press, 1996. DOI: [10.1017/CB09781316036440](https://doi.org/10.1017/CB09781316036440) (cit. on pp. 16, 19).
- [10] M. A. Clark and A. D. Kennedy. „Accelerating staggered-fermion dynamics with the rational hybrid Monte Carlo algorithm“. In: *Phys. Rev. D* 75 (1 Jan. 2007), p. 011502. DOI: [10.1103/PhysRevD.75.011502](https://doi.org/10.1103/PhysRevD.75.011502). URL: <https://link.aps.org/doi/10.1103/PhysRevD.75.011502> (cit. on p. 28).

-
- [11] Francesca Cuteri, Owe Philipsen, and Alessandro Sciarra. „QCD chiral phase transition from noninteger numbers of flavors“. In: *Phys. Rev. D* 97.11 (2018), p. 114511. DOI: [10.1103/PhysRevD.97.114511](https://doi.org/10.1103/PhysRevD.97.114511). arXiv: [1711.05658 \[hep-lat\]](https://arxiv.org/abs/1711.05658) (cit. on p. 34).
- [12] Francesca Cuteri et al. „The deconfinement critical point of lattice QCD with $N_f = 2$ Wilson fermions“. In: *Preprint* (Sept. 2020). arXiv: [2009.14033 \[hep-lat\]](https://arxiv.org/abs/2009.14033) (cit. on pp. 76, 77).
- [13] Francesca Cuteri et al. „Updates on the Columbia plot and its extended/alternative versions“. In: *EPJ Web Conf.* 175 (2018). Ed. by M. Della Morte et al., p. 07032. DOI: [10.1051/epjconf/201817507032](https://doi.org/10.1051/epjconf/201817507032). arXiv: [1710.09304 \[hep-lat\]](https://arxiv.org/abs/1710.09304) (cit. on p. 26).
- [14] Christopher Czaban and Owe Philipsen. „The QCD deconfinement critical point for $N_\tau = 8$ with $N_f = 2$ flavours of unimproved Wilson fermions“. In: *PoS LAT-TICE2016* (2016), p. 056. DOI: [10.22323/1.256.0056](https://doi.org/10.22323/1.256.0056). arXiv: [1609.05745 \[hep-lat\]](https://arxiv.org/abs/1609.05745) (cit. on pp. 76, 77).
- [15] Alan M. Ferrenberg and Robert H. Swendsen. „New Monte Carlo technique for studying phase transitions“. In: *Phys. Rev. Lett.* 61 (23 Dec. 1988), pp. 2635–2638. DOI: [10.1103/PhysRevLett.61.2635](https://doi.org/10.1103/PhysRevLett.61.2635). URL: <https://link.aps.org/doi/10.1103/PhysRevLett.61.2635> (cit. on p. 31).
- [16] Alan M. Ferrenberg and Robert H. Swendsen. „Optimized Monte Carlo data analysis“. In: *Phys. Rev. Lett.* 63 (12 Sept. 1989), pp. 1195–1198. DOI: [10.1103/PhysRevLett.63.1195](https://doi.org/10.1103/PhysRevLett.63.1195). URL: <https://link.aps.org/doi/10.1103/PhysRevLett.63.1195> (cit. on p. 31).
- [17] Christof Gattringer and Christian B. Lang. *Quantum chromodynamics on the lattice*. Vol. 788. Berlin: Springer, 2010. ISBN: 978-3-642-01849-7, 978-3-642-01850-3. DOI: [10.1007/978-3-642-01850-3](https://doi.org/10.1007/978-3-642-01850-3) (cit. on pp. 4, 5, 8, 9, 15, 28, 62).
- [18] Nigel Goldenfeld. *Lectures on phase transitions and the renormalization group*. 85 vols. Frontiers in Physics. Addison-Wesley Publishing Company, 1992. ISBN: 0-201-55408-9 (cit. on pp. 16, 17, 19, 21).
- [19] Benjamin Gompertz. „XXIV. On the nature of the function expressive of the law of human mortality, and on a new mode of determining the value of life contingencies. In a letter to Francis Baily, Esq. F. R. S. &c“. In: *Philosophical Transactions of the Royal Society of London* 115 (Dec. 1825), pp. 513–583. DOI: [10.1098/rstl.1825.0026](https://doi.org/10.1098/rstl.1825.0026). URL: <https://doi.org/10.1098/rstl.1825.0026> (cit. on pp. 42, 89).
- [20] J. D. Hunter. „Matplotlib: A 2D graphics environment“. In: *Computing in Science & Engineering* 9.3 (2007), pp. 90–95. DOI: [10.1109/MCSE.2007.55](https://doi.org/10.1109/MCSE.2007.55) (cit. on p. 50).
- [21] F. Karsch, E. Laermann, and Ch. Schmidt. „The chiral critical point in 3-flavour QCD“. In: *Physics Letters B* 520.1-2 (Nov. 2001), pp. 41–49. ISSN: 0370-2693. DOI: [10.1016/S0370-2693\(01\)01114-5](https://doi.org/10.1016/S0370-2693(01)01114-5). URL: [http://dx.doi.org/10.1016/S0370-2693\(01\)01114-5](http://dx.doi.org/10.1016/S0370-2693(01)01114-5) (cit. on p. 36).
- [22] John Kogut and Leonard Susskind. „Hamiltonian formulation of Wilson’s lattice gauge theories“. In: *Phys. Rev. D* 11 (2 Jan. 1975), pp. 395–408. DOI: [10.1103/PhysRevD.11.395](https://doi.org/10.1103/PhysRevD.11.395). URL: <https://link.aps.org/doi/10.1103/PhysRevD.11.395> (cit. on p. 8).

- [23] Martin Lüscher. „Properties and uses of the Wilson flow in lattice QCD“. In: *Journal of High Energy Physics* 2010.8 (Aug. 2010). ISSN: 1029-8479. DOI: [10.1007/JHEP08\(2010\)071](https://doi.org/10.1007/JHEP08(2010)071). URL: [http://dx.doi.org/10.1007/JHEP08\(2010\)071](http://dx.doi.org/10.1007/JHEP08(2010)071) (cit. on pp. 12, 46).
- [24] M.E.J. Newman and G.T. Barkema. *Monte Carlo Methods in Statistical Physics*. Clarendon Press, 1999. ISBN: 9780198517979. URL: <https://books.google.de/books?id=J5aLdDN4uFwC> (cit. on p. 31).
- [25] Andrea Pelissetto and Ettore Vicari. „Critical phenomena and renormalization-group theory“. In: *Physics Reports* 368.6 (Oct. 2002), pp. 549–727. ISSN: 0370-1573. DOI: [10.1016/S0370-1573\(02\)00219-3](https://doi.org/10.1016/S0370-1573(02)00219-3). URL: [http://dx.doi.org/10.1016/S0370-1573\(02\)00219-3](http://dx.doi.org/10.1016/S0370-1573(02)00219-3) (cit. on p. 21).
- [26] O. Philipsen. „Debye Screening in the QCD Plasma“. In: *Strong and Electroweak Matter 2000* (July 2001). DOI: [10.1142/9789812799913_0008](https://doi.org/10.1142/9789812799913_0008). URL: http://dx.doi.org/10.1142/9789812799913_0008 (cit. on p. 10).
- [27] Christopher Pinke et al. „CL2QCD - Lattice QCD based on OpenCL“. In: *Proceedings of XXXII International Symposium on Lattice Field Theory — PoS(Lattice 2014)* (May 2015). DOI: [10.22323/1.214.0038](https://doi.org/10.22323/1.214.0038). URL: <http://dx.doi.org/10.22323/1.214.0038> (cit. on pp. 43, 44).
- [28] Christopher Pinke et al. „LatticeQCD using OpenCL“. In: *Proceedings of XXIX International Symposium on Lattice Field Theory — PoS(Lattice 2011)* (July 2012). DOI: [10.22323/1.139.0044](https://doi.org/10.22323/1.139.0044). URL: <http://dx.doi.org/10.22323/1.139.0044> (cit. on p. 43).
- [29] Krishna Rajagopal and Frank Wilczek. „The Condensed Matter Physics of QCD“. In: *At The Frontier of Particle Physics* (Apr. 2001), pp. 2061–2151. DOI: [10.1142/9789812810458_0043](https://doi.org/10.1142/9789812810458_0043). URL: http://dx.doi.org/10.1142/9789812810458_0043 (cit. on p. 23).
- [30] D. Rohr et al. *The L-CSC cluster: greenest supercomputer in the world in Green500 list of November 2014*. 2017. arXiv: [1712.09431](https://arxiv.org/abs/1712.09431) [cs.PF] (cit. on p. 44).
- [31] Guido van Rossum. „Style Guide for Python Code. PEP 8“. In: *Python Developer’s Guide* (Aug. 2013). URL: <https://www.python.org/dev/peps/pep-0008/> (visited on 08/09/2020) (cit. on p. 48).
- [32] Alessandro Sciarra. *AG Philipsen Workflow*. May 2020. URL: <https://gitlab.itp.uni-frankfurt.de/lattice-qcd/ag-philipsen/group-workflow> (cit. on p. 45).
- [33] Alessandro Sciarra. „BaHaMAS: A Bash Handler to Monitor and Administrate Simulations“. In: *EPJ Web Conf.* 175 (2018). Ed. by M. Della Morte et al., p. 09003. DOI: [10.1051/epjconf/201817509003](https://doi.org/10.1051/epjconf/201817509003). arXiv: [1710.08831](https://arxiv.org/abs/1710.08831) [hep-lat] (cit. on p. 44).
- [34] Alessandro Sciarra. „The QCD phase diagram at purely imaginary chemical potential from the lattice“. PhD thesis. Frankfurt am Main: Johann Wolfgang Goethe Universität, 2016, p. 209. URL: https://github.com/AxelKrypton/PhD_Thesis (cit. on pp. 26, 44, 61, 63).

- [35] Shinji Takeda et al. „Update on Nf=3 finite temperature QCD phase structure with Wilson-Clover fermion action“. In: *PoS LATTICE2016* (2017), p. 384. DOI: [10.22323/1.256.0384](https://doi.org/10.22323/1.256.0384). arXiv: [1612.05371 \[hep-lat\]](https://arxiv.org/abs/1612.05371) (cit. on pp. [36](#), [82](#)).
- [36] Pauli Virtanen et al. „SciPy 1.0: Fundamental Algorithms for Scientific Computing in Python“. In: *Nature Methods* 17 (2020), pp. 261–272. DOI: [10.1038/s41592-019-0686-2](https://doi.org/10.1038/s41592-019-0686-2) (cit. on p. [50](#)).
- [37] Peter H. Westfall. „Kurtosis as Peakedness, 1905–2014. R.I.P.“ In: *The American Statistician* 68.3 (2014), pp. 191–195. DOI: [10.1080/00031305.2014.917055](https://doi.org/10.1080/00031305.2014.917055). eprint: <https://doi.org/10.1080/00031305.2014.917055>. URL: <https://doi.org/10.1080/00031305.2014.917055> (cit. on p. [33](#)).
- [38] Kenneth G. Wilson. „Confinement of quarks“. In: *Phys. Rev. D* 10 (8 Oct. 1974), pp. 2445–2459. DOI: [10.1103/PhysRevD.10.2445](https://doi.org/10.1103/PhysRevD.10.2445). URL: <https://link.aps.org/doi/10.1103/PhysRevD.10.2445> (cit. on p. [7](#)).
- [39] Ulli Wolff. „Monte Carlo errors with less errors“. In: *Computer Physics Communications* 156.2 (Jan. 2004), pp. 143–153. ISSN: 0010-4655. DOI: [10.1016/s0010-4655\(03\)00467-3](https://doi.org/10.1016/s0010-4655(03)00467-3). URL: [http://dx.doi.org/10.1016/S0010-4655\(03\)00467-3](http://dx.doi.org/10.1016/S0010-4655(03)00467-3) (cit. on pp. [29](#), [46](#)).
- [40] Peter Young. „Everything You Wanted to Know About Data Analysis and Fitting but Were Afraid to Ask“. In: *SpringerBriefs in Physics* (2015). ISSN: 2191-5431. DOI: [10.1007/978-3-319-19051-8](https://doi.org/10.1007/978-3-319-19051-8). URL: <http://dx.doi.org/10.1007/978-3-319-19051-8> (cit. on pp. [40](#), [58](#)).

Acknowledgments

With respect to the work in the last year for this master's thesis, I'd like to thank some people, who supported me with this work. First of all, many aspects of the analysis in this thesis rely on numerical tools, which have been implemented by members and former members of the working group. Without these scripts and programs, a fast and reliable analysis wouldn't have been possible. Furthermore, I want to thank Alena Schön and Francesca Cuteri for using the PFG and giving feedback about bugs or improvements of its functionality. I am grateful to Owe Philipsen for the supervision of this master's thesis and the discussions of physical questions, which provided me with lots of new insights. I would like to thank Alessandro Sciarra very much, who has been an advisor for me, considering many different aspects. He monitored most of the simulations for this work and advised me for a lot of technical issues. He was always willing to discuss other problems with me, too, for example the possible new features to be implemented within the PFG. Finally, I thank my father Hartmut Kaiser and my grandfather Hartwig Kaiser for their support in formulating good English and I thank Andreas Halsch for his feedback, concerning the content of this thesis.

Selbstständigkeitserklärung

Erklärung nach § 30 Absatz 12 der Prüfungsordnung Physik 2013 für den Bachelor- und den Masterstudiengang

Hiermit erkläre ich, dass ich die Arbeit selbstständig und ohne Benutzung anderer als der angegebenen Quellen und Hilfsmittel verfasst habe. Alle Stellen der Arbeit, die wörtlich oder sinngemäß aus Veröffentlichungen oder aus anderen fremden Texten entnommen wurden, sind von mir als solche kenntlich gemacht worden. Ferner erkläre ich, dass die Arbeit nicht - auch nicht auszugsweise - für eine andere Prüfung verwendet wurde.

Frankfurt, den 20. November 2020

Reinhold Kaiser